Resonances, R-matrix – Rotations in ^{12}C?

Jonas Refsgaard

PhD Dissertation

Supervisor: Hans O. U. Fynbo

Institut for Fysik og Astronomi
Aarhus Universitet

September 2016

Croyez ceux qui cherchent la vérité,
doutez de ceux qui la trouvent.

– André Gide

Dansk Resumé

Denne afhandling beskriver et eksperiment hvor der er målt på henfaldet af den radioaktive ^{12}N kerne. Ioner af ^{12}N implanteres i et tyndt folie, hvorefter de β henfalder med en halveringstid på 11 ms. Henfaldets datterkerne er ^{12}C, hvor både grundtilstanden og adskillige exciterede tilstande populeres. Hvis den populerede tilstand har en excitationsenergi højere end tærsklen for α emission, er der stor sandsynlighed for at ^{12}C kernen bryder op og udsender tre lav-energetiske α partikler. Disse α partikler detekteres i en opstilling af pixeldetektorer, og både energier og impulser af de tre partikler kan bestemmes. De observerede tre-partikel tilstande repræsenteres i et såkaldt Dalitz plot. En sekventiel henfaldsmodel kombineres med den veletablerede R-matrix formalisme og vha. Monte Carlo simuleringer sammenlignes den teoretiske model med de eksperimentelle data. Det konkluderes at excitationsspektret mellem 8 MeV og 12 MeV er domineret af resonanser med $J^\pi = 0^+$ som henfalder sekventielt til grundtilstanden in ^{8}Be gennem udsendelse af en α partikel med $L = 0$. Spektret mellem 12 MeV og 15 MeV er derimod domineret af en 2^+ tilstand ($\sim 66\,\%$ af spektret) og en 0^+ tilstand ($\sim 25\,\%$ af spektret) som begge henfalder til den første exciterede tilstand i ^{8}Be gennem udsendelse af en α partikel med $L = 2$. Den resterende del af henfaldene i dette energiområde sker gennem grundtilstanden i ^{8}Be. En meget berømt 2^+ tilstand ved en excitationsenergi på 10 MeV, forudsagt i 1956 og målt første gang i 2013, kan ikke éntydigt identificeres i dette eksperiment.

English Resumé

This thesis describes an experiment on the decay of the radioactive ^{12}N nucleus. Ions of ^{12}N are implanted in a thin foil, whereafter they β decay with a half-life of 11 ms. The daughter nucleus of the decay is ^{12}C where both the ground state and several excited states are populated. If the populated state has an excitation energy above the α emission threshold, there is a large probability that the ^{12}C nucleus breaks apart and emits three low-energetic α particles. The α particles are detected in an array of pixel-detectors and both energies and momenta of the three particles can be determined. The observed three-particle state is represented in the so-called Dalitz plot. A sequential decay model is combined with the well-established R-matrix formalism and with the help of Monte Carlo simulations the theoretical model is compared to the experimental data. It is concluded that the excitation spectrum between 8 MeV and 12 MeV is dominated by resonances with $J^\pi = 0^+$ which decay sequentially to the ground state of ^{8}Be through emission of an α particle with $L = 0$. The spectrum between 12 MeV and 15 MeV is, on the other hand, dominated by a 2^+ state ($\sim$ 66 % of the spectrum) and a 0^+ state ($\sim$ 25 % of the spectrum) which both decay to the first excited state in ^{8}Be through emission of an α particle with $L = 2$. The remaining part of the decays in this energy range go through the ground state in ^{8}Be. A famous 2^+ state at an excitation energy of 10 MeV, predicted in 1956 and observed for the first time in 2013, cannot be unambiguously identified in the present experiment.

Contents

1

INTRODUCTION

Since the 1950s the ^{12}C nucleus has attracted quite some attention from nuclear physicists and astrophysicists. There are multiple reasons to investigate ^{12}C, some of which are presented in this chapter, together with a historical overview of the most important ideas and experimental results related to this nucleus and, especially, its broad resonances above the α particle threshold.

1.1 BROAD RESONANCES IN ^{12}C

The Hoyle state is without question the most famous level in ^{12}C. Not only is its discovery a prime example of interplay between astronomy and nuclear physics, but the properties of the Hoyle state have proven extremely difficult to explain in many, otherwise very succesful, theoretical frameworks.

1.1.1 Discovery of the Hoyle state

In the beginning of the 1950s it was still mysterious how elements heavier than ^{4}He were produced, since no stable isotopes exist with mass numbers 5 and 8. Still, ^{12}C is the fourth-most abundant isotope in the universe (Rolfs and Rodney 1988), so clearly some mechanism exists that enables the circumvention of these gaps. The solution was proposed by (Öpik 1951) and (Salpeter 1952): The stellar triple-α reaction. The theory was that the energetic α particles, which are zooming around in the stellar plasma, collide and form ^{8}Be, however, ^{8}Be is unstable and breaks up into two α particles again with a life-time of $\tau \sim 10^{-16}$ s.

With such a long life-time an equilibrium is established with a density ratio of $N(^8\mathrm{Be})/N(^4\mathrm{He}) \sim 5.2 \times 10^{-10}$ (assuming a temperature of $T_6 = 100$ and a density of $\rho = 10^5\,\mathrm{g\,cm^{-3}}$). This concentration is high enough that there is a non-negligible probability that a third α particle collides with a ^{8}Be nucleus and forms ^{12}C, i.e.

$$\alpha + \alpha + \alpha \rightleftharpoons {}^8\mathrm{Be} + \alpha \rightleftharpoons {}^{12}\mathrm{C}^* \rightarrow {}^{12}\mathrm{C} + \gamma. \tag{1.1}$$

It was shown by Fred Hoyle that this mechanism could not explain the large observed abundance of ^{12}C unless the α capture on ^{8}Be proceeded resonantly through a then unobserved state in ^{12}C. Hoyle calculated the energy of this state to be 7.68 MeV above the ground state of ^{12}C (Hoyle et al. 1953). The state was shortly afterwards seen in a $^{14}\mathrm{N}(d,\alpha)^{12}\mathrm{C}$ experiment by Hoyle's colleagues, and the energy and width were determined to $E = 7.68(3)\,\mathrm{MeV}$ and $\Gamma < 25\,\mathrm{keV}$, see (Dunbar et al. 1953). In this way, knowledge about the universal isotopic abundances, together with the hypothesis of the stellar triple-α reaction, led directly to a very precise prediction about nuclear structure, which is rather remarkable. The state was later investigated in a ^{12}B β decay experiment by (Cook et al. 1957) where the spin and parity were established to be $J^\pi = 0^+$. A more detailed account of the prediction and discovery of the Hoyle state is presented in (Kragh 2010).

1.1.2 Early experimental efforts

Not long after the existence of the Hoyle state had been experimentally confirmed what looked like a broad resonance at $E = 10.1(2)\,\mathrm{MeV}$ with a width of $\Gamma \simeq 2.5\,\mathrm{MeV}$ was observed by (Cook et al. 1958). The spin and parity was determined as either 0^+ or 2^+. It was shown by (F. C. Barker and Treacy 1962) that the Hoyle state, with its observed width of $\Gamma^{\mathrm{obs}} = 8.5(10)\,\mathrm{eV}$ was sufficiently broad that an associated ghost structure (see Section 2.3) would appear in the same energy region as the observed resonance. The accessible energy range was extended by (Wilkinson et al. 1963), who used the β decay of ^{12}N to populate the resonances of ^{12}C. These authors concluded that the ghost of the Hoyle state could not account for the entire resonant strength above the α particle threshold, and that the spectrum was most accurately fitted by the ghost contribution in

addition to two resonances at approximately 10 MeV and 12 MeV, respectively. Assuming the two-level scheme, the β decay to the higher resonance would have a $\log(ft) \approx 4.6$, indicating it to be an allowed transition and therefore of even parity. The parameters for the 10 MeV resonance that appear in the (Ajzenberg-Selove 1990) evaluation are based on another β decay experiment by (Schwalm and Povh 1966), see also Table 1.1.

Table 1.1: The low-energy levels in ^{12}C from the most recent evaluation, (Ajzenberg-Selove 1990). The spin-parity assignments in parantheses are tentative. See Figure 3.1 for a graphical level diagram.

E (keV)	J^π, T	Γ^{obs} (keV)
0	0^+, 0	-
4438.91(31)	2^+, 0	$10.8(6) \times 10^{-6}$
7654.20(15)	0^+, 0	$8.5(10) \times 10^{-3}$
9641(5)	3^-, 0	34(5)
10 300(300)	(0^+), 0	3000(700)
10 844(16)	1^-, 0	315(25)
(11 160(50))	(2^+), 0	430(80)
11 828(16)	2^-, 0	260(25)
12 710(6)	1^+, 0	$18.1(28) \times 10^{-3}$
13 352(17)	(2^-), 0	375(40)
14 083(15)	4^+, 0	258(15)
15 110(3)	1^+, 1	$43.6(13) \times 10^{-3}$

1.1.3 Phenomenological theories

In 1956 Morinaga put forward a hypothesis that would link some of the properties of the lighter, self-conjugate, nuclei, i.e. ^{16}O, ^{20}Ne and ^{24}Mg, (Morinaga 1956). In all these nuclei there are excited 0^+ levels not very far above the ground state, and these 0^+ states seem to be accompanied by a 2^+ level at slightly higher energy. Morinaga's conjecture was that the 0^+ levels should be interpreted as band heads for rotational bands, to which the 2^+ levels also belonged. The small

0^+-2^+ energy spacing seemed to indicate very large moments of inertia, and the states were therefore expected to be very spatially extended. In fact, Morinaga showed that the inferred moments of inertia were consistent with a chain-like structure of α particles. If the structure of the Hoyle state could be explained as a chain of three α particles, we should expect to observe the rotationally excited 2^+ state at an excitation energy of around 10 MeV in ^{12}C. When a broad resonant structure was observed in this energy region and assigned $J^\pi = 0^+$ or 2^+, (Cook et al. 1958; Wilkinson et al. 1963), Morinaga therefore argued that the resonance should be assigned $J^\pi = 2^+$, (Morinaga 1966).

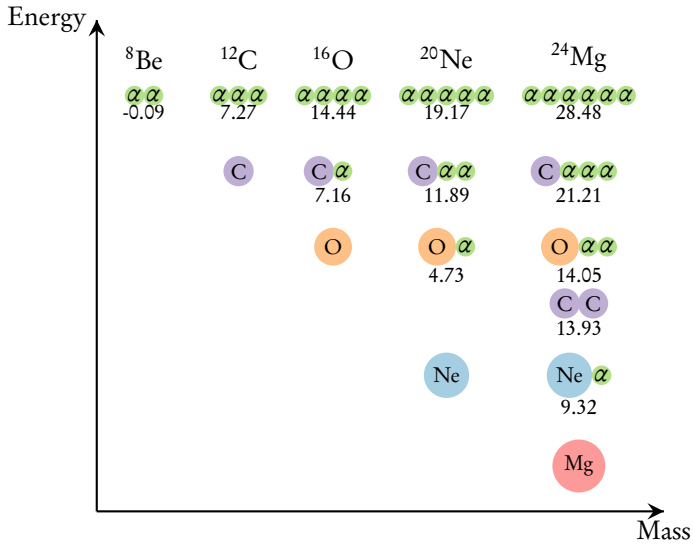

Figure 1.1: A so-called Ikeda diagram after (Ikeda et al. 1968). The threshold energy in MeV is marked below each cluster configuration.

Along the same lines as Morinaga's α-chain picture (Ikeda et al. 1968) suggested a more general scheme of formation of clusterised states near particle threshold. A sketch of the principle applied to α thresholds in light, self-conjugate, nuclei is shown in Figure 1.1. The idea is that near particle thresholds it becomes energetically possible to form cluster configurations or molecule-like states with

constituents corresponding to the threshold. The clusterised states near α thresholds are then also expected to have a large reduced α width (for an explanation of the concept of reduced width, see Section 2.2.1). Since the stellar triple-α process is completely dependent on such states, namely the ^{8}Be ground state and the Hoyle state in ^{12}C this pattern has quite far reaching consequences, see Section 1.2. The observed α width of the Hoyle state was indeed shown by (F. C. Barker and Treacy 1962) to correspond to an extremely large reduced width of $\sim 1.5\,\hbar^2/(2M_c a_c)$, i.e. larger than the single-particle limit.

1.1.4 Modern theories

That the Hoyle state should have a peculiar structure is supported by the fact that many theoretical models do not reproduce its properties correctly. In the shell model calculation by (Cohen and Kurath 1965), for instance, the Hoyle state had to be excluded from the analysis, and the authors concluded that the state could not be explained with single-particle excitations alone, and probably contained a large fraction of 2p2h-excitation. In a more modern ab initio calculation using the no-core shell model and similarity renormalisation group methods the Hoyle state is still problematic, appearing at an energy $\sim 5\,\mathrm{MeV}$ higher than the experimental value, (Roth et al. 2011). This is a sign that the wave function of the Hoyle state is almost orthogonal to the harmonic-oscillator basis states used in the calculation, and that the truncation in main quantum number is not justified for this state.

Some theories that more easily allow many-particle correlations and clusterisation have met with more success: In a work using *Anti-symmetrised Molecular Dynamics* (AMD) by (Kanada-En'yo 2007) many properties of the ^{12}C ground state and excited states were calculated, and the obtained mass density distribution for the Hoyle state indeed shows a large degree of clusterisation. Furthermore, the 2^+ state that Morinaga predicted to exist as a rotational excitation of the Hoyle state at around 10 MeV is also predicted in the AMD-framework. The Hoyle state and the rotationally excited 2^+ state also came out of a lattice calculation with *Chiral Effective Field Theory* (Ch-EFT) by (Epelbaum et al. 2012). Here, the ground state of ^{12}C appeared to be well described as a close, triangular arrangement of α particles, while the Hoyle state was better described as a

bent-arm structure, very similar to Morinaga's α chain picture. The 2^+_1 and 2^+_2 states are then interpreted as rotational excitations of the two arrangements of α clusters.

In fact, many states in ^{12}C can be explained in a framework that explicitly assumes clusterisation, see (Wheeler 1937; Bijker and Iachello 2000). In this model the ground state is assumed to have the structure of an equilateral triangle with an α particle in each corner. From the symmetry properties alone ($U(7)$) of such a system it is possible to generate an entire ro-vibrational spectrum for ^{12}C. This idea recently recieved some support by the discovery of a 5^- state at 22.4(2) MeV that fits very well into the ground state rotational band, (Marín-Lámbarri et al. 2014). The Hoyle state is interpreted as a vibrational excitation of the breathing-mode vibration of the triangular configuration, and the first rotational excitation of the Hoyle state results in a 2^+ state at around 10 MeV, in fine agreement with the predictions from AMD and Ch-EFT.

1.1.5 β-decay experiments

With several modern theoretical calculations predicting a 2^+ rotational excitation of the Hoyle state to exist at around 10 MeV and new experimental techniques emerging, a second wave of experiments were initiated specifically in order to characterise the broad, resonance-like, structure above the Hoyle state.

The total energy spectrum af ^{12}C populated in ^{12}B and ^{12}N β-decay experiments was measured in complete kinematics, i.e. using position- and energy-sensitive silicon detectors to detect all three α particles emitted in the breakup of the ^{12}C resonances, by (Fynbo et al. 2005). An R-matrix expression was fitted to the spectrum (see also Section 2.2.3) and it was concluded that most of the 10 MeV structure was 0^+, based on the strong distortion of the lineshape caused by interference with the high-energy tail of the Hoyle state, an interference which would not appear if the spectrum was dominated by 2^+. It was also noted that the resonant strength seemed to extend all the way up to the highest energy allowed by the β decay Q-value, indicating a broad resonance at higher energy. The lack of interference with the other resonances led to a 2^+ assignment of this state. The R-matrix fit resulted in $E(0^+) = 11.23(5)$ MeV, $\Gamma(0^+) = 2.5(2)$ MeV and $E(2^+) = 13.9(3)$ MeV, $\Gamma(2^+) = 0.7(3)$ MeV. Even though some 2^+ strength

were observed, the energy is so high that it is inconsistent with an interpretation as the rotationally excited Hoyle state.

Data from another complete kinematics experiment with the β-delayed α breakup of ^{12}B and ^{12}N were analysed in terms of the phase space distribution of the α particles, (Diget et al. 2009). The approach is very similar to the one we shall follow in the present work but was, however, quite limited in terms of counting statistics. It was found that the breakup of the resonance around 10 MeV was consistent with a 0^+ resonance breaking up sequentially through the ^{8}Be(0^+) ground state (see also Section 3.2.2). At excitation energies higher than 12.7 MeV the phase space distributions were consistent with a 2^+ resonance breaking up through the first excited 2^+ state in ^{8}Be by emission of a d-wave α particle, in agreement with the results from (Fynbo et al. 2005).

A very high-statistics measurement of the β-delayed α spectrum ^{12}B and ^{12}N was made by implanting the radioactive ions in a thin, segmented silicon detector, and the data were, together with the data from the experiment by (Diget et al. 2009) included in a very elaborate R-matrix fit by (Hyldegaard et al. 2010). Evidence was found for both a broad 0^+ resonance and a broad 2^+ resonance, co-existing in the energy region around 11 MeV with parameters $E(0^+) = 11.2(3)$ MeV, $\Gamma(0^+) = 1.5(6)$ MeV and $E(2^+) = 11.1(3)$ MeV, $\Gamma(2^+) = 1.4(4)$ MeV. Both 0^+ and 2^+ components were used to describe the resonant strength above 12.7 MeV.

1.1.6 Other experimental probes

Even if the discussion has so far been focused on β-decay experiments there are other methods that can be used to probe the excited states of ^{12}C. The challenges that have to be overcome are mainly related to unwanted background from other resonances in the 9 MeV–12 MeV region, see Table 1.1. Selectivity is therefore the key to any succesful experiment that has the goal of measuring a broad 2^+ state at this energy.

Data from inelastic p- and α-scattering experiments, (Freer et al. 2009; Itoh et al. 2011), were simultaneously analysed in the paper by (Freer et al. 2012). Both experiments employed a magnetic spectrometer and any 0^+ resonant strength was suppressed by two orders of magnitude by careful selection of scattering

angle with the spectrometer. A small signal that could not be attributed to the known resonances in ^{12}C was fitted to the single-level R-matrix line shape for a 2^+ resonance, and the extracted parameters for the 2^+ signal was $E(2^+) = 9.75(15)\,\mathrm{MeV}$, $\Gamma(2^+) = 0.75(15)\,\mathrm{MeV}$, making this state an obvious candidate for the rotationally excited Hoyle state. One could doubt the robustness of this result, since the signal is quite weak and sits on top of a large background. If, on the other hand, the analysis is sound enough, the result is clearly inconsistent with the state found in the β-decay experiments, suggesting that multiple 2^+ states should exist in the energy region of interest. If this is the case, then it should be possible to observe interference phenomena, and fitting to a single-level line shape is not appropriate.

Clear identification of a 2^+ state at the right energy for a rotational excitation of the Hoyle state was presented by (Zimmerman et al. 2013). Here, ^{12}C was excited by a γ-ray beam and the products of the photodisintegration were measured in an optical time projection chamber. The selection rules for electromagnetic transitions strictly exclude population of 0^+ strength, and the most troubling background is effectively removed. A resonance was observed at $E(2^+) = 10.03(11)\,\mathrm{MeV}$, $\Gamma(2^+) = 0.80(13)\,\mathrm{MeV}$. Breakups that proceed sequentially through the ground state of ^{8}Be is identified by requiring the three emitted α particles to be almost collinear, with the first emitted particle (α_0) possessing two thirds of the kinetic energy. The $\gamma\alpha_0$ angular correlations are in fine agreement with a 2^+ assignment to the measured state.

1.2 STELLAR HELIUM BURNING

Since the subject of stellar He burning is closely related to nuclear levels with large α widths near the α particle threshold, a short introduction is appropriate. A more detailed discussion is found in (Rolfs and Rodney 1988).

When dealing with stellar fusion processes, it is important to understand the concept of the *Gamow window*, which is the energy region, or "window", where the fusion reactions typically takes place. In connection with He burning, we have the α particles together with ^{8}Be, ^{12}C and ^{16}O, moving around with thermal velocity distributions. The relative velocities of the α particles and

the heavier ions, and therefore also their relative energies, are determined by the *Maxwell-Boltzmann* distribution. On the other hand, the Coulomb repulsion between the ions constitute a potential barrier, and the ions must penetrate this barrier in order for a reaction to take place. The probability for this to happen is proportional to the *penetrability*, which is a strong function of energy, see Section also 2.2.1. It is the product of the thermal energy distribution and the penetrability that determines the reaction rate. The result is a peak in the reaction rate, known as the Gamow peak or the Gamow energy window, the position of which can be calculated as

$$E_0 = \left[\left(\frac{\pi}{\hbar} \right)^2 \left(\frac{Z_1 Z_2 e^2}{4\pi\epsilon_0} \right)^2 \left(\frac{m}{2} \right) (kT)^2 \right]^{\frac{1}{3}}. \tag{1.2}$$

Quiescent He burning typically takes place at a temperature of 0.1 GK, where the thermal energy distribution peaks at $kT \sim 10$ keV, however, taking the $^4\mathrm{He}(\alpha,\gamma)^8\mathrm{Be}$ reaction as example, the Gamow window is at around 100 keV.

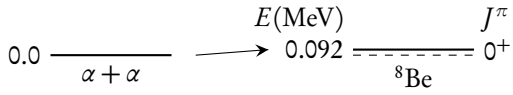

Figure 1.2: The first step of stellar He-burning.

The production of the light, self-conjugate nuclei, i.e. those nuclei which can be broken into a whole number of α particles, is relatively easy to explain by a sequence of α-capture reactions in the He rich environments of large stars. During quiescent He burning the temperature typically reaches $T \sim 0.1$ GK in the parts of the star where the nuclear fusion takes place. The first step of He burning is shown in Figure 1.2, where two α particles fuse and form ^{8}Be. The process is greatly facilitated by the fact that for $T \sim 0.1$ GK the ground state of ^{8}Be sits in the middle of the Gamow window for this reaction. Furthermore, the ^{8}Be ground state has natural spin-parity, and the capture can proceed resonantly.

As Hoyle showed, the next step in stellar He burning is the resonant $^8\mathrm{Be}(\alpha,\gamma)^{12}\mathrm{C}$ reaction. This reaction is also enhanced by a state of natural spin and parity in the Gamow-window, which explains the large universal abundance of ^{12}C.

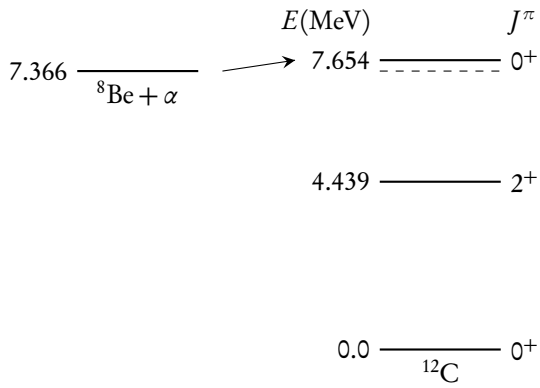

Figure 1.3: The second step of stellar He-burning.

If the next step was also resonantly enhanced, we would expect all the ^{12}C to be used up as fuel for the production of ^{16}O. In turn, we would also not be here to worry about it. If we take a look at Figure 1.4, however, we see that there are no natural spin-parity states in, or even near, the Gamow-window for this reaction, which is at ~ 300 keV. This is the fact that to a large extent allows ^{12}C to survive the He burning stages in the stars. That the $^{12}C(\alpha,\gamma)^{16}O$ is not completely blocked at this point is due to a mechanism, which we have not yet discussed, namely capture through sub-threshold states.

It turns out that several levels in ^{16}O play a rôle in the $^{12}C(\alpha,\gamma)^{16}O$ reaction, the dominating contribution coming from the 2^+ level at 245 keV below the α particle threshold. That capture through sub-threshold states is possible may seem surprising, but is related to the finite width of nuclear levels. The high-energy tail of a level may extend to energies above the threshold and contribute to the reaction cross section. In the case of $^{12}C(\alpha,\gamma)^{16}O$ the 2^+ level at 6.9 MeV is responsible for approximately half of the α capture cross section, while the 1^- level at 7.1 MeV (45 keV below the threshold) provides the other half. On top of this there is also interference effects between the sub-threshold and the 9.6 MeV 1^- levels involved. This rather complicated scheme makes it challenging to predict the reaction cross section at stellar temperatures, and the properties

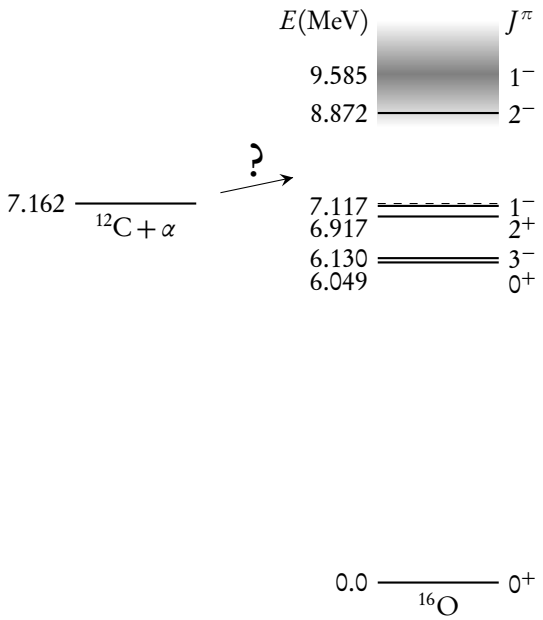

Figure 1.4: ^{12}C is converted to ^{16}O

of the involved levels must be very well determined in order to make accurate calculations. The reaction has therefore attracted quite a lot of attention from astrophysicists, and it is known as the *holy grail of astrophysics*. A more detailed discussion of this reaction can be found in (Refsgaard et al. 2016)

The next, natural step would be the $^{16}O(\alpha,\gamma)^{20}Ne$ reaction, however, the only ^{20}Ne resonance in the Gamow window is a 2^- state, and all natural parity states that could potentially contribute to the reaction cross section, are quite narrow. The ashes that remain after the quiescent He burning phase of a star are therefore primarily ^{12}C and ^{16}O.

2

NUCLEAR PHENOMENOLOGY

Since this is an experimental work we shall not concern ourselves with detailed theoretical derivations, however, to make the thesis more readable, also for non-experts, I think it is useful to include a short introduction of some of the theoretical concepts that we use in later chapters. We could call it *Nuclear theory for pedestrians*. In addition this chapter includes some of the formulas that are most often used in the practical application of R-matrix analysis.

2.1 RESONANCES

The ultimate goal of this work is to characterise resonances in ^{12}C. But what do we understand by a "resonance", and how do we expect to be able to measure it? Well, a typical way to learn more about a nucleus is to bombard it with some projectile and see what happens. In the middle of the thirties it was shown experimentally that the neutron capture cross sections of various nuclei had a strong energy dependence and exhibited very narrow peaks, see (Amaldi and Fermi 1936; Frisch et al. 1936). This observation led to several papers suggesting the existence of long-lived, unbound states in these nuclei, which could account for the pronounced resonant behaviour of the capture, (Bohr 1936; Breit and Wigner 1936). Based upon the long life-times and the large probability of neutron capture, compared to the probability of scattering, it was also argued that the unbound states could not have the configuration of an energetic neutron moving in some mean-field potential of the target nucleus, but instead should be explained as complex, collective excitations of the nucleons of the compound

system. This viewpoint is represented in Bohr's *bowl of balls* model, see (Bohr 1937).

That resonances should appear in the capture cross section can be understood in a relatively simple picture. Following the discussion in (Blatt and Weisskopf 1952), imagine a neutron-nucleus system with a constant potential of $-V$ inside the interaction radius, i.e. for $r < a$, and zero potential for $r > a$. Assume also that the compound system can decay only through re-emission of the neutron. This means that if we have an ingoing neutron flux inside the nuclear radius there must also be an outgoing flux of equal amplitude, such that the wave function becomes

$$u_< = c[\exp(-iKr) + \exp(i(Kr + 2\zeta))] = C\cos(Kr + \zeta), \tag{2.1}$$

where ζ is the phase shift of the outgoing wave caused by the detailed interactions between the neutron and the other nucleons.

If we only consider s-wave neutrons, the outside wave function can be written as

$$u_> = A\sin(kr + \delta), \tag{2.2}$$

where A is adjusted to obtain unit incoming flux. Requiring the total wave function to be continuous and smooth at $r = a$ leads to a solution for given values of K, k and ζ. Since $K \gg k$, we find the amplitude of the internal wave function to be quite small for most values of ζ, however, if the derivative of the wave function is zero at $r = a$ it is possible to have equal amplitudes inside and outside the nuclear boundary, see the examples in Figure 2.1. We note that far away from resonance the wave function looks almost as if it had been reflected by a hard sphere of radius a.

It is seen that only for a set of discreet values of ζ does the wave function penetrate considerably into the core of the nucleus, allowing interactions to take place. With ζ being a function of energy, it makes sense that neutron capture cross sections, and indeed any reaction cross sections, can show sharp peaks as function of the energy of the projectile. This simple analysis does not in itself show that resonances in the cross sections are related to any particular, physical state of the compound nucleus, such as the long-lived states of collective

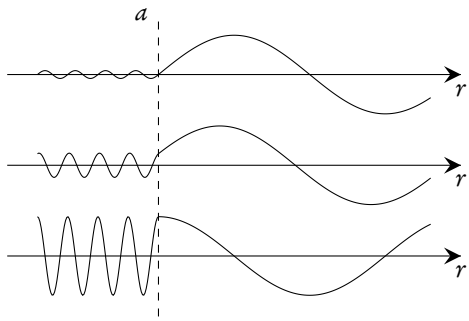

Figure 2.1: Sketch of a hypothetical neutron wave function far away from resonance (top), close to resonance (middle) and on resonance (bottom).

excitation mentioned above, but penetration of the projectile into the nucleus is necessary for any interaction to take place and thus for the formation of a resonant state.

In nuclear physics there are two mechanisms that are relevant for the existence of long-lived unbound states: The potential barrier from Coulomb and angular momentum repulsion forms a classically forbidden region outside the nuclear core, which suppresses the coupling between the core and the continuum. The other mechanism is of statistical nature and related to Bohr's bowl-of-balls model. If an impending projectile is absorbed in the compound system its energy is quickly distributed between the nucleons in a collective excitation. The probability that the excitation energy is concentrated again on a single nucleon is very small and a long time can pass before a nucleon gets enough energy to escape the system (Weinberg 1996). The resonances associated with these two mechanisms are called *Shape*-resonances and *Feshbach*-resonances, respectively. In nuclear physics, the distinction between these types is rarely seen, as nuclear resonances are usually some kind of mixture between the two.

2.2 R-MATRIX ANALYSIS

The *R*-matrix framework has been used for seven decades to interpret experimental data from nuclear reactions. A review of the *R*-matrix framework can be found in the classic paper by (Lane and Thomas 1958). The approach can be qualitatively understood by analogy to a system of wave guides connected to a resonating cavity, as illustrated in Figure 2.2. The cavity, which is the analogue

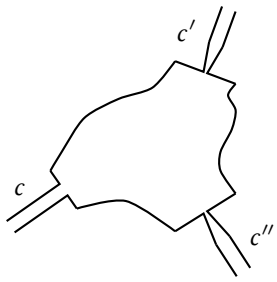

Figure 2.2: The compound nucleus is compared to a resonating cavity connected to several wave guides.

of the compund nucleus, can be excited by incoming waves in each of the three wave guides, c, c' and c'', also known as *channels* in the *R*-matrix formalism. The excited compound system can subsequently de-excite through emission of outgoing waves through any of the open channels. These channels correspond to different projectile-target combinations forming the same compound system or different relative angular momenta of the projectile and target.

The analogy can even be taken a step further and related to the discussion in Section 2.1. In Figure 2.2 there is a sudden change in the cross section at the junction between the wave guides and the cavity, which leads to an abrupt change in the "impedance". This impedance mismatch is equivalent to the condition $K \ll k$ in the earlier discussion and leads to a partial reflection of the incoming wave.

We know that charged particles, or particles of non-zero angular momentum, see a rising potential barrier as they approach the target nucleus. This barrier also leads to some reflection of an incoming wave. If the relative energy

of the projectile and target is smaller than the height of the barrier the wave function becomes exponentially damped after the classical turning-point, however, still with a possibility of forming the compound system. In Figure 2.2 channel c could represent an $l = 0$ neutron channel, while c' and c'' are charged particle channels or channels with $l \neq 0$.

The goal of R-matrix analysis is to find a way of predicting the amplitude going out in a channel, c, given an incoming wave in another channel, c', i.e. the cross section $\sigma_{cc'}$.

2.2.1 *The formalism*

The idea is to divide space into two regions, separated at the nuclear boundary $r = a$: An external region where the particle pair in the projectile-target system interacts only through the Coulomb force, and an internal region where the nuclear forces dominate. The boundary may vary from channel to channel such that we are dealing with a set, a_c. The a_c's are therefore also referred to as *channel radii*. For a particle pair, $B + b$, the channel radius is often chosen near the size of the nuclei:

$$a_c = r_0(A_B^{1/3} + A_b^{1/3}) \quad , \qquad r_0 \approx 1.4\,\text{fm}. \tag{2.3}$$

The behaviour of the internal interactions of the compound system is parametrised in terms of a number of levels, labelled λ, their energies, E_λ, and how strongly they couple to each channel, described by the *reduced width amplitudes*, $\gamma_{\lambda c}$. Incidentally these levels are also known as *resonances*. We define the levels to be eigenfunctions of the internal hamiltonian with eigenenergies E_λ, i.e. $HX_\lambda = E_\lambda X_\lambda$, such that we can expand the total, internal wave function as

$$\Psi = \sum_\lambda C_\lambda X_\lambda. \tag{2.4}$$

The coupling strength of a level, λ, to a channel, c, is basically determined by the overlap between X_λ and a pure channel wave function, ϕ_c, and we define

$$\gamma_{\lambda c} = \sqrt{\frac{\hbar^2}{2M_c a_c}} \int \phi_c^* X_\lambda dS \tag{2.5}$$

where the integration is over the nuclear boundary surface and M_c is the reduced mass of the channel. If we consider a level in the compound nucleus ${}^{A}Z$ and take a neutron channel as example, $\gamma_{\lambda c}^2$ is proportional to the probability of forming the ${}^{A-1}Z + n$ pair at a separation of a_c and has units of keV.

The coupling between a level and a channel is not, however, only determined by the internal properties of the system, as Equation (2.5) could lead one to expect. The reason is the Coulomb and angular momentum barriers, in the presence of which it is not enough for a level to easily form the appropriate particle pair on the channel surface, the pair must also penetrate the barriers. Therefore, the *partial width* is defined

$$\Gamma_{\lambda c} = 2P_c(E_\lambda)\gamma_{\lambda c}^2, \tag{2.6}$$

where P_c is called the *penetrability* and proportional to the probability of transmission through the potential barriers. Like the reduced width, the partial width is expressed in units of keV, and the sum of the partial widths constitute the total width of a level, $\Gamma_\lambda = \sum_c \Gamma_{\lambda c}$.

It is possible in the R-matrix framework to derive expressions for reaction cross sections. Most of these are quite complicated and not very useful in this qualitative discussion. In sufficiently simple situations, i.e. if only a single, isolated level is considered, the standard *Breit-Wigner* form of the cross section is recovered. For scattering between channel c and c' this is

$$\sigma_{cc'} \sim \frac{\Gamma_{\lambda c}\Gamma_{\lambda c'}}{(E - E_r)^2 + \frac{1}{4}\Gamma_\lambda^2}. \tag{2.7}$$

If the width of the level is sufficiently small, such that the energy dependence of the $\Gamma_{\lambda c}$'s can be ignored, then it will show itself as a resonance in the cross section at $E = E_r$, where

$$E_r = E_\lambda + \Delta_\lambda(E_r). \tag{2.8}$$

We realise that the *observed* resonance energy, E_r, is not equal to the eigenenergy

of the level, E_λ, but is shifted by the *level shift*, Δ_λ. The level shift is given by

$$\begin{aligned}\Delta_\lambda(E) &= \sum_c \Delta_{\lambda c}(E) \\ \Delta_{\lambda c}(E) &= -(S_c(E) - B_c)\gamma_{\lambda c}^2,\end{aligned} \tag{2.9}$$

where the $S_c(E)$ is the *shift function* and B_c is the boundary condition imposed on the logarithmic derivative of the wave function on the nuclear boundary. If several levels are coupled to the same channel, a customary choice is to set $B_c = S_c(E_1)$, where E_1 is the observed energy of the lowest-energy level. Looking at Equation (2.9) we see that this choice of B_c results in equality between the formal and observed energy of this level.

The distinction between formal and observed parameters not only applies to the level energies, but also to the level widths. The relations are

$$\begin{aligned}(\gamma_{\lambda c}^{\text{obs}})^2 &= \frac{\gamma_{\lambda c}^2}{1 + \sum_c \gamma_{\lambda c}^2 \frac{dS}{dE}\big|_{E_r}} \\ \Gamma_{\lambda c}^{\text{obs}} &= 2P_c(E_r)(\gamma_{\lambda c}^{\text{obs}})^2.\end{aligned} \tag{2.10}$$

From Equations (2.9) and (2.10) we note that the difference between formal and observed parameters is only substantial if very broad levels are considered, i.e. if the reduced width is large. It has been proposed by (Brune 2002) to re-formulate the R-matrix framework in terms of the observed parameters. Since the observed parameters are independent of the (more or less arbitrary) choice of a_c and B_c such an approach would greatly facilitate the comparison of results from different calculations.

In practice, experimental data are often interpreted by fitting to the R-matrix expressions, using $\gamma_{\lambda c}$ and E_λ (and sometimes also a_c) as fitting parameters. The resulting $\gamma_{\lambda c}$'s are sometimes used not only as meaningless fitting parameters, but also as a means to understand the structure of the levels. As mentioned in connection with the definition in (2.5), the reduced width $\gamma_{\lambda c}^2$ is a measure of how much level λ "looks like" the pure configuration corresponding to channel c. One can then start to speculate as to whether a level with a large α particle width contains pre-formed α particles within the nuclear boundary...

2.2.2 *The toolbox*

We have encountered some functions, namely the penetrability and the shift function, that need to be evaluated in almost any problem involving R-matrix calculations. These functions are determined by conditions in the external region exclusively and are therefore (relatively) trivial to calculate:

$$P_c(E) = \begin{cases} \dfrac{\rho}{F_l^2(\eta,\rho) + G_l^2(\eta,\rho)} & E > 0 \\ 0 & E < 0 \end{cases} \tag{2.11}$$

$$S_c(E) = \begin{cases} \dfrac{\rho[F_l(\eta,\rho)\dot{F}_l(\eta,\rho) + G_l(\eta,\rho)\dot{G}_l(\eta,\rho)]}{F_l^2(\eta,\rho) + G_l^2(\eta,\rho)} & E > 0 \\ \dfrac{\rho\,\dot{W}_{-\eta,l+\frac{1}{2}}(2\rho)}{W_{-\eta,l+\frac{1}{2}}(2\rho)} & E < 0 \end{cases} \tag{2.12}$$

where F_l and G_l are the regular and irregular Coulomb functions, respectively, and W is the Whittaker W-function. A dot indicates derivation with respect to ρ. l is the orbital angular momentum of the channel and η and ρ are defined by

$$\begin{aligned} \rho &= k a_c \\ \eta &= \frac{Z_1 Z_2 e^2 M_c}{\hbar^2 k} \qquad \text{(the } \textit{Sommerfeld}\text{-parameter)} \\ k &= \sqrt{\frac{2M_c|E|}{\hbar^2}}. \end{aligned} \tag{2.13}$$

Details about the behaviour of Coulomb and and Whittaker functions can be found in (Abramowitz and Stegun 1965). The numerical implementation for evaluation of the Coulomb functions used in this work is the one presented in (Michel 2007).

2.2.3 *Application to β-delayed particle breakup*

The *R*-matrix formalism was originally developed to treat particle capture and emission. It was later extended (though not in any rigourous fashion) to incorporate also β-delayed particle emission by (F. C. Barker 1969). In the resonating cavity picture, it is basically a question of adding two inbound channels to the cavity in Figure 2.2, one for Fermi transitions and one for Gamow-Teller transitions. Since the β-delayed α spectrum of ^{12}N and ^{12}B has been analysed in great detail with this method, for instance by (Hyldegaard et al. 2010), it is worthwhile to quote a few of the formulas here. Following the notation of (F. C. Barker and Warburton 1988) we let $N(E)$ describe the spectrum of delayed particles, such that $\int N(E)dE = N$. If there are more than one open particle channel, $N(E) = \sum_c N_c(E)$. The following relates the *R*-matrix parameters of the daughter nucleus to the observed particle spectrum:

$$N_c(E) = f_\beta P_c(E) \sum_x \left| \sum_{\lambda\mu} B_{\lambda x} \gamma_{\mu c} A_{\lambda\mu} \right|^2 . \tag{2.14}$$

Here, f_β is the phase space factor of the β decay, $x = \{\mathrm{F},\mathrm{GT}\}$, $B_{\lambda x}$ is the β feeding of level λ (the β width of the level, so to speak) and $A_{\lambda\mu}$ is the *level matrix*, defined by

$$(A^{-1})_{\lambda\mu} = (E_\lambda - E)\delta_{\lambda\mu} - \sum_c \left[S_c(E) - B_c + iP_c(E) \right] \gamma_{\lambda c} \gamma_{\mu c}. \tag{2.15}$$

The expression in Equation (2.14) treats the many-level case, and correctly includes the effect of interference between levels.

As a sidenote, the method has also been applied to other interesting cases, most boldly perhaps to the $^{12}\mathrm{C}(\alpha,\gamma)^{16}\mathrm{O}$ reaction, where the reaction cross section has been calculated from *R*-matrix parameters found through fits to the β-delayed α spectrum of ^{16}N, (F. C. Barker 1971; Azuma et al. 1994; Tang et al. 2010).

2.3 GHOSTS

In both the ^{12}C and ^{8}Be systems a certain effect, known by the colourful name "ghost" or "ghost anomaly", plays an important rôle in the interpretation of the spectra. The effect of ghosts in these nuclei has been discussed in several papers, see for instance (F. C. Barker and Treacy 1962; Wilkinson et al. 1963; Szczurek et al. 1991), and it is related to resonances situated near particle thresholds.

In the single-level approximation of (Lane and Thomas 1958), consider the total wave function, Ψ_c, of the particle pair of channel c with unit incoming flux. We find the probability to form a nuclear resonance through channel c by integrating the wave function over the internal region:

$$\int_\tau |\Psi_c|^2 d\tau = \frac{\hbar\Gamma_{\lambda c}}{(E_\lambda + \Delta_\lambda - E)^2 + \frac{1}{4}\Gamma_\lambda^2}. \tag{2.16}$$

If c is the only open channel we have

$$\begin{aligned} \Delta_\lambda &= \Delta_{\lambda c} = -(S_c(E) - B_c)\gamma_{\lambda c}^2 \\ \Gamma_\lambda &= \Gamma_{\lambda c} = 2P_c(E)\gamma_{\lambda c}^2. \end{aligned} \tag{2.17}$$

With the parameters for the ^{8}Be ground state given in Table 3.1 we can calculate this probability for the $\alpha + \alpha$ channel and the result is shown in Figure 2.3. The result is remarkable in the sense that we only consider a single nuclear level, but in the spectrum we observe two peaks, one narrow peak at the resonance energy, E_λ, and a very broad peak at $\sim 700\,\mathrm{keV}$. The broad peak appears because the penetrability, $P_c(E)$, in the energy range between 100 keV and 700 keV grows faster than the Breit-Wigner function falls off. The extra peak is therefore a natural part of the ground state line shape, and the mystical connotations of the "ghost"-name are perhaps not entirely justified.

In ^{12}C we also find a resonance very close to the α particle threshold, namely the Hoyle state. It is possible to explain a significant fraction of the broad, resonant strength in ^{12}C as the Hoyle state ghost, see (Fynbo et al. 2005).

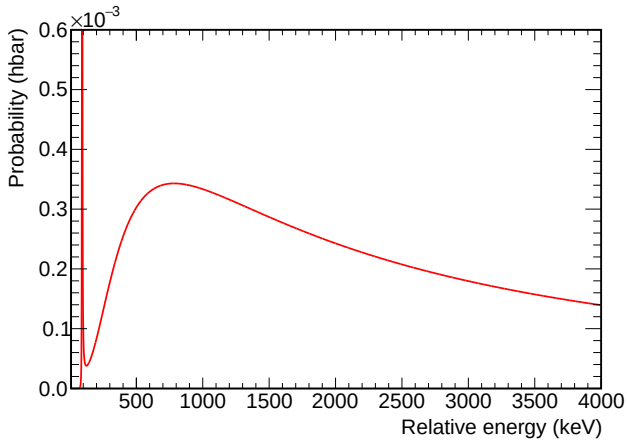

Figure 2.3: Graph of Equation (2.16) as function of relative energy of the $\alpha + \alpha$ pair. The very narrow ground state at 91.84 keV peaks at a value of $410\hbar$.

2.3.1 *Sequential breakup through the ^{8}Be ground state*

It would be interesting to get an idea of how large a fraction of the triple-α breakups of ^{12}C proceed through the ghost of the ^{8}Be ground state, relative to the total number of decays through $^8\mathrm{Be}(0^+)$. To make such an estimate we use the phase space distributions from Equation (3.7), depicted in Figure 3.4(a) and 3.4(e). We divide the phase space into two regions, using the relative energy of the two lowest-energy alphas, E_{23}. Dividing at $E_{23} = 100\,\mathrm{keV}$ results in a region containing the sharp ground state peak and another region containing the ghost. The phase space distributions are numerically integrated over the two regions using the multi-dimensional Monte Carlo integration routines, VEGAS and MISER, from the GSL library, (Galassi et al. 2009). It should be noted that the two routines give consistent results. The resulting branching ratio for decay through the ghost is dependent on both the available energy, $Q_{3\alpha}$, and the spin and parity of the decaying resonance in ^{12}C, see Figure 2.4.

It is worth noting that it is a sizeable fraction of the ^{12}C breakups that proceed through the $^8\mathrm{Be}(0^+)$ ghost. In the $^{12}\mathrm{C}(\gamma, 3\alpha)$ experiment reported on by

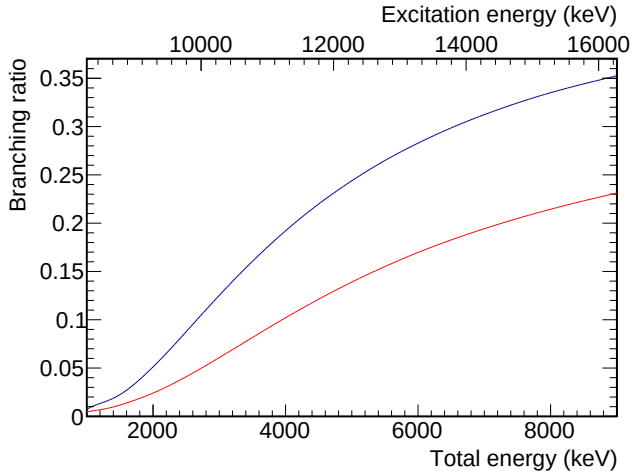

Figure 2.4: Predicted branching ratio for breakup through the ghost of the ^{8}Be ground state as function of excitation energy in ^{12}C. The blue line shows the branching ratio assuming an initial 0^+ resonance and the red line shows the branching ratio assuming an initial 2^+ resonance.

(Zimmerman 2013) excited 2^+ strength in ^{12}C was populated to excitation energies of 9.1 MeV–10.7 MeV. It was estimated that 1 %–6 % of the breakups proceeded through excited states in ^{8}Be, which includes the ^{8}Be(0^+) ghost. If we look at Figure 2.4 we see that the predicted branching ratio varies from 2 % to 8 %, which means that all the observed decays through excited states in ^{8}Be could be explained as going through ^{8}Be(0^+) ghost. The population of the ^{8}Be(0^+) ghost was also investigated experimentally by others, for instance by (Szczurek et al. 1991), however, the population method in that experiment was $^{9}\mathrm{Be}(d,t)^{8}\mathrm{Be}^{*}$ and the results are therefore not directly comparable.

There are better opportunities for comparison to experimental results when considering the Hoyle state. The state decays predominantly through the ^{8}Be ground state peak, but the so-called *direct decay* branch has also attracted a lot of interest, since any substantial direct decay branch would lower the reaction rate of the stellar triple-α process, (Freer et al. 1994; Kirsebom et al. 2012; Itoh et al.

2014). In most of these works the only distinction between the decay types is between ^{8}Be ground state peak and everything else, so decays through ^{8}Be(0^{+}) ghost would be included in the category of direct decays. The most recent upper limit on the direct decay branch is 2×10^{-3} from (Itoh et al. 2014), which is consistent with the theoretical prediction of the ghost contribution to the Hoyle state breakup of $1.0(1) \times 10^{-3}$.

3

METHOD

The experimental techniques that have been used to probe the broad resonances above the triple-α threshold in ^{12}C were presented in Chapter 1. In this chapter it is described how we propose to characterise the excited ^{12}C nucleus through β-delayed α decay of ^{12}N.

3.1 BETA DECAY OF ^{12}N

The radiactive isotope, ^{12}N, is unstable towards β decay and decays with a half-life of 11 ms into ^{12}C and an $e^+\nu$-pair (Ajzenberg-Selove 1990). The β decay selection rules impose narrow constraints on the spins and parities of the states in ^{12}C that are populated. The selection rules are dependent on the coupling between the angular momenta of the lepton pair, and can be summarised for allowed decays as

$$\begin{aligned} \vec{S}_{e^+} + \vec{S}_\nu = \vec{0} \quad &\rightarrow \quad \Delta J = 0 \qquad\qquad \text{(Fermi decay)} \\ \vec{S}_{e^+} + \vec{S}_\nu = \vec{1} \quad &\rightarrow \quad \Delta J = -1, 0, 1 \qquad \text{(Gamow-Teller decay)} \end{aligned} \tag{3.1}$$

with no change of parity in either case. Since the ground state of ^{12}N has $J^\pi = 1^+$, the populated states in ^{12}C can only be 0^+, 1^+ or 2^+ states. The Q value of decay between the ground states is

$$Q_{\beta^+} = \left(M_{^{12}\mathrm{N}} - M_{^{12}\mathrm{C}} - 2m_e\right)c^2 = 16.316\,\mathrm{MeV}. \tag{3.2}$$

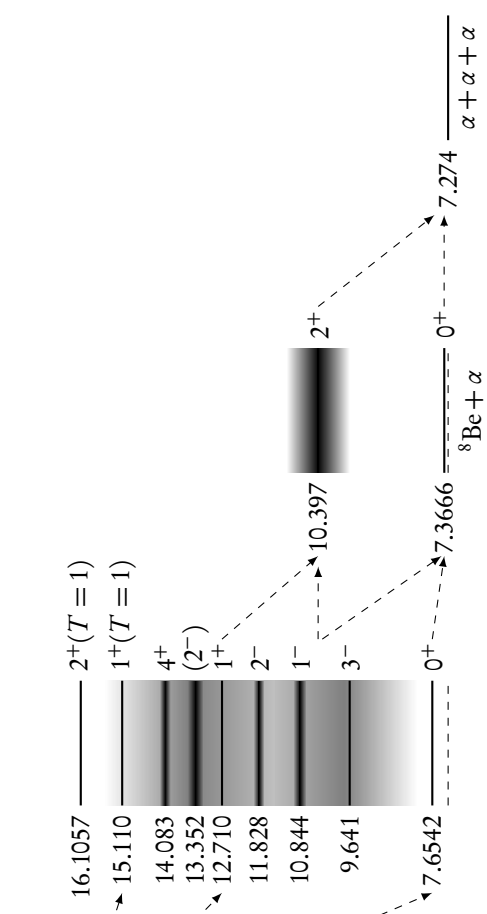

Figure 3.1: An overview of the levels involved in the β-delayed particle breakup of ^{12}N. The number to the left of each level is the energy measured in MeV relative to the ^{12}C ground state. Each level is also marked with its spin and parity, J^π. The values are those found in (Ajzenberg-Selove 1990) and (Tilley et al. 2004).

This means that only states below 16.316 MeV excitation energy in ^{12}C are populated in the decay. Looking at the level diagram in Figure 3.1 we realise that energy conservation allows nine, narrow ($\Gamma < 0.5$ MeV) resonances above the triple-α threshold to be populated in this β decay. The β decay selection rules narrow this down to only three, narrow resonances, in addition to the broad, resonant structures, which are expected to be 0^+ and/or 2^+. Of these it is really only the 1^+ resonance at 12.7 MeV that is close to the energy region of interest and could provide a significant background to the signal from the broad resonances.

3.1.1 The triple-α breakup

The excitation energy in ^{12}C corresponding to the triple-α threshold is

$$E_{3\alpha} = \left(3M_\alpha - M_{^{12}\mathrm{C}}\right)c^2 = 7.274\,\mathrm{MeV}. \tag{3.3}$$

When the daughter state of the β decay is at an energy above this threshold, the ^{12}C* system has (at least) two open decay channels: It can decay through γ emission or through α emission. If we focus on the α channel, we can write the process as $^{12}\mathrm{C}^* \rightarrow ^8\mathrm{Be}^* + \alpha$, where the ^{8}Be nucleus is either in its ground state or first excited state. Since ^{8}Be is unbound, it immediately breaks up into two alpha particles.

$$^{12}\mathrm{C}^* \rightarrow ^8\mathrm{Be}^* + \alpha \rightarrow \alpha + \alpha + \alpha \tag{3.4}$$

Effectively, what we observe is therefore a β-delayed α breakup of ^{12}N with three α particles in the final state.

3.2 Characterisation of the states in ^{12}C

The idea is now to extract information about the excited states of ^{12}C from the kinematics of the three emitted α particles. In the following we shall see how kinematic information from the detection of the α particles can be represented in the Dalitz plot and compared to theoretical predictions.

3.2.1 The Dalitz plot

The Dalitz plot is a way to represent the final state of a system breaking into three fragments. It was originally introduced by Dalitz as a technique to study the decay of K mesons (Dalitz 1953). The basic definitions are shown in Figure 3.2, where E_1, E_2 and E_3 are the kinetic energies of the three α particles

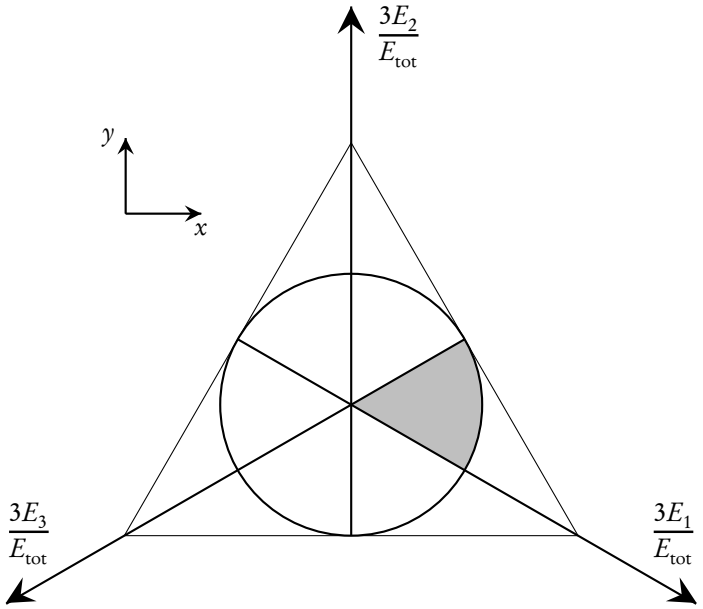

Figure 3.2: Definition of the Dalitz coordinates. The kinematics of a three-particle decay are characterised completely by a point in the Dalitz plot.

α_1, α_2 and α_3 and $E_{\text{tot}} = E_1 + E_2 + E_3$. Since only two coordinates are needed to completely describe a three-body decay, we also introduced the coordinates (x, y), which shall often be referred to as "Dalitz coordinates". If we put the origin at the point where the three energy axes intersect, the Dalitz coordinates

can be calculated as

$$x = \frac{\sqrt{3}(E_1 - E_3)}{E_{\text{tot}}} \quad \text{and} \quad y = \frac{2E_2 - E_1 - E_3}{E_{\text{tot}}} \tag{3.5}$$

The Dalitz plot has some useful properties: Energy conservation only allows decays which are inside the equilateral triangle of the figure and momentum conservation, combined with the fact that we have three identical particles in the final state, further reduces the allowed phase space to within a circle of radius 1, which is also shown. Since the α particles are identical, numbering the decay fragments introduces a six-fold symmetry. If we choose to number the fragments in order of descending energy, i.e. $E_1 > E_2 > E_3$, all allowed decays are contained within the grey slice of Figure 3.2. The last property of the Dalitz plot to mention is that if we observe a pure phase-space breakup, the events would be uniformly distributed in the Dalitz plot. Any non-trivial physics shows up as peaks or minima in the distribution.

3.2.2 *The sequential decay model*

As mentioned in Section 3.1.1 the breakup of ^{12}C into three α particles can be considered as a sequential process, where an α particle and a ^{8}Be nucleus are produced in the first step and the ^{8}Be nucleus breaks into two α particles in a second step. The kinematics of this process is sketched in Figure 3.3. If we denote the energy released in the first step ϵ_1 and the energy released in the second step ϵ_2, we can calculate the kinetic energies of the α particles in the ^{12}C rest frame (in our case also the laboratory system) as

$$\begin{aligned} E_1 &= \frac{2}{3}\epsilon_1 \\ E_2 &= \frac{\epsilon_1}{6} + \frac{\epsilon_2}{2} + \sqrt{\frac{\epsilon_1 \epsilon_2}{3}} \cos\theta_2 \\ E_3 &= \frac{\epsilon_1}{6} + \frac{\epsilon_2}{2} - \sqrt{\frac{\epsilon_1 \epsilon_2}{3}} \cos\theta_2, \end{aligned} \tag{3.6}$$

where θ_2 is the emission angle of α_2 in the rest frame of the recoiling ^{8}Be nucleus.

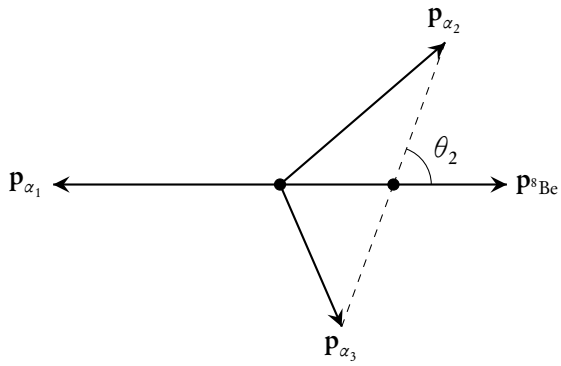

Figure 3.3: The three-body breakup of ^{12}C can be considered as two two-body breakups.

The sequential picture has been combined with an R-matrix treatment in order to analyse the decay of excited states in ^{12}C, for instance in (Balamuth et al. 1974), (Fynbo et al. 2003) and in (Diget et al. 2009). The expression for the breakup amplitude can be written as

$$f_{1-23} = \sum_{m_b} \langle l\, m_a - m_b\, j_b\, m_b | j_a\, m_a \rangle Y_l^{m_a - m_b}(\Theta_1, \Phi_1) Y_{l'}^{m_b}(\theta_2, \phi_2) \times \frac{\sqrt{\Gamma_1 \Gamma_2 / \sqrt{E_1 E_{23}}}\, e^{i(\omega_l - \phi_l)} e^{i(\omega_{l'} - \phi_{l'})}}{E_0 - \gamma_2^2 \left[S_{l'}(E_{23}) - S_{l'}(E_0) \right] - E_{23} - \frac{i}{2}\Gamma_2}. \tag{3.7}$$

A little explanation of the notation is probably in order:

j_a Spin of decaying state in ^{12}C.

j_b Spin of ^{8}Be resonance.

l Orbital angular momentum in the $^{12}\mathrm{C} \rightarrow {}^8\mathrm{Be} + \alpha$ breakup.

l' Orbital angular momentum in the $^8\mathrm{Be} \rightarrow \alpha + \alpha$ breakup.

Γ_1 Partial width of $^{12}\mathrm{C} \rightarrow {}^8\mathrm{Be} + \alpha$ channel.

Γ_2 Partial width of $^8\mathrm{Be} \to \alpha + \alpha$ channel.

E_1 Kinetic energy of α_1 in $^{12}\mathrm{C}$ rest frame.

E_{23} Relative kinetic energy of α_2 and α_3.

E_0 Energy of the intermediate state in $^8\mathrm{Be}$ measured from the two-α threshold.

ω_l Coulomb phase shift.

ϕ_l Hard sphere phase shift.

$S_{l'}$ R-matrix shift function.

Θ_1, Φ_1 Direction of emission of α_1 in the $^{12}\mathrm{C}$ rest frame.

θ_2, ϕ_2 Direction of emission of α_2 in the recoiling $^8\mathrm{Be}$ rest frame.

We note that Equation (3.7) implies a definite order of emission of the α particles. In fact, even in an experiment where all three α particles are detected, there is no way of telling which of them was emitted first. As a consequence, we must symmetrise the amplitude in the order of emission:

$$|f|^2 = \sum_{m_a} |f_{1-23} + f_{2-31} + f_{3-12}|^2, \tag{3.8}$$

where we have also averaged over the possible initial spin projections.

The applicability of Equation (3.7) rests on the assumption that the two breakups proceed completely independently. We can estimate how well this condition is met by considering the spatial separation of α_1 and the $^8\mathrm{Be}$ recoil when the second breakup happens. As an example we take the decay of the 12.7 MeV resonance in $^{12}\mathrm{C}$. The relative velocity of α_1 and the $^8\mathrm{Be}$ recoil is $v = \sqrt{2\epsilon_1/\mu}$, where μ is the reduced mass. Additionally, the lifetime of the intermediate $^8\mathrm{Be}$ resonance is found through the relation $\tau = \hbar/\Gamma_{\mathrm{obs}}$ and, using the values for Γ_{obs} from Table 3.1, we obtain

$$\begin{aligned} (v\tau)_{0^+} &\sim 2.1\,\mathrm{nm} \\ (v\tau)_{2^+} &\sim 5.1\,\mathrm{fm} \end{aligned} \tag{3.9}$$

Table 3.1: R-matrix parameters for the relevant levels in ^{8}Be. E and $\Gamma_{\rm obs}$ of the 0^+ level are taken from (Tilley et al. 2004) while E and γ^2 of the 2^+ level are taken from (Bhattacharya et al. 2006). The other figures were calculated using standard R-matrix formulas and a channel radius of 4.5 fm.

J^π	E (keV)	$\Gamma_{\rm obs}$ (keV)	$\gamma^2_{\rm obs}$ (keV)	γ^2 (keV)
0^+	91.84(4)	$5.57(25)\times10^{-3}$	474(22)	830(38)
2^+	3129(6)	1477(13)	811(7)	1075(9)

for decay through the 0^+ ground state and 2^+ first excited state in ^{8}Be, respectively. Incidentally, the 12.7 MeV resonance has $J^\pi = 1^+$, and conservation of angular momentum and parity only allows decay through the first excited 2^+ level in ^{8}Be. If we assume that right after the first breakup the separation of α_1 and the ^{8}Be recoil is equal to the channel radius of the $^{12}\mathrm{C}\rightarrow{}^8\mathrm{Be}+\alpha$ decay (typically values around 5 fm are used), then the separation is approximately 10 fm when the second breakup happens. At this distance the electrostatic energy of the $^8\mathrm{Be}+\alpha$ system is still 1.1 MeV, and thus comparable to the kinetic energies of the α particles.

From the foregoing discussion it would seem questionable whether we are allowed to regard the sequential breakup of ^{12}C as proceeding in two independent steps. We can, however, make an *ad hoc* modification of Equation (3.7) to correct for the sizeable Coulomb interaction between the three α particles in the final state. In the tunneling picture, imagine that α_1 is formed on the nuclear surface at R and tunnels out to a distance $\tilde{R}$ with a penetrability appropriate for the $^8\mathrm{Be}+\alpha$ channel. When α_1 has reached $\tilde{R}$, the ^{8}Be resonance breaks up and the penetrability must be replaced with the penetrability for two $\alpha+\alpha$ pairs formed at $\tilde{R}$, i.e.

$$\frac{P_l(\epsilon_1)}{\sqrt{\epsilon_1}} \quad\rightarrow\quad \frac{P_l(\epsilon_1)}{\tilde{P}_l(\epsilon_1)}\,\frac{\tilde{P}_{12,\tilde{l}}(E_{12})}{\sqrt{E_{12}}}\,\frac{\tilde{P}_{13,\tilde{l}}(E_{13})}{\sqrt{E_{13}}}. \tag{3.10}$$

Here, P_l is the penetrability for the $^8\mathrm{Be}+\alpha$ pair, calculated using a channel radius of R. $\tilde{P}_l$ is also the penetrability for a $^8\mathrm{Be}+\alpha$ pair, but calculated using a

channel radius of $\tilde{R}$. E_{12} and E_{13} are the relative energies of the pairs $\alpha_1\alpha_2$ and $\alpha_1\alpha_3$, respectively, and $\tilde{P}_{12,\tilde{l}}$ and $\tilde{P}_{13,\tilde{l}}$ are penetrabilities for $\alpha+\alpha$ pairs with a channel radius of $\tilde{R}$ and an orbital angular momentum, $\tilde{l}$, which we assume is equal to the spin of the ^{8}Be resonance. All penetrabilities entering in Equation (3.10) are divided by the square root of the energy, in order to remove the phase space factor (i.e. the factor ρ in the definition of Equation (2.11)).

Penetrabilities are included in Equation (3.7) via the partial widths, which are calculated from the reduced widths as $\Gamma = 2P_l\gamma^2$. By replacing the penetrability in Γ_1 with the modified penetrability we correct for Coulomb interaction in the final state. With this *Coulomb correction* Equation (3.7) has been shown to fit experimental data from the breakup of the 12.7 MeV resonance quite well, if $\tilde{R}$ is chosen in the vicinity of 10 fm (Fynbo et al. 2003).

In essence, we can now predict the phase space distribution of the three α particles emitted in the decay of ^{12}C resonances. The distribution depends, among other things, on the spin of the initial resonance, j_a, which means that it is possible to infer j_a from comparison of experimental phase space distributions to the prediction of Equation (3.7).

3.3 Allowed modes of decay

As discussed in Section 3.1 we know that only 0^+, 1^+ or 2^+ resonances in ^{12}C are populated in the β decay of ^{12}N. Looking at Figure 3.1 we conclude that there are only two states in ^{8}Be in the energy region we are interested in which can act as intermediate resonances in the triple-α breakup, namely the 0^+ ground state and the 2^+ first excited state. Conservation of parity and total angular

Table 3.2: Possible combinations of j_a, l and j_b that conserves parity and total angular momentum in the triple-α breakup of ^{12}C.

j_a	0	0	1	2	2	2	2
l	0	2	2	0	2	2	4
j_b	0	2	2	2	0	2	2

momentum constricts the number of ways we can combine j_a, l (the orbital

angular momentum of $^8\mathrm{Be} + \alpha_1$) and j_b (spin of intermediate resonance in ^{8}Be) to seven. These allowed combinations are listed in Table 3.2.

In Figure 3.4 the phase space distributions for each model are shown in the Dalitz plot representation, described in Section 3.2.1, for several values of E_{tot}. A very clear feature can be observed in Figures 3.4(a) and 3.4(e) which show the (0,0,0) and (2,2,0) decay modes. These decays proceed through the very narrow ^{8}Be ground state, which leads to the sharp intensity peak that runs diagonally through the Dalitz plots (note that the peak intensity is far outside the range of the color scale). What is also remarkable about these models is that there is some intensity outside the peak, mainly to the left of the peak, corresponding to a larger relative energy between the two α particles in the ^{8}Be resonance, i.e. $E_{23} > E_{\mathrm{gs}}$. We interprete this as breakups that would populate the ghost of the ^{8}Be ground state, as discussed in Section 2.3.

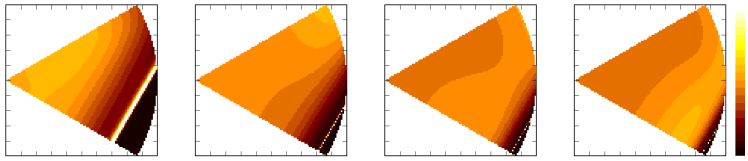

(a) (0,0,0)

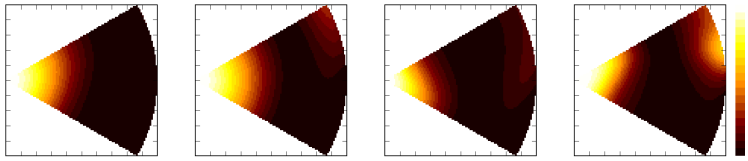

(b) (0,2,2)

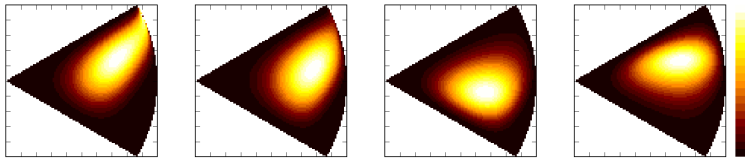

(c) (1,2,2)

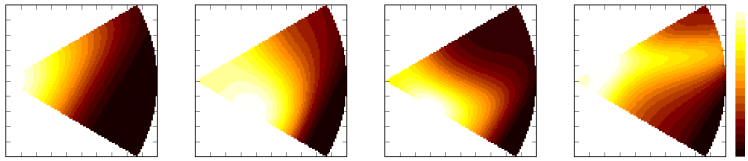

(d) (2,0,2)

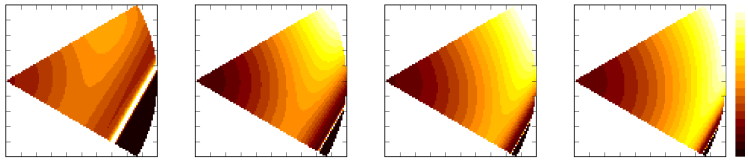

(e) (2,2,0)

Figure 3.4: See description on the next page.

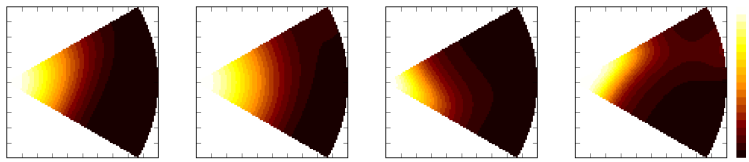

(f) (2,2,2)

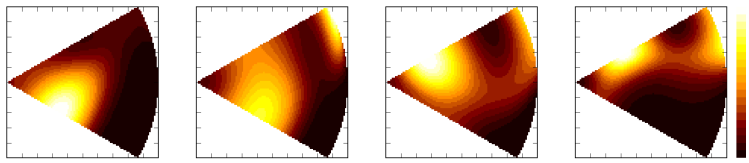

(g) (2,4,2)

Figure 3.4: Dalitz plots of the calculated phase space distributions for the seven possible decay modes. Each mode is labelled by its (j_a, l, j_b) and the distributions are shown for four values of E_{tot} $(= Q_\alpha)$, 1 MeV, 3 MeV, 5 MeV and 7 MeV. The plots are arranged with E_{tot} ascending from the left. The color scale is linear in density.

4

EXPERIMENT

An experiment was devised in order to observe the β-delayed α decay of ^{12}N. Since ^{12}N, with a half-life of only 11 ms, is quite short-lived (Ajzenberg-Selove 1990), the detection system could not be far removed from the production site. Therefore, the radioactive beam facility, IGISOL, located at the physics department of the *University of Jyväskylä* in Finland, was chosen for our experiment. Here, ^{12}N ions were produced in a transfer reaction, purified and rapidly transported to our detection chamber. In the detection chamber, the ions were stopped in a thin carbon foil surrounded by energy- and position-sensitive particle detectors. If the α particles emitted by the decaying ions had sufficient, kinetic energy, they would escape the carbon foil and hit the detectors. As described in Section 3, we needed to detect all three α particles from a decay in order to investigate the phase space distribution. To ensure a good triple-α coincidence detection efficiency, the solid-angle coverage of the detectors was chosen rather large ($\sim 45\,\%$ of 4π).

4.1 IGISOL IN JYVÄSKYLÄ

The IGISOL facility in Jyväskylä has recently undergone an upgrade, and is now running in its fourth incarnation (Äystö 2001; Moore et al. 2013). IGISOL is an acronym for *Ion-Guide Isotope Separation On-Line* and it is a technique for producing low-energy beams of short-lived radioactive ions.

A primary ion beam is produced by a cyclotron and led to the ion source and the main target, which is sketched in Figure 4.1. When the primary beam

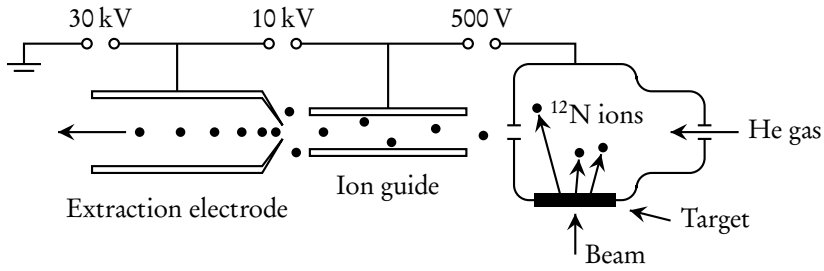

Figure 4.1: The principle behind IGISOL. The sketch is based on (Äystö 2001). Details of the figure are discussed in the text.

hits the target, a cocktail of different isotopes is produced, and some of the reaction products recoil out of the target and into a stream of helium gas that sweeps them into the ion guide. The RF sextupole ion guide acts as a mass filter and only allows the selected ions to pass through to the extraction electrode. The extracted ions are then electrostatically accelerated and led to the relevant experimental setup. The voltages in the figure are subject to changes and only quoted to give an idea of their magnitudes.

In case of the present experiment the primary beam consisted of protons at $\sim 30\,\mathrm{MeV}$ kinetic energy, and a target of natural carbon were used. The reaction products included ^{12}N, produced via the $^{12}\mathrm{C}(p,n)^{12}\mathrm{N}$ reaction. The total acceleration voltage for the radioactive beam was 29.9(1) kV.

The laboratory in Jyväskylä has two cyclotrons, an older *K130* cyclotron, which can accelerate both light and heavy beams, and a new *MCC30/15* cyclotron that accelerates proton and deuterium beams. The installation of the second cyclotron made it possible to allow experiments requiring long beam time, since several users can now do experiments in parallel.

4.2 Detection setup

A photograph of the detection setup is shown in Figure 4.2. It consists of a thin foil of natural carbon mounted in the center of a more or less cubic array of

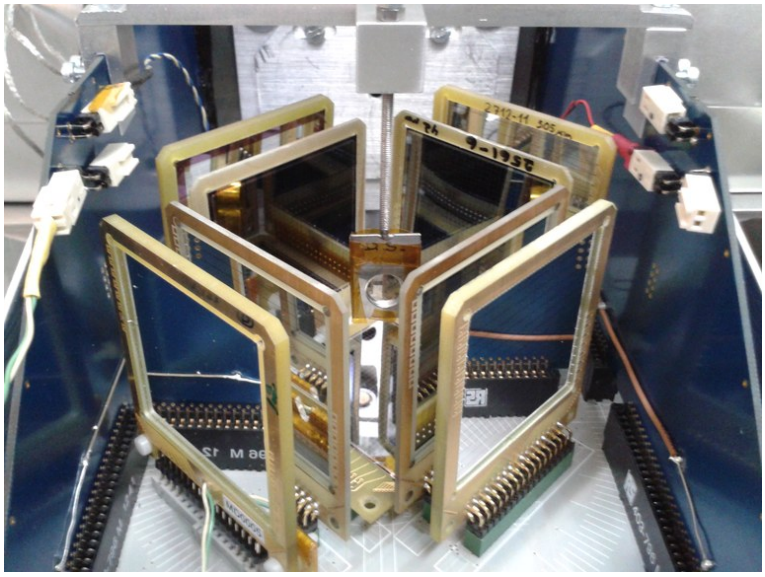

Figure 4.2: The detector setup. Details are found in the text.

particle detectors. The five inner detectors are for detection of α particles while the four outer detectors are meant to detect β particles. The ^{12}N beam emerges from the small hole, barely visible in the background behind the foil holder. The entire setup is operated under vacuum, with a HPGe detector placed outside the vacuum chamber to detect γ rays, useful for absolute normalisation.

4.2.1 The foil

The first component that the ^{12}N ions meet after entering the detection chamber is a thin carbon foil that puts the ions to rest. We can estimate how far a ^{12}N ion with a kinetic energy of 29.9 keV penetrates into the foil with the TRIM simulation package (J. Ziegler et al. 2010). The result of a simulation with 10^5 ions is shown in Figure 4.3. The foil should be sufficiently thin that it allows even low energy α particles from the decay to escape, but at the same time it

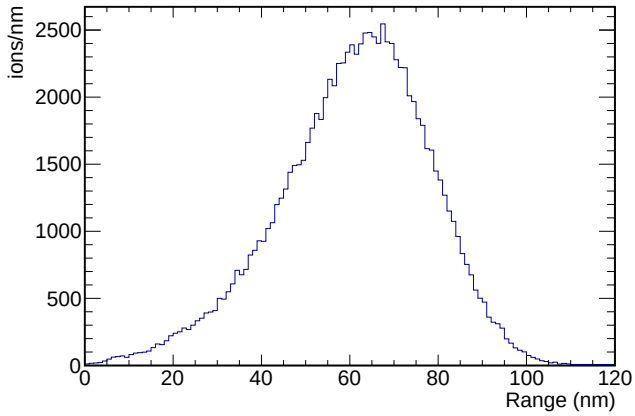

Figure 4.3: A simulation of 29.9 keV ^{12}N ions penetrating into a natural carbon target. The histogram shows the implantation depth of the ions.

should be thick enough to stop the majority of impending ^{12}N ions. A foil thickness of around 110 nm seems to be an appropriate choice.

4.2.2 The detectors

Six of the detectors in the setup are *Double-Sided Silicon Strip Detectors* (DSSSD), supplemented with three silicon pad detectors. The DSSSDs are of the W1 type from *Micron Semiconductor Ltd*. This detector type has an active area of 50 mm × 50 mm, it has sixteen contact strips on the front side and sixteen more running orthogonally on the back side, giving a total of 256 pixels. The strips are 3 mm wide and separated by a 0.1 mm inter-strip region. The detector design is modified from the traditional W1 design in order to achieve a very thin dead layer of only 100 nm Si-equivalent, as described in (Tengblad et al. 2004). A segment of a DSSSD is sketched in Figure 4.4. We use the LISE++ physics toolbox to calculate the typical energy loss of α particles in silicon (Tarasov and Bazin 2008). A 1 MeV α particle would lose on average 32 keV travelling through a 100 nm dead layer, while it would lose more than 200 keV travelling through

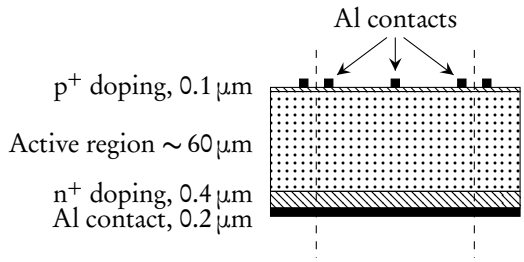

Figure 4.4: The structure of a DSSSD of the thin dead layer design. The continuous aluminium contact strips on the front (top in this figure) has been replaced by an aluminium grid. The result is an effective dead layer thickness of only 100 nm over most (~ 98 %) of the detector surface. The dashed lines indicate borders between two strips.

the 630 nm dead layer of the ordinary W1 design. Thus, for spectroscopy of low energy α particles, the thin dead layer provides significant advantage with regard to accuracy and low-energy detection thresholds. The pad detectors are of the same physical dimensions as the DSSSDs, but are unsegmented.

The detectors are arranged in an almost cubic array, which is sketched in Figure 4.5. The labels of the detectors, which we shall later use for reference, are also provided in the figure. The basic properties of the detectors are summarised in Table 4.1. The inner detectors are, except for U4, chosen to be quite thin, in order to minimise their response to β particles. U3 and U4 are both sufficiently thick to have a good β response, which can be useful for analysing $\beta\alpha$ angular correlations. These correlations provide an alternative way of learning about the ^{12}C resonances populated in β decay of ^{12}N. For the analysis of phase space distributions of the three α particles from the decay we are only concerned about the five inner detectors, since the alphas are of such low kinetic energy that they are completely stopped in these.

4.3 Goal and achievement

A very similar experiment (I301) was carried out a decade ago and reported in (Diget et al. 2009). The data were also then analysed with the Dalitz plot tech-

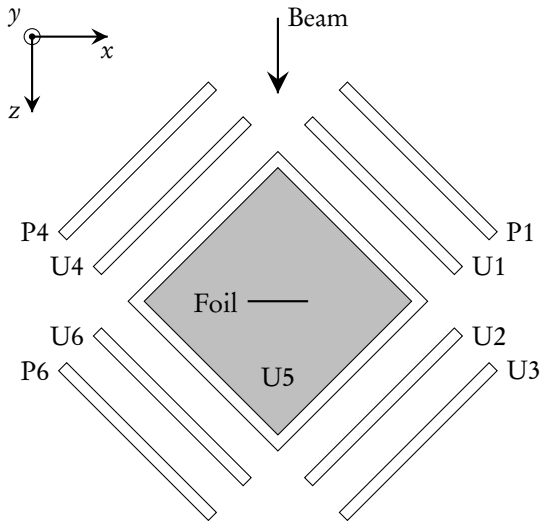

Figure 4.5: A map of the experimental setup as seen from above. The detectors are labelled and coordinate axes are defined.

Table 4.1: An overview of the detectors.

Detector	*Thickness* (μm)	*Type*
U1	42	DSSSD
U2	67	DSSSD
U3	1041	DSSSD
U4	524	DSSSD
U5	69	DSSSD
U6	65	DSSSD
P1	505	Pad
P4	1473	Pad
P6	1483	Pad

nique, and the conclusion was that all the strength below 10.5 MeV excitation energy in ^{12}C could be explained as a 0^+ resonance decaying via the $(0,0,0)$ mode (see Section 3.3). Furthermore, the strength above 12.7 MeV was shown to be consistent with a 2^+-resonance decaying through the $(2,2,2)$-mode.

The present experiment (I161) was at the time of proposal planned to improve on the counting statistics from the old experiment by a factor of 250. Fourteen days of ^{12}N beam and six days of ^{12}B beam (the mirror nucleus of ^{12}N which also β decays to ^{12}C) were asked for and granted.

On the 10th of June 2014 the first ^{12}N beam was delivered by IGISOL to our setup. After ~ 3 h the MCC30/15 cyclotron broke down. It was not possible to get support from the Russian manufacturer because of a national holiday in Russia, and in spite of intense efforts by the IGISOL group to repair the cyclotron it did not become functional again during the experiment. From the 18th until the 26th of June a ^{12}N beam was again delivered by IGISOL, using the K130 cyclotron for primary beam. In the end we detected approximately a factor of thirty-five more triple-α coincidences from ^{12}N than the earlier experiment, reaching 2×10^4 coincidences pr. 100 keV in the 9 to 10 MeV excitation energy region.

5

CALIBRATION

Calibration is about learning as many details as possible with regard to the experimental setup. The motivation for doing a careful calibration is two-fold: First, it is needed in order to get meaningful information out of the collected data, and second, a detailed understanding is necessary if you want to reliably simulate the behaviour of the setup.

5.1 ENERGY

An energy calibration is needed such that the stored ADC values can be converted to equivalent particle energies. Therefore, a source of α-radioactive nuclides were placed in front of each of the inner DSSSDs both before and after the experiment. The source contained ^{239}Pu, ^{241}Am and ^{244}Cm, the properties of which are listed in Table 5.1. The energy calibration is done for each strip of the detectors, and a typical single-strip spectrum is shown in Figure 5.1. The calibration is an iterative process in which a preliminary calibration is done with some reasonable, guessed values for the detector dead layer thickness and source thickness. These thicknesses are then found from analysis of the calibrated data and finally the data are re-calibrated using the proper thicknesses.

5.1.1 Peak position

The task is to determine the position of the peaks in the spectrum and relate them to the corresponding α particle energy. Therefore we are immediately

Table 5.1: Dominating α lines from the isotopes in the calibration source. The values are those recommended by (Rytz 1991).

Isotope	I_α (%)	E_α (keV)
^{239}Pu	73.3(8)	5156.59(14)
	15.1(8)	5144.3(8)
	11.5(8)	5105.8(8)
^{241}Am	85.1(3)	5485.56(12)
	13.3(7)	5442.80(13)
^{244}Cm	76.4(12)	5804.77(5)
	23.6(12)	5762.16(3)

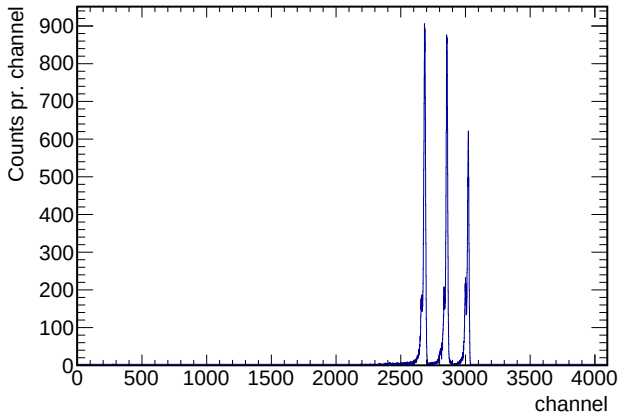

Figure 5.1: Calibration spectrum from a front strip of detector U2.

forced to define what we mean by *peak position*. If the peaks in Figure 5.1 had been Gaussians, or even just symmetric, the definition of peak position would have been trival; the centroid of the Gaussian, the mean value or the median value would all yield the same result. Figure 5.2 shows a zoom of the spectrum

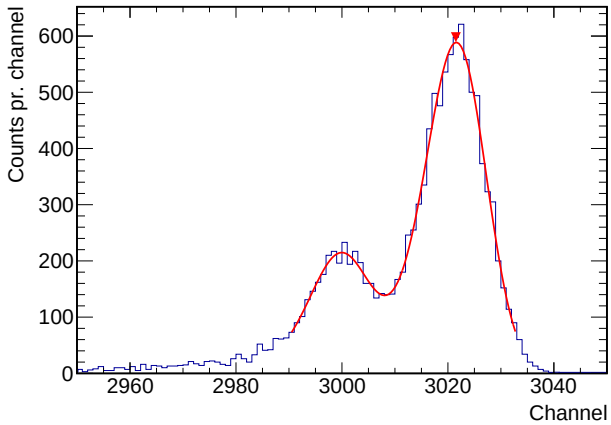

Figure 5.2: Zoom of the spectrum in Figure 5.1. We see the primary and secondary peak from ^{244}Cm together with a fit to the line shape described in the text.

in Figure 5.1 and we see that the two peaks are in fact asymmetrical.

The asymmetric response of silicon detectors is a well known phenomenon, and it has been shown, for instance by (Bortels and Collaers 1987), that the line shape is well approximated by a Gaussian function folded with a left-handed exponential tail. In fact, more than one exponential tail is needed if the α peaks are fitted over a large energy range, but to keep the calibration algorithm simple and robust we restrict ourselves to a narrow region around the peaks and include only one tail. The fitting function then takes the form

$$f(E) = \frac{A}{2\tau} \exp\left(\frac{E-\mu}{\tau} + \frac{\sigma^2}{2\tau^2}\right) \operatorname{erfc}\left[\frac{1}{\sqrt{2}}\left(\frac{E-\mu}{\sigma} + \frac{\sigma}{\tau}\right)\right]. \tag{5.1}$$

Here, A is the peak area, μ is the formal peak position, τ is the tail parameter

and σ is the width of the Gaussian component. A fit of this function to data is shown in Figure 5.2. Since the α lines of the source appear in dublets, it is actually a two-component fit, but τ and σ are the same for the two lines. In this work the peak position is defined as the formal position, μ, extracted from these fits.

5.1.2 Dead layers and source thickness

Now that we have defined the observed peak position we must figure out what energy to assign to the peak. The source emits practically monoenergetic α particles, but on its way from the emission point in the source to the active region of the detector the particle loses a fraction of its energy. The situation is sketched in Figure 5.3. The thick lines on the figure are the layers of either

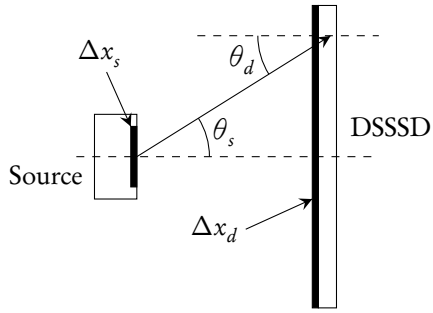

Figure 5.3: The setup for a calibration run. The source is mounted 30 to 40 mm from the DSSSD. The thick lines illustrates that the source material has an effective thickness, Δx_s, and that the detector has a dead layer of effective thickness Δx_d.

source material or detector dead layer that the α particles travel through before reaching the active region of the DSSSD.

The energy loss consists of two parts: Some energy is lost in the source, ΔE_s, and some is lost in the dead layer, ΔE_d. Since the energy losses are small compared to the kinetic energy of the calibration alphas, we are allowed to ap-

proximate

$$\Delta E \approx \left(\frac{dE}{dx}\right)_E \Delta x. \tag{5.2}$$

From the geometry in Figure 5.3 it is clear that $\theta_s = \theta_d$, and further that $\Delta x = \Delta x_0 / \cos\theta_d$, where $\Delta x_0 = \Delta x_s + \Delta x_d$ is the total thickness of the non-active material. Therefore we can write

$$\Delta E(\theta_d) = \frac{\Delta E_0}{\cos\theta_d} \quad ; \text{where} \quad \Delta E_0 = \left(\frac{dE}{dx}\right)_E \Delta x_0. \tag{5.3}$$

A linear fit of the observed α energy vs. $1/\cos\theta_d$ should directly provide us with ΔE_0. Such a fit is done for all the inner DSSSDs except for U5, since the source was mounted too far away from the detector to provide a strong energy variation across the detector surface. A fit to the position of the ^{239}Pu peak for different angles of incidence on U1 is shown in Figure 5.4. The energy losses

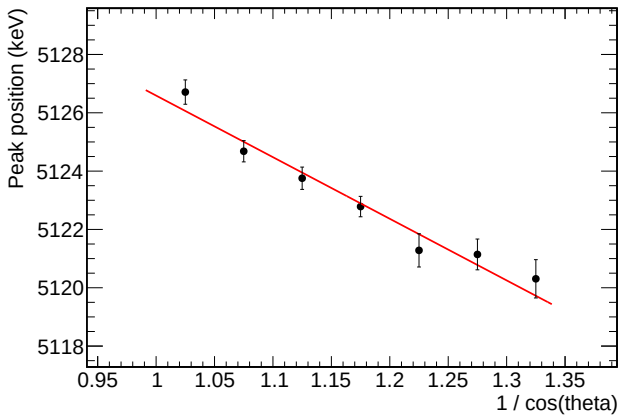

Figure 5.4: The position of the ^{239}Pu peak was found for different ranges of $1/\cos\theta_d$ across U1. The linear fit in this figure corresponds to $\Delta E_0 = 21.1(19)$ keV.

were converted to an equivalent thickness of silicon with LISE++ (Tarasov and

Table 5.2: Total energy loss of the primary alphas from the calibration source. The values are found from fits similar to the one shown in Figure 5.4. The energy losses have also been converted to a thickness of silicon equivalent.

Det	$(\Delta E_0)_{\mathrm{Pu}}$ (keV)	$(\Delta E_0)_{\mathrm{Am}}$ (keV)	$(\Delta E_0)_{\mathrm{Cm}}$ (keV)	Δx_0 (nm)
U1	21.1(19)	20.5(16)	18.9(20)	147(3)
U2	23.1(19)	21.6(17)	23.4(20)	164(12)
U4	20.5(8)	19.8(8)	20.9(15)	146(9)
U6	18.2(7)	15.8(10)	17.8(9)	126(10)

Bazin 2008) and the weighted mean was calculated for each detector. The results are summarised in Table 5.2.

The geometry in Figure 5.3 does not allow disentanglement of Δx_s and Δx_d, however, if we look on one of the detectors not directly faced by the source the situation is different, see Figure 5.5. With this geometry, the energy loss of the

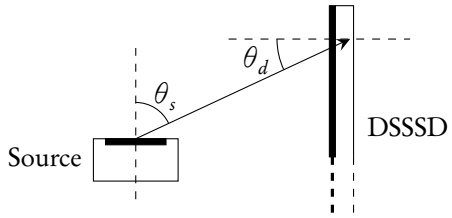

Figure 5.5: Sketch of the geometry used to measure the effective source thickness, Δx_s.

detected α particles is described by

$$\Delta E(\theta_s, \theta_d) = \frac{\Delta E_s}{\cos\theta_s} + \frac{\Delta E_d}{\cos\theta_d} \approx \frac{\Delta E_s}{\cos\theta_s} + \text{const}, \tag{5.4}$$

where we approximate the energy loss in the detector dead layer with a constant, since in our data $1/\cos\theta_d$ only varies from 1 to 1.2, while $1/\cos\theta_s$ varies from 2 to 10. Next, we find the observed α energy for different values of $1/\cos\theta_s$ and do a linear fit, an example of which is seen in Figure 5.6. A weighted average

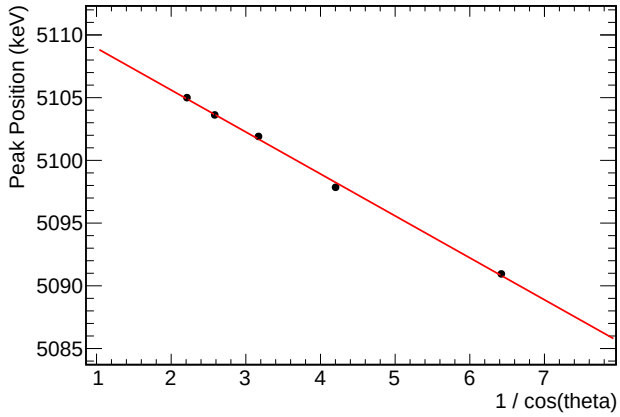

Figure 5.6: The position of the ^{239}Pu peak was found for different ranges of $1/\cos\theta_s$ across U4. The linear fit in this figure corresponds to $\Delta E_0 = 3.3\,\text{keV}$.

of the results from the four detectors is found for each of the three, primary, calibration energies, and the results are listed in Table 5.3. With a value for the effective source thickness of 32(5) nm we can go back to the results in Table 5.2 and find Δx_d for each detector. The values listed in Table 5.4 are in quite good

Table 5.3: The effective energy loss in the source is found for each of the three, primary, α energies.

$(\Delta E_s)_{\text{Pu}}$ (keV)	$(\Delta E_s)_{\text{Am}}$ (keV)	$(\Delta E_s)_{\text{Cm}}$ (keV)	Δx_s (nm)
4.8(20)	4.4(18)	4.2(20)	32(5)

agreement with the factory specification of 100 nm. As mentioned already, there is no data available for measuring the dead layer thickness on U5, but since the measured values for U1, U2, U4 and U6 are close to the factory specification it seems reasonable to assume a value of 100 nm for U5.

Table 5.4: Values for detector dead layer thicknesses found from analysis of the calibration data.

Detector	Δx_d (nm)
U1	115(6)
U2	132(13)
U4	114(11)
U6	94(11)

5.1.3 Weighted energy loss

Now that the dead layers are characterised it is straightforward to calculate the energy loss of an α particle with known, kinetic energy and known angle of incidence. When doing the calibration on a strip-by-strip basis, however, the angle of incidence is not known, since it varies along the strip. To take this into account we calculate a solid-angle weighted average energy loss for the calibration. In a single-strip spectrum we expect to observe an α particle with energy E_0 at

$$E_{\text{obs}} = E_0 - \frac{\sum_{i=1}^{16} \Delta E_i \Omega_i}{\sum_{i=1}^{16} \Omega_i}, \tag{5.5}$$

where the sums are over the sixteen pixels of the strip, ΔE_i is the energy loss calculated for pixel i and Ω_i is the solid angle that pixel i subtends when viewed from the source position. If we denote the angle of incidence θ_i for the ith pixel, we can write $\Delta E_i = \Delta E_0 / \cos\theta_i$ and $\Omega_i = [A/(4\pi d_i^2)] \cos\theta_i$, where d_i is the distance from the source to pixel i and A is the pixel area, and Equation (5.5) becomes

$$E_{\text{obs}} = E_0 - \Delta E_0 \frac{\sum_{i=1}^{16} \cos^2\theta_i}{\sum_{i=1}^{16} \cos^3\theta_i}. \tag{5.6}$$

This is then the energy which is used to calibrate the strip.

5.1.4 *Pulser data*

As is evident from Figure 5.1 the three calibration points provided by the α source calibration are distributed throughout a very narrow energy range compared to the full range of the ADC. Especially, since detection of low-energy alphas is important for the present work, it would be convenient with another calibration point at lower energy. This is achieved by feeding the signal from a spectroscopic pulser to the pre-amplifiers. The spectroscopic pulser can de-

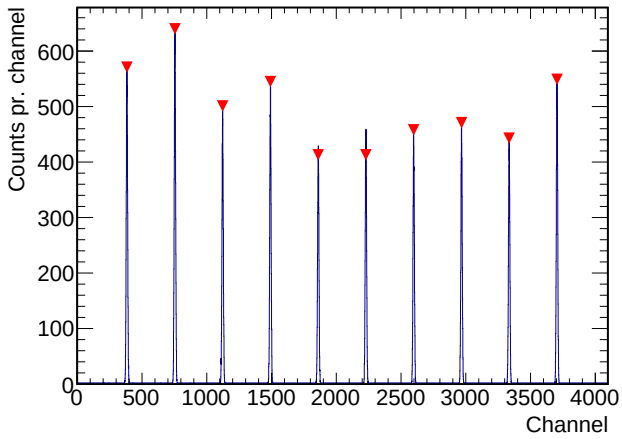

Figure 5.7: Raw ADC spectrum of a spectroscopic pulser.

liver pulses with a very well-defined pulse height, and in particular it can deliver pulses with a height directly proportional to some whole number, m, i.e. $V = mV_0$. The ADC channel number, n, depends linearly on the pulse height, such that $n = AV + B$, where A and B are constants. An example of the raw ADC-spectrum of the pulser signal is shown in Figure 5.7, and these data are used to locate the channel numbers, $n(m)$, corresponding to $m = 1, 2, ...10$. If the relations for pulse height and channel number are combined, we get

$$n(m) = mAV_0 + B, \tag{5.7}$$

and a linear fit of $n(m)$ vs. m immediately gives the coefficients AV_0 and B. The channel corresponding to zero pulse height, the *zero-energy channel*, is $n(0) = B$. If we use a calibration function of the form

$$E(n) = a(n - n(0)), \tag{5.8}$$

then it is really only the slope, a, which is unknown and must be found using the α calibration data.

5.2 GEOMETRY

Since the data analysis relies not only on the energy of the detected α particles but also on knowledge of their momentum, it is necessary to know the positions of the detectors relative to the decay point. Some measurements can be made with a simple ruler, but as is evident from Figure 4.2, there is not much room to fiddle around with measurement devices without the risk of accidentally destroying some fragile and expensive component. The physical measurements are therefore supplemented with solid angle fits to decay data.

One distance, which could be measured reliably with a ruler, was the distance from the detector plane to the target holder. The results are listed as d_{meas} in Table 5.5, and I would estimate the target-detector distances to be accurate within 1.5 mm.

Table 5.5: Distance between beam spot and detector plane, d_{meas}, as measured with a ruler. Also listed are the number of α singles and the projection of the beam spot on the detector plane, found with the method described in the text.

Detector	d_{meas} (mm)	N_α	$\tilde{x}_p$ (mm)	$\tilde{y}_p$ (mm)
U1	35.9(15)	148900	1.48(7)	−1.77(9)
U2	31.1(15)	196900	5.75(3)	0.38(7)
U4	34.4(15)	157400	2.52(8)	0.53(5)
U6	40.6(15)	125700	−3.89(13)	0.48(2)

The transverse position of the detector relative to the beam spot, i.e. the projection of the beam spot onto the detector plane, is found from the α-particle

hit pattern. Analysing the ^{12}N decay data, the number of single α detections is counted in each detector. The conditions used here to identify an α particle is $|E_f - E_b| < 65\,\text{keV}$ and $2000\,\text{keV} < E < 5000\,\text{keV}$. The rather high low-energy threshold is necessary to avoid including β particle hits in U4 and noise in general in the data. The hit pattern of these single α particles is shown for U1 in Figure 5.8. If we assume that the intensity is spherically distributed then the

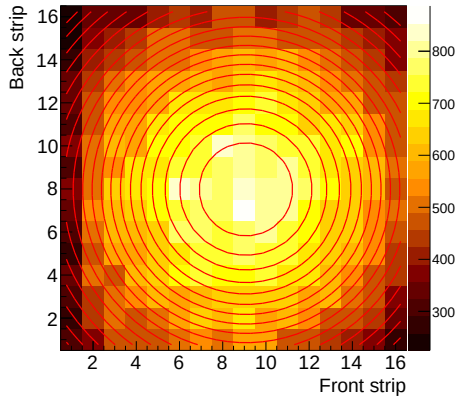

Figure 5.8: Hit pattern of single α particles identified by the conditions described in the text. The pattern is from U1 and shown together with a polynomial fit to the intensity.

hit pattern will show a maximum at the point closest to the beam spot, since the pixels here subtends the largest solid angle. The maximum of the observed hit pattern is found by fitting it to a polynomial intensity distribution,

$$N_i = c_0 + c_1 d_i + c_2 d_i^2 + c_3 d_i^3 + c_4 d_i^4, \tag{5.9}$$

where $d_i = [(\tilde{x}_i - \tilde{x}_p)^2 + (\tilde{y}_i - \tilde{y}_p)^2]^{1/2}$, $(\tilde{x}_i, \tilde{y}_i)$ is the pixel position in the coordinate system defined in Figure 5.9 and $(\tilde{x}_p, \tilde{y}_p)$ is the projection of the beam spot. The hit pattern in Figure 5.8 is overlaid with contour lines of the corresponding fit. The results for U1, U2, U4 and U6 are shown in Table 5.5 together with the uncertainties estimated by the fitting routine (MINUIT, included in the ROOT library (Brun and Rademakers 1997)). It should be noted that I find these errors

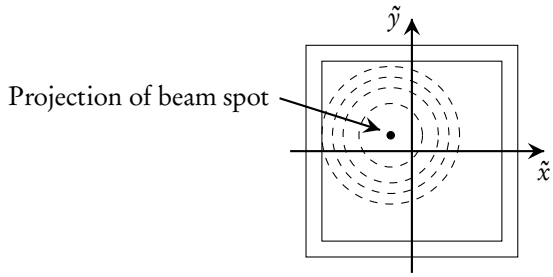

Figure 5.9: Definition of the $(\tilde{x}, \tilde{y})$ coordinates used to characterise the projection of the beam spot on the detector plane. The dashed lines respresent contours of the α particle intensity distribution.

unrealistically small, mainly because they do not take any systematic errors into account. It is not possible to do the same analysis for U5, since it is partly shadowed by the target holder.

With values for d, $\tilde{x}_p$ and $\tilde{y}_p$ it is straightforward to calculate the total solid angle, Ω, subtended by each of the detectors with respect to the beam spot. If the α intensity is indeed spherically symmetric the number N_α/Ω should be equal for all four detectors. Since the statistical error on N_α is very small, we can use it to improve on the determination of the geometry. We construct a χ^2:

$$\chi^2 = \sum_{\text{det}} \left[\left(\frac{d_{\text{det}} - d_{\text{meas,det}}}{\sigma_d} \right)^2 + \left(\frac{N_{\text{det}} - \bar{N}}{\sigma_N} \right)^2 \right]. \tag{5.10}$$

Here $N_{\text{det}} = N_{\alpha,\text{det}}/\Omega_{\text{det}}$ and $\bar{N} = \sum_{\text{det}} N_{\text{det}}/4$. The error on the measured distances were estimated to $\sigma_d = 1.5\,\text{mm}$ and we let $\sigma_N = 1/\sqrt{N}$. The χ^2-function is then minimised by varying d_{det} and the final values are listed in Table 5.6. One should keep in mind that the method described in this section only works if there is no systematic bias on d_{meas} and N_α.

Table 5.6: Coordinates for the detector centers used in the analysis. The values for U1, U2, U4 and U6 were found through a combination of physical measurements and solid angle fits, while the values for U5 relies solely on physical measurements. Since U5 is partly shadowed by the target holder its effective solid angle is somewhat smaller than the quoted value.

Detector	x (mm)	y (mm)	z (mm)	Ω (%)
U1	25.8(8)	1.77(9)	−27.9(8)	10.0(2)
U2	23.7(7)	−0.38(7)	15.6(7)	13.7(3)
U4	−26.8(8)	−0.53(5)	−23.2(8)	10.8(2)
U5	3.7(15)	−36.0(15)	−9.1(15)	9.4(5)
U6	−31.3(9)	−0.48(2)	25.8(9)	8.1(2)

Table 5.7: Data were taken before and after the experiment to measure the thickness of the target foil. A density of 2.253 g cm^{-3} is used for calculation of the thickness.

Runs	ΔE_{Pu} (keV)	ΔE_{Am} (keV)	ΔE_{Cm} (keV)	Δx_f (nm)
66,68	17.3(7)	15.7(6)	16.1(8)	96(4)
294,314	22.6(10)	20.5(10)	20.0(10)	123(3)

5.3 Foil thickness

In the analysis of the decay data an estimate of the energy loss that the α particles experience in the carbon foil is needed. Therefore it is necessary to know the implantation depth and the foil thickness in order to find the amount of traversed material. It is obvious from Figure 4.3 that the implantation depth follow a quite broad distribution, but in the data reduction we use the mean implantation depth of 63 nm.

The foil thickness is found experimentally by shining α particles from the calibration source through the foil and onto U2. After locating the position of each of the three primary α peaks and comparing with similar data taken with the source shining directly onto U2, it is possible to use the difference in peak energy to infer the foil thickness, see Table 5.7. The measurement was carried

out both before and after the experiment, and we note that the foil thickness seems to have grown between the two measurements. It is not clear what causes the foil to grow, but possible explanations include deposition of stable beam components and/or adhesion of rest gas.

5.4 Detector response

It is possible to do most of the data reduction with just an accurate energy calibration. Still, when we proceed to simulate the experiment, it is very useful to have a more detailed knowledge of the detectors' response to being hit by an energetic, charged particle.

5.4.1 Line shape

We already noted in Section 5.1.1 that the line shape of the detectors are not simple Gaussians. Instead the line shape was described by a Gaussian peak folded with a left-handed exponential tail. For the calibration only one tail was used and the fitting range restricted to a narrow region around the observed peak position. For a detailed simulation of the experiment, however, the full line shape needs to be characterised, and we expand the fitting function with a second, exponential tail, following again (Bortels and Collaers 1987):

$$f(E) = \sum_i \frac{A_i}{2}\left\{\left(\frac{1-\eta}{\tau_1}\right)\exp\left(\frac{E-\mu_i}{\tau_1}+\frac{\sigma^2}{2\tau_1^2}\right)\operatorname{erfc}\left[\frac{1}{\sqrt{2}}\left(\frac{E-\mu_i}{\sigma}+\frac{\sigma}{\tau_1}\right)\right]\right.$$
$$\left.+\frac{\eta}{\tau_2}\exp\left(\frac{E-\mu_i}{\tau_2}+\frac{\sigma^2}{2\tau_2^2}\right)\operatorname{erfc}\left[\frac{1}{\sqrt{2}}\left(\frac{E-\mu_i}{\sigma}+\frac{\sigma}{\tau_2}\right)\right]\right\}, \quad (5.11)$$

where the sum is over the number of peaks in the fitting region. That this function provides a decent fit to the detector line shape is evident from Figure 5.10, where a fit to the ^{244}Cm dublet in U1 is shown. From the figure it is also clear that the observed peak position is not coincident with the formal peak position. The line shape parameters for all five detectors are listed in Table 5.8.

A slightly better fit is achieved, if a broad satellite peak at lower energy is included. The origin of this phenomenon is the aluminium grid that covers

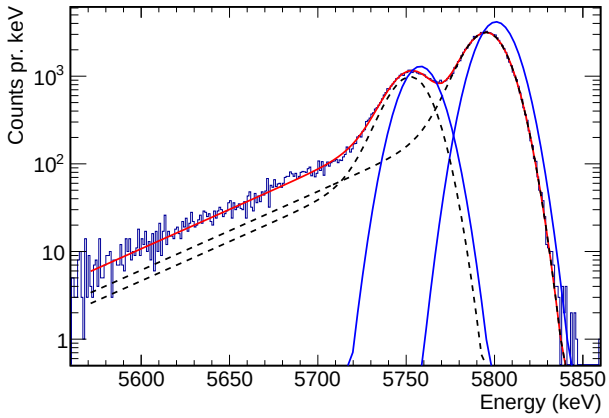

Figure 5.10: The ^{244}Cm dublet as observed in U1. The solid, red line is a fit of Equation (5.11) to the spectrum. The solid, blue curves are the Gaussian peaks for the primary and secondary α components and the dashed, black line shows each Gaussian folded with the exponential tails.

Table 5.8: The line shape parameters extracted from a fit of Equation (5.11) to data from each detector. Only the ^{244}Cm dublet was fitted, since this isotope has the least composite spectrum of the three nuclides in the source.

Detector	σ (keV)	τ_1 (keV)	τ_2 (keV)	η
U1	9.86(8)	6.9(3)	48(1)	0.179(6)
U2	7.46(5)	4.5(2)	39(1)	0.236(5)
U4	5.30(4)	5.1(1)	39(1)	0.221(5)
U5	8.57(6)	3.9(2)	43(1)	0.239(4)
U6	6.88(5)	5.0(2)	39(1)	0.209(6)

around 2 % of the DSSSD surface, see Figure 4.4. A small fraction of the impending particles hits the grid and experiences a larger energy loss than the majority, corresponding to the increased dead layer thickness.

5.4.2 Low-energy thresholds

Some kind of signal is needed to trigger the data acquisition (DAQ) for each event. In practice this happens in the amplifier modules, where a voltage threshold is set for the trigger, and when a signal arrives from the pre-amplifier with a pulse height larger than the threshold voltage the amplifier emits a trigger signal and the DAQ is started. Because of the finite resolution of the detectors, the trigger threshold does not behave as a sharp edge, rather it is characterised by a trigger efficiency, $\epsilon(E)$, that rises smoothly from 0 to 1 as the energy crosses the threshold energy, E_{th}.

To estimate the functional behaviour of the trigger efficiency, let us assume that the deposition of a certain energy in the detector leads to a pulse height with a Gaussian distribution, $p(V|E)$, as sketched in Figure 5.11. The probability of

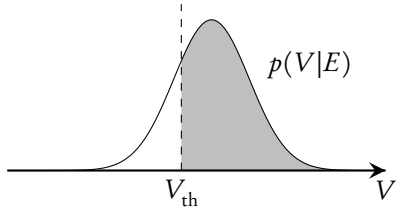

Figure 5.11: A deposited energy, E, leads to a pulse height with some probability distribution, here sketched as a Gaussian.

getting a trigger signal is the integral of the pulse height distribution above the threshold voltage, i.e.

$$\epsilon(E) = \int_{V_{\text{th}}}^{\infty} p(V|E)dV = \frac{1}{2}\left[1 + \text{erf}\left(\frac{E - E_{\text{th}}}{\sqrt{2}\sigma_{\text{th}}}\right)\right], \tag{5.12}$$

where E_{th} is the energy corresponding to the threshold voltage and σ_{th} is a measure of the "width" of the threshold, i.e. how fast $\epsilon(E)$ rises from 0 to 1.

It is possible to observe signals in a channel even below the trigger threshold if the trigger for the event is provided by another channel. Furthermore, if a channel is triggering, the amplifier also fires a timing signal, which is registered by a *Time-to-Digital Converter* (TDC). Thus, if the signals from a channel are gated on a signal in the TDC, the result is a spectrum of only those signals that provided a trigger. This, gated spectrum, divided by the raw spectrum from the same channel, directly provides the trigger efficiency, $\epsilon(E)$. An example, together with a fit of Equation (5.12), is shown in Figure 5.12. The trigger threshold parameters are found in this way for all back strips of the DSSSDs (only the back strips were connected to a TDC).

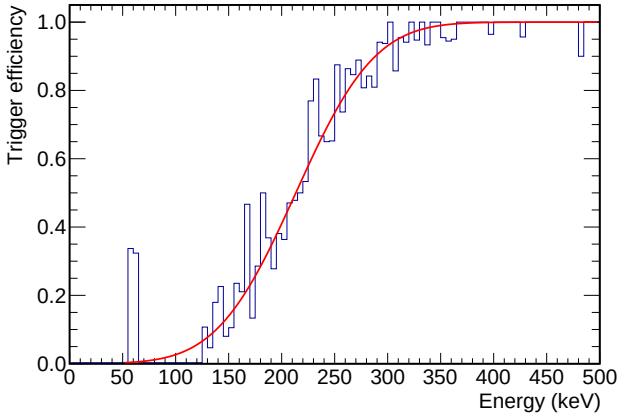

Figure 5.12: Trigger efficiency for back strip number 1 of U1. The fit of Equation (5.12) to the data gives, for this particular strip, $E_{\text{th}} = 213\,\text{keV}$ and $\sigma_{\text{th}} = 58\,\text{keV}$.

In addition to the trigger threshold there is also the threshold of the ADC-module. This is the minimum channel number that the ADC module accepts as a signal, and it is set to a non-zero value in order to avoid filling up data storage with noise signals. The ADC threshold is, in contrast to the trigger threshold, a sharp threshold, and it is immediately visible in the spectra.

6

Data Reduction

The purpose of the present chapter is to describe the reconstruction of the decays from the calibrated detector signals by application of energy corrections and various data cuts. By the end we should have a reasonable overview of the amount and quality of the data.

6.1 Reconstruction of particle hits

The data are collected in an event-by-event fashion. This means that if some signal triggers the DAQ, it reads out all ADC channels and TDC channels and stores those values that are above the ADC thresholds or within the TDC windows. In the preceding chapter we established how to convert the raw ADC values to an equivalent energies, but so far we are only able to tell which front strips and which back strips provided the signals.

6.1.1 Front-back matching

We now need to match the front signals with the back signals in order to figure out in which pixel the detector was hit. The problem is sketched in Figure 6.1. The situation in Figure 6.1(a) is the simplest, and it is straightforward to find the pixel where the DSSSD was hit. The particle energy is found by taking the mean of the front energy and the back energy, $E = \frac{1}{2}(E_f + E_b)$. Figure 6.1(b) shows a DSSSD being hit by two particles, and we see that there are two possible pixel combinations that could produce the same output. In practice, the front-back

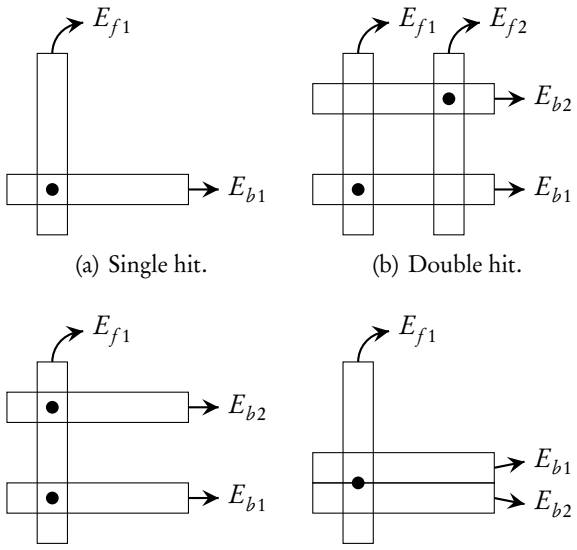

(a) Single hit. (b) Double hit.

(c) Double hit with summing. (d) Single hit with sharing.

Figure 6.1: Four different situations that must be considered when doing front-back matching of DSSSD signals. The black dots show where the DSSSD was hit by a particle.

matching algorithm loops through all strip combinations and selects the combination (i, j) giving the smallest energy difference, $E_{f,i} - E_{b,j}$. The algorithm proceeds until there are no more strips to match up.

In Figure 6.1(c) a rarer type of event is sketched, where the charge signal from two hits are summed in a single strip on one side of the DSSSD. Besides calculating the differences $E_{f,i} - E_{b,j}$, the matching algorithm also calculates $E_{f,i} - (E_{b,j} + E_{b,k})$ and $(E_{f,i} + E_{f,j}) - E_{b,k}$, and if one of these combinations produces a smaller difference than any other, it is concluded that charge summing happened and that actually two particles hit the DSSSD. In the situation of Figure 6.1(c) the front energy is split, such that $E'_{f1} = [E_{b1}/(E_{b1} + E_{b2})]E_{f1}$

and $E'_{f2} = E_{f1} - E'_{f1}$.

The phenomenon of charge sharing, sketched in Figure 6.1(d), has been subject of a surprising amount of research, see for instance (Torresi et al. 2013). It occurs because there is a narrow gap between the strips on a DSSSD, on our detectors it is 0.1 mm, and if a particle hits the DSSSD in an inter-strip region, the generated charge carriers are collected on both neighbouring strips. The probability for charge sharing is on the same order of magnitude as the relative widths of the inter-strip regions and the strips themselves, in our case 0.1 mm compared to 3 mm, or around 3 % for each side. The sharing probability is, however, also dependent on the particle energy and the bias voltage. Interesting as it is, it is not possible to distinguish charge sharing from charge summing, and so we simply reject those strip combinations where neighbouring strips are involved.

6.1.2 Correction for energy losses

With knowledge about how much energy was deposited in which pixel and the geometry calibration from Section 5.2, it is possible to reconstruct the direction of emission of each particle and hence the path it has taken through the target foil and dead layer of the DSSSD. If the traversed deadlayer is denoted Δx_d and the energy deposited in the detector is E_f, then the energy of the α particle before hitting the detector, E_i, can be determined. The SRIM package (J. Ziegler et al. 2010) includes tabulations of ranges of ions in matter for different energies. If we do a cubic spline interpolation of the tabulated ranges, we obtain the range as a continuous function of energy, $R(E)$, and further, since the range is a monotonic function of E, we can also find the inverted range function, $R^{-1}(E)$. The following relation must hold

$$R(E_i) = R(E_f) + \Delta x_d. \tag{6.1}$$

Knowing the inverted range function, it is straightforward to find the initial energy:

$$E_i = R^{-1}(R(E_i)) = R^{-1}(R(E_f) + \Delta x_d). \tag{6.2}$$

Since the implantation depth of the ^{12}N ions in the target foil follows the broad distribution shown in Figure 4.3, it is not possible to exactly determine

how much carbon the α particles have to pass before escaping the foil, Δx_f. The best estimate is to calculate Δx_f from the assumption that the ion was implanted in the average implantation depth, which for the distribution in Figure 4.3 is 63 nm. Furthermore, in Section 5.3 it was concluded that the foil thickness grew from 96 nm to 123 nm during the experiment. An estimate of the actual foil thickness for a given data file is found by linear interpolation between the intial and final thickness. The energy loss in the foil is also calculated with the range inversion method.

6.2 CUTS

In order to distinguish signals from α particles from other signal sources, such as electronic noise and signals from β particles, it is necessary to construct a series of conditions that a signal must fulfill, if it is to be accepted as an α particle candidate. These conditions are often referred to as *cuts*, and they are used to effectively prune the data.

6.2.1 Finding α candidates

For each event, all front and back signals paired by the matching algorithm are compared to a low-energy threshold, which is set slightly above the ADC-threshold for each channel. This is done for two reasons: First, to eliminate electronic noise appearing at the extreme low end of the spectra, and second, to ensure identical sensitivity at low energies for real data and simulated data. These low-energy cuts are set on a channel-by-channel basis and also changes between the data files. This is necessary since the ADC thresholds were adjusted several times during the experiment. Generally the cuts vary between 35 keV and 250 keV.

Another useful piece of information is whether the hit produced a trigger or not. For the experimental data this is easy to check by requiring a TDC signal from the hit. We could try to imitate the behaviour of a trigger in the simulations, however, to make sure that the experimental and the simulated data are treated on an equal footing we instead impose an energy threshold based on E_{th} and σ_{th}, which we found in Section 5.4.2. For each channel we find the

energy, $E_{99\,\%}$, where expression (5.12) gives a trigger efficiency of 99 %. If the energy of a hit is above $E_{99\,\%}$ we define it to have produced a trigger.

A plot of the difference between the energy from the front strip signals and the back strip signals is shown in Figure 6.2. Signals from real α particles should

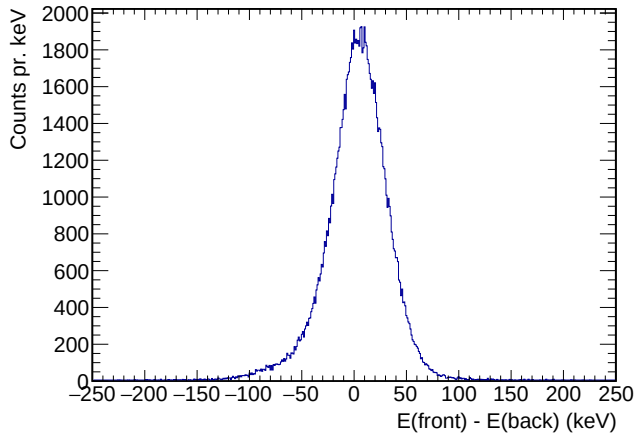

Figure 6.2: Differences between the energy from the front strips and from the back strips of U1. Only a well-behaved subset of the data, i.e. without too much electronic noise, were used in this figure, and it should represent the behaviour of true α signals quite well.

produce a Gaussian distribution around zero, the spread being determined by the electronic resolution of the detection system and the quality of the calibration. The distribution in the figure, however, sits on a broad background, possibly resulting from noise or mismatched signals. Therefore, to remove unphysical signals, we require $|E_{\text{front}} - E_{\text{back}}| < 65\,\text{keV}$. This requirement, even for U1, which is the detector with the poorest resolution, still allows more than 95 % of the real α signals to pass.

Some of the α particles leave the target foil under a very steep angle and thus experience a large energy loss in the foil. Furthermore, even if we do the energy loss calculations very carefully, the uncertainties on the setup geometry

and implantation depth of the ^{12}N in the foil lead to large uncertainties in the energy corrections. To minimise this problem, the pixels closest to the foil plane are excluded from the analysis. Those pixels are excluded where more than half of the α particles are estimated to have experienced an energy loss larger than 50 % of the detected energy.

6.2.2 *Identifying triple-α coincidences*

If an event contains three or more α particle candidates, identified with the methods described in the preceding section, it is possibly a true triple-α coincidence detection. It could, however, also be two α particles together with a β particle, or some of the signals could even be noise.

If there are more than three α candidates in an event, all different combinations are tried, and the combination that minimises the total momentum is selected as the candidates that most probably constitutes the three α particles from the decay. Additionally, at least one of the candidates is required to have caused a trigger. When three candidates have been chosen, their total momentum and energy is calculated and the following conditions are required to be fulfilled:

$$\left|\sum_{i=1}^{3}\vec{p}_i\right| < \frac{1}{2}\sqrt{\sum_{i=1}^{3}E_i + 800\,\mathrm{keV}} \quad \text{and} \quad \sum_{i=1}^{3}E_i > 600\,\mathrm{keV}. \tag{6.3}$$

The results for all possible triple-coincidence events are shown in Figure 6.3 together with the energy-momentum cut. There are many interesting structures in Figure 6.3, and it is not *a priori* clear that this particular cut is effective or even meaningful. Results from simulated data show, however, that most physical triple-α coincidences are indeed expected to fall inside the cut, see Section 7.3.

The cuts are applied in the order in which they have been presented, and the effect of each cut is listed in Table 6.1.

6.2.3 *Decays through the ^{8}Be ground state peak*

From Figure 3.1 we see that the ^{12}C resonances have the possibility to break up both through the narrow ground state peak of ^{8}Be and through the excited

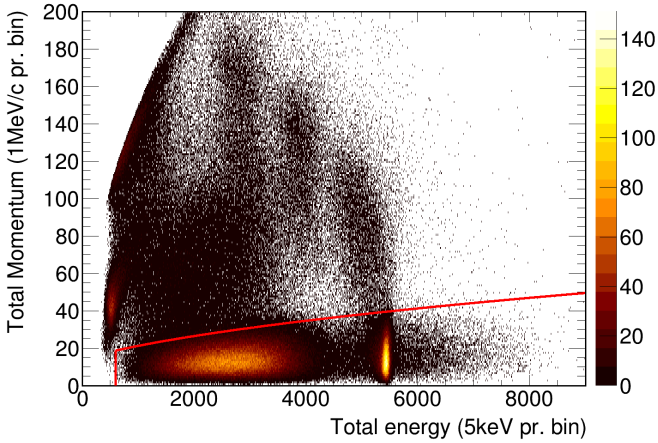

Figure 6.3: If three potential α particles are identified in an event, their total momentum and energy is calculated and the cut shown as a red line in the plot is used to distinguish between true triple-α coincidences and background.

Table 6.1: Application of the cuts described in the text is used to identify true triple-α coincidences. The number of events surviving each cut is listed here.

Cut	*No. of events*
None	363 921 000
Low energy	119 873 000
Energy match	114 516 000
Excl. pixels	99 659 500
At least three hits	1 027 940
At least one trigger	751 949
$\sum E$ and $\lvert\sum \vec{p}\rvert$ cut	518 843
^{8}Be(peak)	418 540
^{8}Be(exc)	100 303

2^+ state of ^{8}Be. Those decays that go through the ground state peak can be considered as two pure phase-space breakups in sequence, and their contribution to the Dalitz plot is trivial. Therefore it is useful to divide the data into ^{8}Be(peak) decays and ^{8}Be(exc) decays.

One way to identify the ^{8}Be(peak) decays is to look at the relative energy of the two α particles with least kinetic energy, labelled α_2 and α_3. Since we already determined the momentum of each α particle, it is possible to find their momentum in the common center of mass, $\vec{p}_{23} = \frac{1}{2}(\vec{p}_2 - \vec{p}_3)$, and use it to calculate the relative energy,

$$E_{23} = 2\frac{\vec{p}_{23}^{\,2}}{2m_\alpha}. \tag{6.4}$$

A spectrum of E_{23} is shown in Figure 6.4. The most significant feature of the

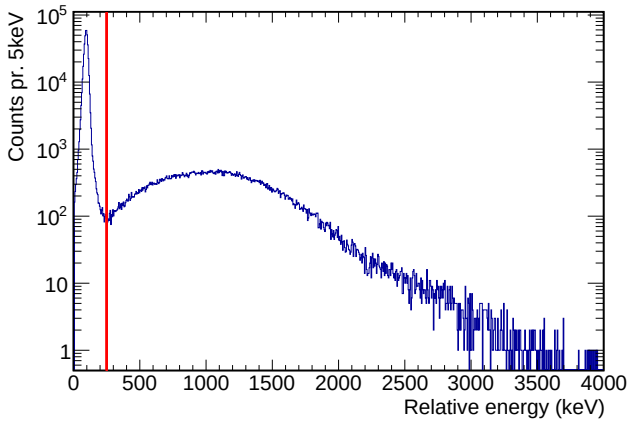

Figure 6.4: A spectrum of the relative energy between α_2 and α_3. The ^{8}Be ground state peak stands out clearly. The red line marks the cut at $E_{23} = 250\,\text{keV}$.

spectrum is the sharp ^{8}Be ground state peak at $E_{23} = 94.0(5)\,\text{keV}$ with a FWHM of 50 keV. At larger values of E_{23} the spectrum rises again, showing that in the sequential picture, the entire energetically accessible region of intermediate ^{8}Be

resonance is populated. Judging from the the figure, the ground state peak starts rising below 250 keV, and so this energy is chosen as the cut between ^{8}Be(peak) and ^{8}Be(exc) decays. The results from applying this cut are shown in Table 6.1.

6.3 SPECTRA

Having endured the tedious details of the preceding sections it is now time to relax and enjoy the view for a bit. For all triple-α coincidences the energies of the α particles are summed and plotted in Figure 6.5. We notice the prominent peak

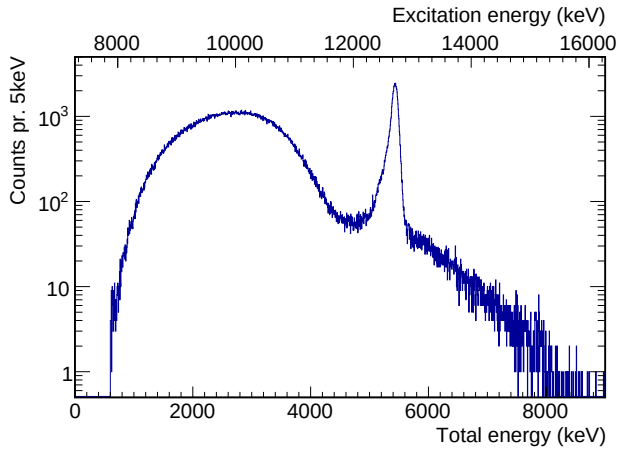

Figure 6.5: A spectrum of the total energy of the three α particles in a triple-α coincidence. Also shown is the corresponding excitation energy in ^{12}C.

at 5435 keV, which is the narrow 1^+ state at 12.7 MeV excitation energy. Since the width of this state is only 18.1(28) eV (Ajzenberg-Selove 1990) its observed line width and shape gives a good impression of the resolution of our detection system. The peak has a FWHM of 110 keV and a pronounced asymmetry. Another remarkable feature of the spectrum is the broad, resonant structures that stretches over the entire accessible energy range, that is, from the triple-α threshold to the top of the β-decay window at 9041 keV above the threshold.

An interesting, alternative way to visualise the data is in a scatter plot, where the total energy is on the horizontal axis and the energy of the individual α particles are along the vertical axis, see Figure 6.6. In this plot there is a lot more

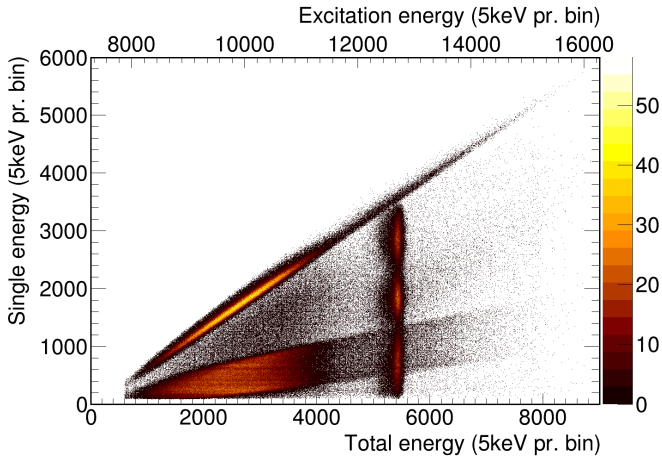

Figure 6.6: A plot of the single α energies vs. their total energy for triple-α coincidence events. Note that each event results in three dots in this type of plot.

structure, and it shows some of the strength of a complete-kinematics experiment. The large amount of intensity along the diagonal originates from decays through the ^{8}Be ground state peak, where, to a very good approximation, the first emitted α particle leaves with two thirds of the available energy, leaving one third for the recoiling ^{8}Be nucleus. When the ^{8}Be recoil breaks up, the kinetic energy is shared between the two emitted alphas, their relative energy being only 91.84 keV from the ^{8}Be ground state. These decays therefore produce one highly energetic α particle (the sharp diagonal line in the plot) emitted almost back-to-back with two alphas, each with much lower energy (the broad band stretching through the lower part of the figure). The 12.7 MeV state obviously decays in a different manner producing three quite distinct "blobs" in the plot. This is caused by the fact that angular momentum and parity conservation forces the 12.7 MeV state to decay through the broad 2^+ first excited state of ^{8}Be.

As described in Section 6.2.3 it is possible to separate out those decays that go through the ground state peak of ^{8}Be. Applying the cut at $E_{23} = 250\,\text{keV}$ and plotting each subset in the same way as in Figure 6.6 results in Figure 6.7. The decays in Figure 6.7(a) only give a trivial contribution to the Dalitz plot, since

$$E_1 = \frac{2}{3}(E_{\text{tot}} - E_{23}) \quad \Leftrightarrow \quad \frac{3E_1}{E_{\text{tot}}} = 2 - \frac{2E_{23}}{E_{\text{tot}}}, \tag{6.5}$$

and with E_{23} fixed at 91.84 keV the decays distribute themselves along a line of constant $3E_1/E_{\text{tot}}$ in the Dalitz plot, see also Figure 3.2 and Figures 3.4(a) and 3.4(e).

A Dalitz plot of the data in Figure 6.7(b) is shown for several ranges of E_{tot} in Figure 6.8. Even though it is tempting to start comparing the plots with the calculated distributions of Figure 3.4 that would really be too soon, since the acceptance of the experiment is not uniform over the three-body phase space and therefore distorts the observed distributions. We note, however, that the 12.7 MeV state is easily identified in the 5000 keV–5600 keV range.

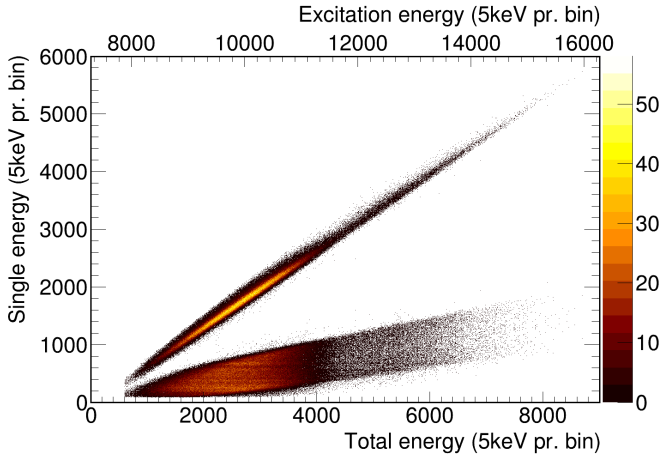

(a) Decays through the ground state peak in ^{8}Be.

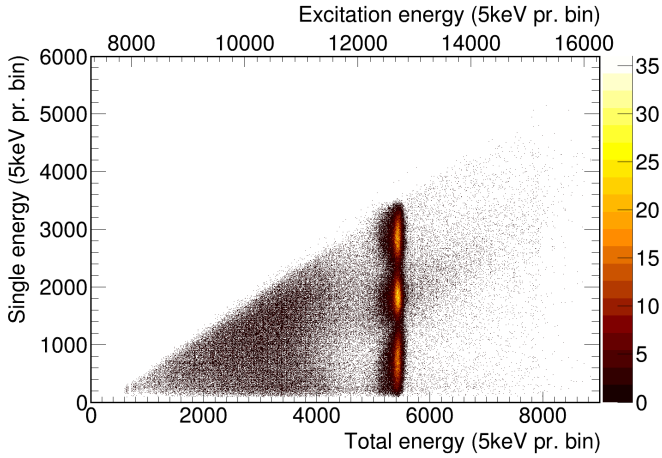

(b) Decays with $E_{23} > 250\,\mathrm{keV}$.

Figure 6.7: Decays through the ground state peak in ^{8}Be produce one α particle with two thirds of the available energy, while two other α particles share the remaining third (a). Decays through the first excited 2^{+} state or the 0^{+} ghost are shown in (b).

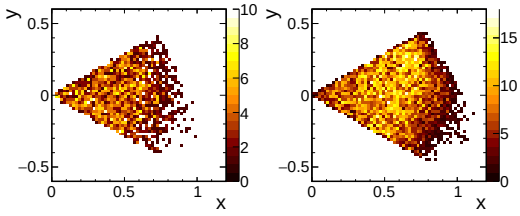

(a) 600 keV–2000 keV and 2000 keV–3000 keV.

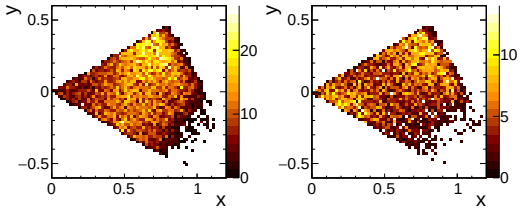

(b) 3000 keV–4000 keV and 4000 keV–5000 keV.

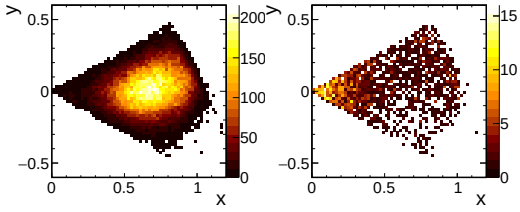

(c) 5000 keV–5600 keV and 5600 keV–6600 keV.

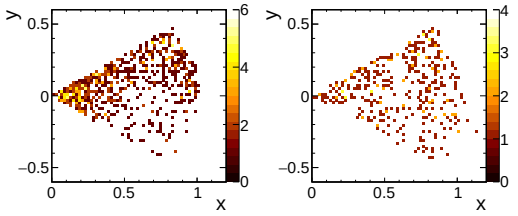

(d) 6600 keV–7600 keV and 7600 keV–9000 keV.

Figure 6.8: Data with $E_{23} > 250\,\text{keV}$ in Dalitz plots for different ranges of E_{tot}. The plots are divided into 60×60 bins.

7

SIMULATION

In an experiment using just one detector it is fairly simple to determine the detection efficiency and resolution. In an experiment like ours the situation is more complicated, since the detection efficiency depends not only on the total energy of the three α particles, but also on how the energy is shared between the three alphas and in which direction they are emitted. This means that the efficiency becomes a function of the the total energy, E_{tot}, and the phase space coordinates, x and y. Furthermore, as described in Section 6.2, several cuts are imposed on the data, and the acceptance of each cut is not exactly known. One way to learn more about the detection efficiency is to use Monte Carlo simulations. A proper simulation also teaches us of the resolution and line shape that we can expect from the experiment and, finally, we get the possibility to investigate potential background contributions.

7.1 SIMULATING AN EVENT

The simulation follows a straightforward step-by-step procedure which can be outlined as follows:

1. Determine the decay point (x, y, z).
2. Choose a value for $Q_{3\alpha}$.
3. Determine Q_β and add $\beta\nu$ recoil to the excited ^{12}C nucleus.
4. Generate the four-momenta of the three emitted α particles.

5. Determine which detector and pixel is hit by each particle.
6. Calculate the energy losses in target foil and detector dead layers.
7. Determine the detector response.

The first step is necessary because the beam spot is not a point, but rather some kind of spatial distribution determined by the beam line optics and various collimators. Which distribution to choose for the x, y position is discussed in Section 7.2. The z coordinate of the beam spot is in this case equivalent to the implantation depth of the ion in the target foil. We already simulated the implantation depth distribution with SRIM in Section 4.2.1, so to find z is just a matter of sampling the distribution in Figure 4.3.

7.1.1 Adding $\beta\nu$ recoil

To simulate the $\beta\nu$ recoil for a given Q_β it is necessary to know the distribution functions for the kinetic energy of the positron, T_β, and the angle between the positron and the neutrino, $\theta_{\beta\nu}$. The kinetic energy distribution is found with the help of Fermi's golden rule, which tells us that the transition rate is proportional to the final density of states, i.e.

$$W_T dE_\beta \sim n_\nu(E_\nu) n_\beta(E_\beta) dE_\beta. \tag{7.1}$$

With the density of states being determined purely by the available phase space of the positron and the neutrino, the distribution can be rewritten as

$$W_T dE_\beta \sim p_\nu E_\nu p_\beta E_\beta dE_\beta, \tag{7.2}$$

and, finally, by substituting $E_\beta = T_\beta + m_\beta c^2$ and $E_\nu = Q_\beta - T_\beta$ and assuming the neutrino to be perfectly massless we get

$$W_T dT_\beta \sim \sqrt{T_\beta^2 + 2T_\beta m_\beta c^2}\,(T_\beta + m_\beta c^2)(Q_\beta - T_\beta) dT_\beta. \tag{7.3}$$

In this derivation we ignored the electrostatic screening factor, which is permissible when dealing with high values of Q_β and low nuclear charge.

The distribution relevant for the angular correlations between the positron and the neutrino is stated in (Hamilton 1947):

$$W_\theta d\Omega_{\beta\nu} = \left(1 - \frac{p_\beta c}{3E_\beta}\cos\theta_{\beta\nu}\right) d\Omega_{\beta\nu}. \tag{7.4}$$

To simplify this expression a bit we introduce the total positron energy in units of its rest mass, $w = T_\beta / m_\beta c^2 + 1$, and, since Equation (7.4) does not depend on the azimuthal angle, we can substitute $x = \cos\theta_{\beta\nu}$ and find

$$W_\theta dx \sim \left(1 - \frac{\sqrt{w^2-1}}{3w}\, x\right) dx. \tag{7.5}$$

In practice, the distributions (7.3) and (7.5) are sampled with the `GetRandom()` method of the `TF1` class in the ROOT library, (Brun and Rademakers 1997), and the azimuthal angle, $\phi_{\beta\nu}$, is sampled from a uniform distribution between `0` and 2π. When combined these quantities determine the magnitude and direction of the nuclear recoil momentum.

The fourth step of the simulation procedure is to generate a three-α state which is allowed by total energy and momentum conservation. The ROOT library contains a generator class, `TGenPhaseSpace`, which does exactly that. Furthermore, it calculates an associated weight such that, when the generated events are sampled according to their weight, the resulting sample is uniformly distributed in phase space. Next, Equations (3.7) and (3.8) are combined to find the theoretical weight of the generated three-particle state. When multiplied, the phase space weight and the theoretical, model dependent, weight determine the total weight of the particular event. Knowing the maximum value of the total weight it is then possible to use the standard von Neumann method of accepting or rejecting the event in the simulation, see (Von Neumann 1951).

From the generated four-vectors it is possible to determine which detectors, if any, are hit by the three α particles, and in which pixels. To calculate the energy losses in foil and detector dead layer we use the range inversion method described in Section 6.1.2, only now the method is reversed, such that

$$E_f = R^{-1}(R(E_i) - \Delta x), \tag{7.6}$$

where Δx is the distance travelled in the foil/dead layer.

7.1.2 Simulating detector response

The final step of the simulation is to simulate a realistic detector response to the incident α particles. The detector response was already described in Section 5.4, however, an explanation of the line shape was not attempted. A discussion of the response of unsegmented silicon detectors to α particles is found in (Steinbauer et al. 1994), and we shall review only the main points here.

When an α particle hits the detector, it travels through the dead layer and some of its energy is lost. Until now we have claimed this energy loss to be exactly predictable, but since the stopping is a statistical process there is in fact also an energy-loss straggling involved, leaving initially mono-energetic α particles with a spread in kinetic energy as they enter the active volume of the detector. Also, variations in the dead layer thickness across the detector may introduce a further broadening of the particle spectrum.

The α particle is now stopped in the active region of the detector. Most of the kinetic energy is lost through interaction with and excitation of the electrons in the silicon crystal, but in rare events the alphas may also collide with the silicon nuclei. Some of the energy lost in nuclear collisions still becomes available to electronic excitation as the recoiling silicon nucleus is brought to a halt, but the remaining energy is lost in the production of crystal defects and lattice vibrations.

The total energy deposited as electronic excitation is spent on the production of electron-hole pairs, each pair requiring on average $\epsilon = 3.62\,\mathrm{eV}$ to create. This is again a statistical process, resulting in a spread on the created number of electron-hole pairs. If the pair production process was a true Poissonian process we would expect the spread on the number of produced pairs, N, to be on the order of $\sqrt{N} = \sqrt{E/\epsilon}$, however, the observed spread is somewhat smaller (for silicon around a factor of three), indicating that the pair production events do not happen independently, see also (Knoll 2000).

Finally, the electrons and the holes drift towards the contacts on either side of the detector, the charge signal is converted to a voltage signal in the pre-amplifier and the electronic resolution of the entire pre-amplifier/amplifier/ADC-

chain is folded into the signal. This part of the discussion is summarised in Table 7.1. Through extensive simulations and theoretical calculations it was shown

Table 7.1: Four physical factors that contribute to the broadening of the observed line shape of a mono-energetic α source.

Process	*Shape*
Energy-loss straggling in dead layer	Gaussian
Electronic excitation by the α particles	Asymmetric
Electron-hole pair statistics	Gaussian
Resolution of amplifier/ADC-chain	Gaussian

by (Steinbauer et al. 1994) that the line shape of Equation (5.11) provides an excellent fit to the line shape resulting from the already mentioned effects, however, the low-energy tails are predicted to be much less pronounced than what is observed in the present experiment, or indeed in most experiments involving DSSSDs.

One explanation could be that the pronounced low-energy tails are an inter-strip effect, where some of the free charge-carriers are captured in the anomalous electric field in the region between two contact strips. In such a case, the line shape asymmetry would be a property inherent to the detector itself. Another explanation could be that the spectrum from the α calibration source is not mono-energetic, but shows a large asymmetry. We found the average energy loss in the source to be around 4.5 keV in Section 5.1.2, so it is hard to imagine that a significant fraction of the emitted α particles should experience energy losses of hundreds of keV (although it can happen if some of the radioactive nuclei have channeled deeply into the source base material during the preparation of the source).

Since it is beyond the scope of the present work to do a microscopic simulation of the detector response, a simple parametrisation of the detectors' behaviour is proposed: The first three contributions to the broadening of the signal listed in Table 7.1 are grouped together in what we can call the "physical" response of the detector. These effects determine the distribution of the energy equivalent to the number of generated electron-hole pairs, which we describe

with a Gaussian folded with two exponential tails, characterised by its width, σ_{phys}, and the tail parameters τ_1, τ_2 and η. The last broadening effect is due to the finite electronic resolution of the amplifier/ADC-chain connected to the front and back strips, described by Gaussians of width $\sigma_{\text{F,el}}$ and $\sigma_{\text{B,el}}$.

If we denote the kinetic energy of the incident α particle E_α, then the energies corresponding to the observed pulse heights are

$$\begin{aligned} E_{\text{F}} &= E_\alpha + \delta E_{\text{phys}} + \delta E_{\text{F,el}} \\ E_{\text{B}} &= E_\alpha + \delta E_{\text{phys}} + \delta E_{\text{B,el}}. \end{aligned} \tag{7.7}$$

If we for a moment disregard the asymmetry and only concern ourselves with the Gaussian parts, the widths of the observed peaks must obey the relations

$$\begin{aligned} \sigma_{\text{F}}^2 &= \sigma_{\text{phys}}^2 + \sigma_{\text{F,el}}^2 \\ \sigma_{\text{B}}^2 &= \sigma_{\text{phys}}^2 + \sigma_{\text{B,el}}^2 \end{aligned} \tag{7.8}$$

Also, we can form the quantity $E_{\text{F-B}} = E_{\text{F}} - E_{\text{B}}$, and from the expressions in (7.7) we see that $E_{\text{F-B}}$ follows a Gaussian distribution of width

$$\sigma_{\text{F-B}}^2 = \sigma_{\text{F,el}}^2 + \sigma_{\text{B,el}}^2. \tag{7.9}$$

The quantities σ_{F}, σ_{B} and $\sigma_{\text{F-B}}$ are found by fitting to the calibration data, and thus (7.8) and (7.9) constitute a set of three equations with three unknowns, which we can easily solve for σ_{phys}, $\sigma_{\text{F,el}}$ and $\sigma_{\text{B,el}}$. For the tail parameters we use the values obtained from fits to calibration data in Section 5.4.

The simulation of the detector response to an α particle in practice involves sampling three distributions. First, δE_{phys} is found by randomly sampling a Gaussian folded with two exponential tails and second, $\delta E_{\text{F,el}}$ and $\delta E_{\text{B,el}}$ are found by a random sampling of the appropriate Gaussian distributions. These quantities are then added to E_α and recorded as the observed signal.

This simple way of modelling the detector response has some drawbacks, which we should be aware of. First of all, the model assumes the same electronic resolution in all front strips and all back strips, which does not always hold in practice. Secondly, the extraction of parameters from calibration data only

works if the individual strips are perfectly calibrated with no offset between them. If these conditions are not fulfilled there is no guarantee that equations (7.8) and (7.9) have a real solution. The third issue is that the parameters are extracted from calibration data where $E_\alpha \sim 5.8\,\text{MeV}$, but this is really at the extreme end of the spectrum from ^{12}N, and the majority of the detected alphas have energies below 1 MeV. As discussed earlier, the physical process causing the asymmetric tails in the response is not entirely understood, and it is not obvious how these parameters shoul be extrapolated to lower energy. In this simulation we assume all detector parameters to be independent of energy.

Table 7.2: The parameters used to simulate the response of the DSSSDs to incident α particles. The numbers in the last column are calculated from the values in the preceding three columns.

Detector	σ_{phys} (keV)	$\sigma_{\text{F,el}}$ (keV)	$\sigma_{\text{B,el}}$ (keV)	$\sigma_{\text{E,calc}}$ (keV)
U1	5.0	12.0	11.6	9.7
U2	4.2	9.5	8.0	7.5
U4	3.0	5.3	6.6	5.2
U5	2.3	11.3	13.2	9.0
U6	3.7	10.0	10.5	8.1

Having described the entire simulation procedure, it would now be interesting to test its performance against real data. In Figure 7.1 we see the simulated spectrum described in Section 7.3 compared to the experimental spectrum. The dominating component is the 1^+ state at 12.7 MeV excitation energy. We note that the observed peak is shifted 20 keV with respect to the simulated peak. Also, the observed peak is somewhat broader than the simulated, with a FWHM = 110 keV compared to FWHM = 80 keV. At first glance this is not very convincing, but I believe some of the discrepancy can be explained with a drift in the calibration, which is observed during the experiment. Energy shifts of as much as 10 keV are observed for some detectors between the the calibration runs in the beginning and the end of the experiment. With no sharp peaks in the single α spectrum it is not possible to track the drift through the ^{12}N runs, and so we must accept a systematic uncertainty in the total energy spectrum of

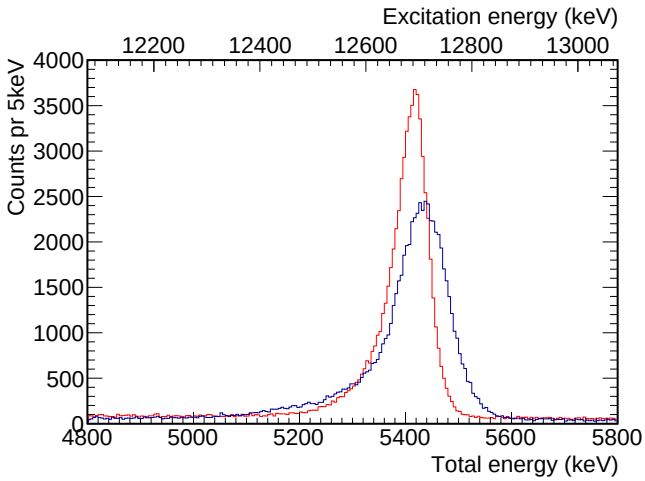

Figure 7.1: A zoom of the data (blue spectrum) around the 1^+ peak compared to the line shape from the Monte Carlo simulation (red spectrum).

around 20 keV.

7.2 Acceptance and sensitivity

In this section we try to learn about the detection efficiency and its dependence on input parameters, such as dead layer thickness, detector geometry, etc. All the relevant input parameters were found in Chapter 5, except for the beam spot size.

To do the simulation properly it is necessary to take the finite beam-spot size into account. The beam-spot size is not readily available for measurement, and the only way to learn about it is to compare results from the simulations with experimental data. To do this I have chosen to simulate decays through the ^{8}Be ground state peak with total energies ranging from 500 keV to 5000 keV, since this is most common type of decay in the experimental data. It is evident from the results in Figure 7.2 that the beam-spot size has a significant influence on the measured distribution of total momentum, which becomes broader as the spot

size is increased. Several sizes of the beam spot as well as various distribution

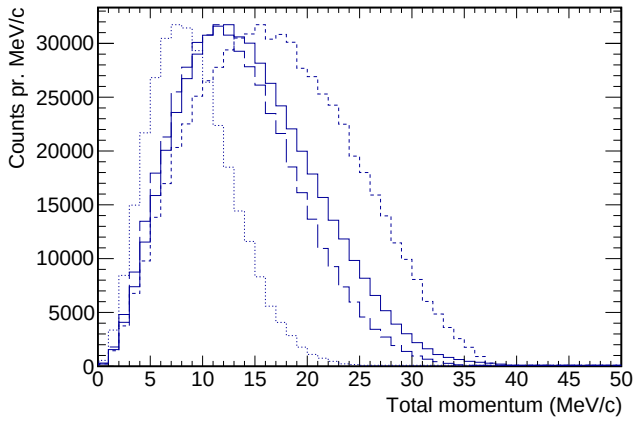

Figure 7.2: Total momentum distribution from the experimental data (solid line) compared to simulations with a beam spot size of 3 mm (dotted line), 6 mm (long dashed line) and 9 mm (short dashed line).

functions were tried, and a uniform distribution with a diameter of 6 mm seems to best fit the data. From Figure 7.2 the uncertainty on this figure is estimated to be on the order of 1 mm.

In Chapter 5 we did a careful calibration of the setup, finding values for the carbon foil thickness, the thickness of detector dead layers and the general geometry of the detector array. These results, however, come with an uncertainty, and it is not immediately clear how the uncertainties would affect the results from the data reduction.

In order to investigate this matter ^{8}Be ground state decays as well as uniform phase space decays were simulated in the energy range from 500 keV to 9000 keV. The 10^6 simulated decays are passed through the data reduction and the overall acceptance is found by comparing the resulting spectrum with the spectrum of simulated decays. The effect on the acceptance of varying the input parameters, one at a time, gives a rough idea of the sensitivity to variations in each parameter.

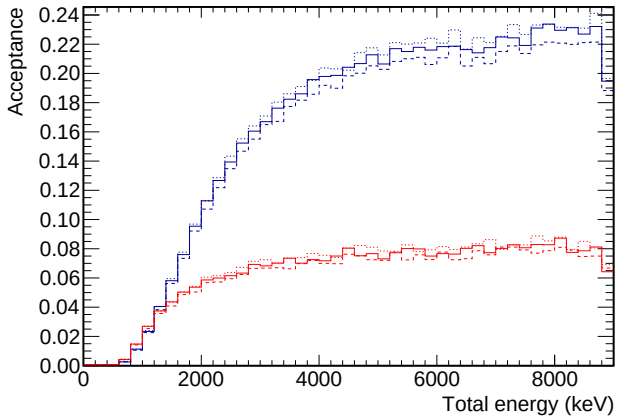

Figure 7.3: Total acceptance for a uniform beam spot with a diameter of 5 mm (dotted line), 6 mm (solid line) and 7 mm (dashed line). The blue lines indicate the results for ^{8}Be ground state decays, while the red lines show results for uniform phase space decays.

The effect of varying the beam-spot size is seen in Figure 7.3. The first thing that should be noticed is the rather large difference between the acceptance of ^{8}Be ground state decays and uniform phase space decays. The red and blue curves in the figure follow each other to around 1400 keV, where the red curve starts to flatten, whereas the blue curve keeps rising to around 5000 keV. This can be understood as an effect of the small relative energy of the two low-energy alphas emitted in the ^{8}Be ground state decay, α_2 and α_3. When the total available energy rises, the opening angle between α_2 and α_3 becomes smaller, and at large total energies they are essentially emitted back-to-back with α_1. Since the setup contains four DSSSDs facing each other in pairs, the chance of detecting this type of decay is very high. Varying the beam-spot size from 5 mm to 7 mm results in systematic shifts in the acceptance of approximately 10 %.

Figure 7.4 shows how variations in the geometry affects the acceptance. The detector positions were randomly varied within 1 mm from the positions found in Section 5.2, and in all circumstances the acceptance is systematically lowered, sometimes with as much as 10 %.

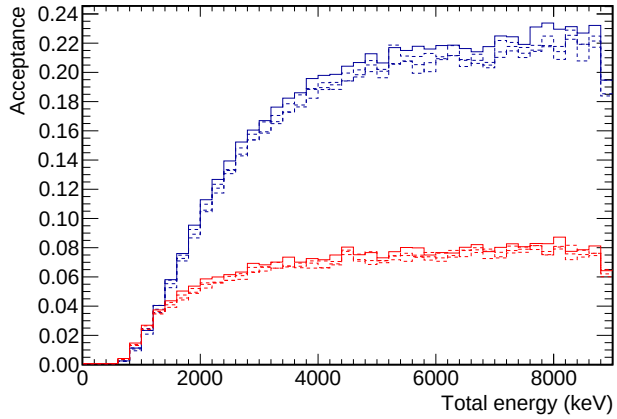

Figure 7.4: Total acceptance for various geometries. The solid line shows the acceptance if the geometry is accurately known while the dashed lines show results for simulations where the individual detectors have been moved around within a 1 mm uncertainty. Blue lines are ^{8}Be ground state decays and red lines are uniform phase space decays.

Similar analyses were done by modifying the foil thickness ±5 % and the detector dead layer thicknesses within ±10 %. None of these uncertainties seem to have a strong impact on the estimated acceptance, producing only changes within ±3 %.

It is clear from the previous discussion that the acceptance is quite sensitive to the decay mechanism, which follows from the fact that the acceptance depends both on the total energy and the Dalitz coordinates. This means that a uniform phase space decay does not appear as a uniform distribution in the Dalitz plot after simulation and data reduction. To illustrate the effect a simulation of 4×10^7 phase space decays were made and Dalitz plots exactly equivalent to the ones in Figure 6.8 are shown in Figure 7.5. The color axis represents the probability for a single decay to end up being observed in the individual bins.

There are a few features in Figure 7.5 that we should note: First, there are some regions in the Dalitz plot, especially at low energy, where we do not observe any counts; “blind” spots, so to speak. The blindness in the upper right

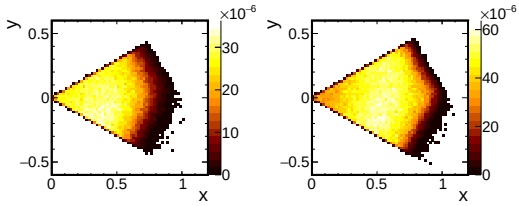

(a) 600 keV–2000 keV and 2000 keV–3000 keV.

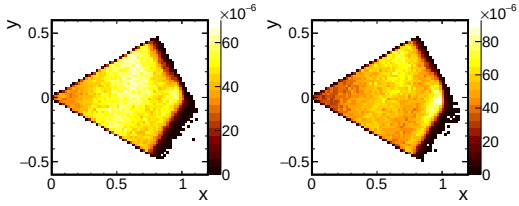

(b) 3000 keV–4000 keV and 4000 keV–5000 keV.

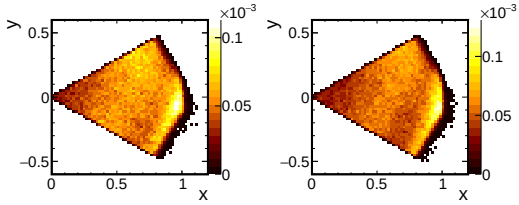

(c) 5000 keV–5600 keV and 5600 keV–6600 keV.

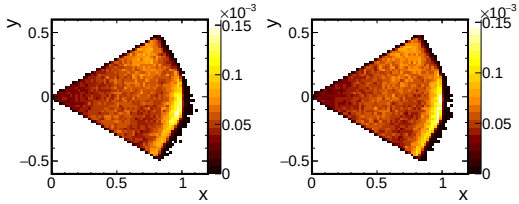

(d) 6600 keV–7600 keV and 7600 keV–9000 keV.

Figure 7.5: Acceptance for different ranges of E_{tot}, found by simulation of uniform phase space decays. The plots are divided into 60×60 bins.

corner is caused by the low energy thresholds of the detectors. The thresholds mean that there is a minimum detectable energy, putting a limit on $3E_3/E_{\text{tot}}$, refer again to Figure 3.2. The blindness in the lower right corner is a result of the cut on the relative energy of α_2 and α_3, $E_{23} > 250\,\text{keV}$, refer to the discussion in connection with Equation (6.5). Second, apart from those two blind spots, the entire phase space is fairly evenly covered by the experiment, except for the sharp rise in acceptance near the circular edge of the Dalitz plot where the α particles are emitted in a back-to-back fashion.

7.3 Background estimate

In Section 6.2 the various cuts of the data reduction were described. The cut on total energy and momentum of Equation (6.3) is used to separate triple-α coincidences from other events with three signals, for instance $\alpha\alpha\beta$ coincidences and $\alpha\alpha$ + noise. It would be very useful to know how many events are wrongly categorized as triple-α events, and where we can expect this background to disturb the spectrum and Dalitz plots.

The method we use is to mix real signals into the simulated data. For all real events where there are more than three α particle candidates, those three candidates are chosen which minimise the total momentum. We regard the remaining candidates as a potential source of background, since they could have resulted in a false triple-α identification, even if fewer than three α particles had been detected. These candidates are then stored in a separate file and mixed into the simulated event with some probability that has to be adjusted such that it reproduces the observed spectra.

The next job is to do a realistic simulation of the experiment. We try to synthesize the spectrum from three components: A narrow 1^+ resonance at 12.7 MeV excitation energy decaying through the ^{8}Be first excited 2^+ state. Also, we simulate decays through the ^{8}Be ground state peak, and we sample the total energy from the observed spectrum (the projection of Figure 6.7(a) onto the horizontal axis) corrected by the estimated acceptance (the solid blue line in Figures 7.3 and 7.4). The third component in the spectrum are those decays that are neither 1^+ nor ^{8}Be peak decays. Judging from the Dalitz plots in Figure 6.8

these decays follow a fairly uniform distribution in the Dalitz plot, and so we choose to approximate this component with a uniform phase space decay. The total energy is sampled from the observed spectrum (the projection of 6.7(b) onto the horizontal axis) corrected with the estimated acceptance (the solid red line in Figures 7.3 and 7.4).

The noise signals are mixed into each of the three components and the mixed data are passed through the data reduction routine. A plot of the total momentum vs. the total energy in events with three α particle candidates, similar to the plot in Figure 6.3, is shown for each of the three spectral components in Figures 7.6, 7.7 and 7.8. It is clear that the components produce distinct contributions

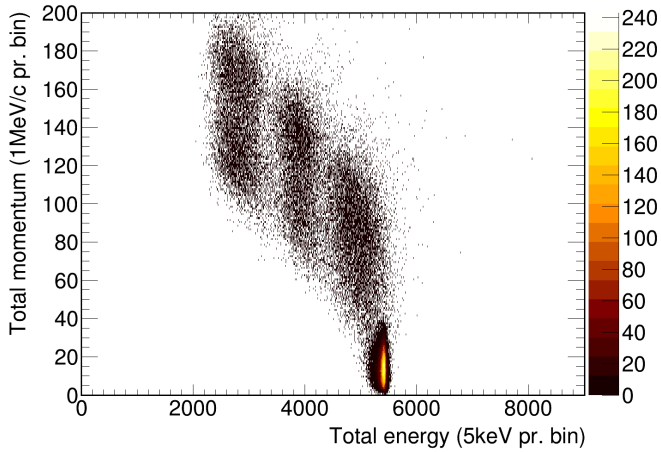

Figure 7.6: Simulated decays of a 1^+ resonance in ^{12}C at 12.7 MeV excitation energy mixed with β/noise signals from real world data.

to the background, and we recognise each contribution from the real world data in Figure 6.3. The 1^+ component gives three background "blobs", corresponding to each of the peaks in the single particle spectrum. The ^{8}Be ground state decays produce two blobs, the larger one corresponding to the loss of one of the low-energy alphas and the smaller blob corresponding to the loss of the most energetic α.

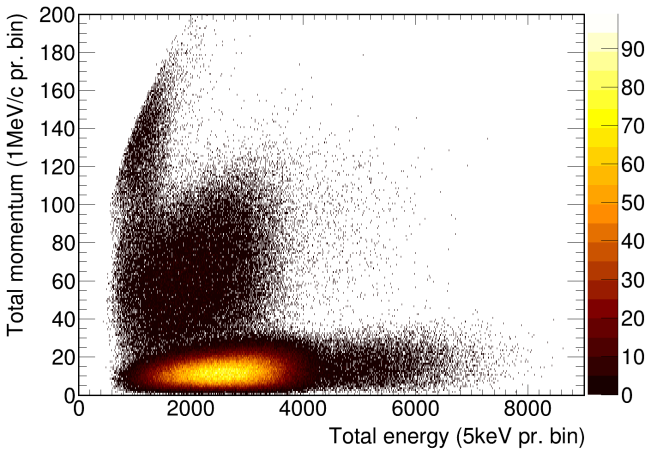

Figure 7.7: Simulated decays through the ^{8}Be ground state peak mixed with β/noise signals from real world data.

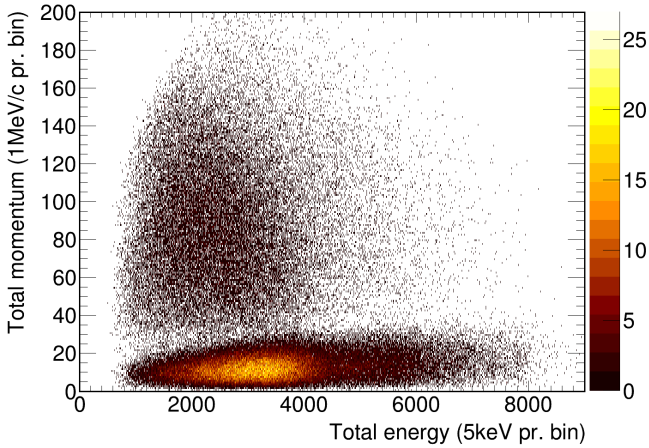

Figure 7.8: Simulated uniform phase space decays mixed with β/noise signals from real world data.

It is now a straightforward task to attach an identifier to each β/noise signal and make a similar plot of only the false coincidences. This is shown in Figure 7.9 together with the energy-momentum cut from Equation (6.3). It is

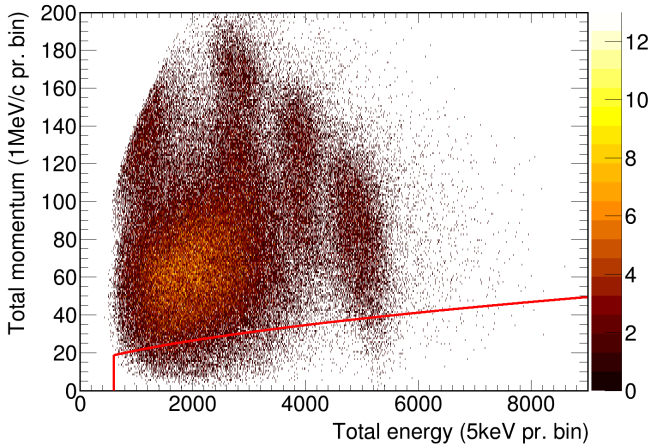

Figure 7.9: Misidentified triple-α coincidences, based on the synthesised decay spectrum and observed noise signals. The red line shows the energy-momentum cut of Equation (6.3).

evident that the energy-momentum cut is not completely succesful in rejecting the false coincidences. We are, however, now in a position where we can quantify the background and, furthermore, predict where in the Dalitz plot we should expect it to disturb. The total spectrum of all misidentified triple-α coincidences are shown in Figure 7.10, and the Dalitz plot of events with $E_{23} > 250\,\text{keV}$ are seen in Figure 7.11 Out of a total of 594000 accepted triple-α coincidences 7400 are misidentified, yielding an average background of 1.25 %. A similar figure holds for the ^{8}Be excited state channel.

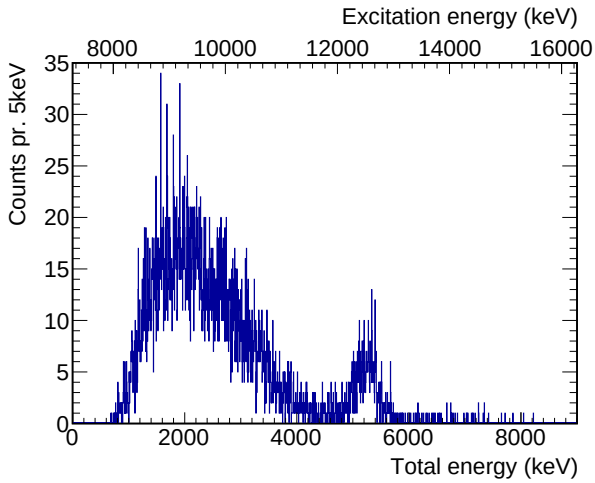

Figure 7.10: Total energy spectrum of the misidentified triple-α coincidences. Comparing with 6.5 we see that we should expect a background of between 1 % and 2 %.

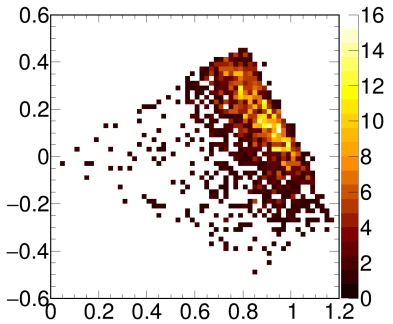

Figure 7.11: Total contribution from misidentified triple-α coincidences to the Dalitz plot of events with $E_{23} > 250\,\text{keV}$. The plot is divided into 60×60 bins.

8

Analysis & Discussion

In this chapter we investigate the experimental spectra in a bit more detail and also try to compare the data to the theoretical predictions of the sequential decay model. In Chapter 7 we built a framework for simulation of the experimental sensitivity to triple-α breakups. The next step is to combine the simulation tool with the sequential decay model described in Section 3.2.2 and find the phase space distributions we should expect to observe from the various breakup modes.

8.1 A narrow level

The goal is to be able to fit a combination of different breakup modes to the broad resonant structures in ^{12}C, however, before we start to combine several decay modes in a fit, it is instructive to check that the method works for the simpler case of a narrow resonance of known J^π, namely the 1^+ resonance at 12.7 MeV excitation energy.

For events with $E_{23} > 250\,\text{keV}$ and $5335\,\text{keV} < E_{\text{tot}} < 5535\,\text{keV}$ the single α particle energies are shown in Figure 8.1. In the sequential breakup picture, the interpretation of the three peaks in the spectrum is that the first α particle is emitted with two thirds of the energy released in the first breakup, $E_{\text{tot}} - E_{2^+}$, and it ends up in the middle peak of the spectrum. The ^{8}Be recoil is left in the excited 2^+ resonance. When the recoil breaks up, the α particle emitted in a forward direction (compared to the motion of the recoil) ends up in the high-energy peak, and the α particle emitted in the backwards direction is observed

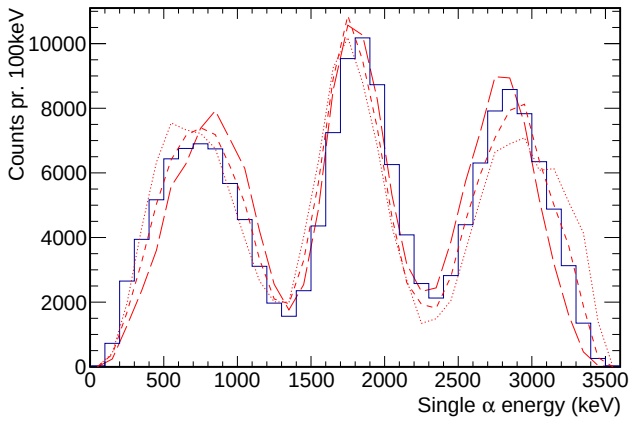

Figure 8.1: The blue line shows the single α particle spectrum from the breakup of the 12.7 MeV resonance in ^{12}C. The red lines show the simulated spectrum without the Coulomb correction (dotted) and with the Coulomb correction for $\tilde{R} = 17$ fm (short dashed) and $\tilde{R} = 10$ fm (long dashed).

in the low energy peak.

Also plotted in the figure is the spectrum from a simulation using the ^{8}Be(2^+) level parameters $E_{2^+} = 3129(6)$ keV and $\gamma^2 = 1075(9)$ keV, obtained from (Bhattacharya et al. 2006), and the effect of the final state Coulomb interaction, described in Section 3.2.2, is illustrated. We see that the low-energy peak and the high-energy peak are shifted towards higher and lower energies, respectively, by the Coulomb correction. This can be understood if we consider the extreme case of a collinear breakup. Here, the high-energy α particle is emitted with maximum energy and the low-energy α particle is emitted with minimum energy. This decay mode is suppressed by the final state Coulomb interaction, which explains the shift of the two outer peaks. A value for the correction radius of $\tilde{R} = 17$ fm is found to provide the best fit to data, which is a bit surprising since a value of 10 fm was used by (Fynbo et al. 2003) to obtain a decent fit.

Even though the agreement between data and simulation is improved by applying the Coulomb correction, the middle peak is still systematically shifted

between the two. As already mentioned, we interpret this peak as originating from the first α particle emitted in the breakup. Therefore, its position effectively measures the energy of the 2^+ resonance in ^{8}Be. We see a similar disagreement in the earlier works by (Diget et al. 2009) and (Kirsebom et al. 2010), and we are led to suspect that the shift is related to proper physics, and is not just caused by some systematic error in the present analysis.

If we treat E_{2^+} as a free parameter and do simulations for an extended range of values, we obtain the best agreement with data using a value of $E_{2^+} = 2940\,\text{keV}$, see Figure 8.2. This value is not compatible with the very accurate result from

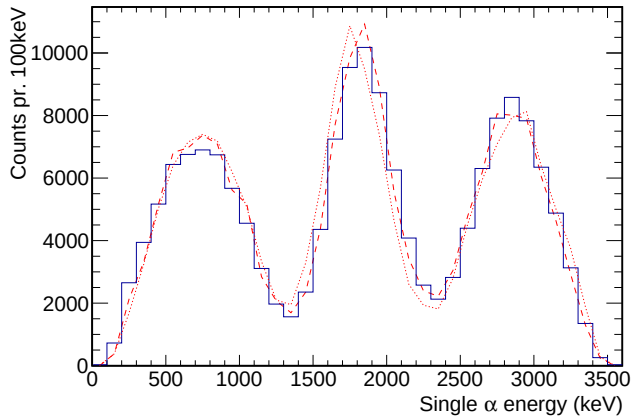

Figure 8.2: The single α particle spectrum from the breakup of the 12.7 MeV resonance in ^{12}C. The red, dashed line and the red, dotted line show the simulated spectrum for $E_{2^+} = 2940\,\text{keV}$ and $E_{2^+} = 3129\,\text{keV}$, respectively.

(Bhattacharya et al. 2006), however, that result was found using the β decay of ^{8}Li and ^{8}B to populate the 2^+ resonance in ^{8}Be. It is well known that the observed energy and width of a resonance is dependent on the reaction channel used to populate the resonance, and the effect on the 2^+ resonance in ^{8}Be in particular was studied by (Berkowitz 1964), (Overway et al. 1981) and (Ricken et al. 1990). A more theoretical approach was taken by (Riisager et al. 2015) to show that populating broad, particle-emitting, resonances through β decay leads to

distortion of the observed spectra; an effect caused by the possibility for direct decay to the continuum.

It would be interesting to make a more detailed fit of the 2^+ parameters to these data, allowing also the width and channel radius, which in this analysis were kept fixed at $\gamma^2 = 1075\,\text{keV}$ and $a = 4.5\,\text{fm}$, to vary. From the foregoing discussion it seems that such an analysis would be quite robust to uncertainties in the decay model, since the position and shape of the middle peak in Figure 8.1 are not very sensitive to variations in $\tilde{R}$. Historically, the existence of a first excited state at 3 MeV in ^{8}Be was actually proposed based on observations of triple-α breakups following the $p + ^{11}$B reaction by (Dee and Gilbert 1936). In those days it was already possible to measure triple-α coincidences in complete kinematics... by using a cloud chamber.

8.1.1 Projections of the phase space distribution

Our next job is to check if the simulations reproduce the observed phase space distribution of the 1^+ resonance. In order to do this we introduce three new coordinates, ρ, ξ and η. These coordinates are defined in Figure 8.3 and can be

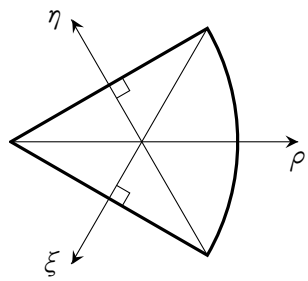

Figure 8.3: Definition of three coordinate axes in phase space. Note that ρ is a radial coordinate and not equal to the previously defined x coordinate.

calculated from the ordinary Dalitz (x, y) coordinates:

$$\begin{aligned} \rho &= \sqrt{x^2 + y^2} \\ \frac{2\xi}{\sqrt{3}} &= -\frac{x}{\sqrt{3}} - y + 1 \\ \frac{2\eta}{\sqrt{3}} &= -\frac{x}{\sqrt{3}} + y + 1 \end{aligned} \tag{8.1}$$

Projecting the data onto these axes results in one-dimensinal histograms, from which it is easier to get a clear impression of the phase space distributions. This particular choice of axes is chosen to reveal any nodes in the phase space distribution along the edges of the Dalitz plot and is inspired by (Kirsebom 2013).

The projections for the 1^+ resonance are shown in Figure 8.4 together with the results from simulations. We note that the distributions vanish at the edges, as is expected for a 1^+ state (Zemach 1964). Also, the agreement between the experimental data and the simulation seems to be reasonable. We expect that the values for $\tilde{R}$ and E_{2^+} in ^{8}Be that fits the 1^+ resonance are also the values that provide the best fit to the rest of the data set, even though E_{2^+} differs from the value found in β decay experiments.

8.1.2 Total yield of ^{12}N

Another piece of information that can be extracted from the 1^+ decays is the total number of ^{12}N ions delivered to the experimental setup during the experiment. The number of events with $5000\,\text{keV} < E_{\text{tot}} < 5600\,\text{keV}$ is 6.87×10^4. The background from broad resonances is approximated in this energy range with a linear function, resulting in a background estimate of 1.7×10^3. The estimated area of the peak is therefore 6.71×10^4. Through simulations we find the detection efficiency for this level to be $\epsilon = 0.076(8)$, allowing for at least 10 % uncertainty, as discussed in Section 7.2. From (Hyldegaard et al. 2009) we find the β decay branching ratio to the 1^+ state to be $\text{BR}_\beta = 0.120(3)\,\%$. Combining

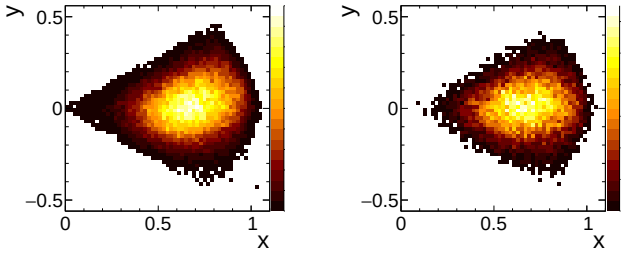

(a) Left panel: Dalitz plot of observed breakups with 5335 keV < $Q_{3\alpha}$ < 5535 keV. Right panel: Simulated (1,2,2) breakups for the same range of $Q_{3\alpha}$.

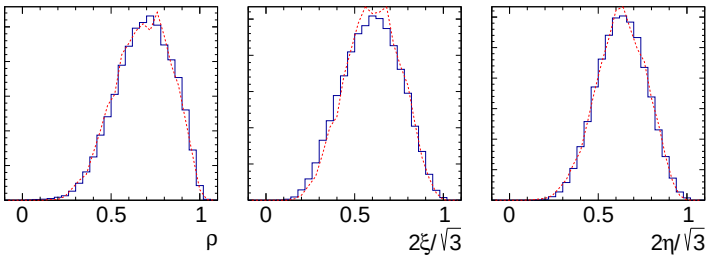

(b) Data from the breakup of the 1^+ resonance in ^{12}C projected along the axes defined in Figure 8.3. The red, dotted lines show the result from simulations.

Figure 8.4: Comparison of simulation and experiment for the 12.7 MeV 1^+ resonance.

this information, our best estimate of the total number of ^{12}N decays is

$$N_{\text{dec}} = \frac{N_{\text{obs}}}{\epsilon \text{BR}_\beta} = 7.4(9) \times 10^8. \tag{8.2}$$

With a total beam time of approximately 150 h this translates to a yield of 1370(150) ions/s from the IGISOL.

8.2 DECAYS THROUGH ^{8}Be(0^+)

In Section 6.2.3 it was described how the observed triple-α coincidences are divided into two categories according to the relative energy of the two lowest-energy alphas, in the following labelled ^{8}Be(peak) and ^{8}Be(exc) decays. The ^{8}Be(peak) decays provide a trivial contribution to the observed phase space distribution, and so the detailed fit of the various decay modes is applied only to the phase space distribution of the ^{8}Be(exc) decays. Still, the ^{8}Be(peak) decays can be used to put a constraint on the fitting parameters, effectively reducing the problem with one degree of freedom.

The spectrum of ^{8}Be(peak) decays is shown in Figure 8.5. We use the de-

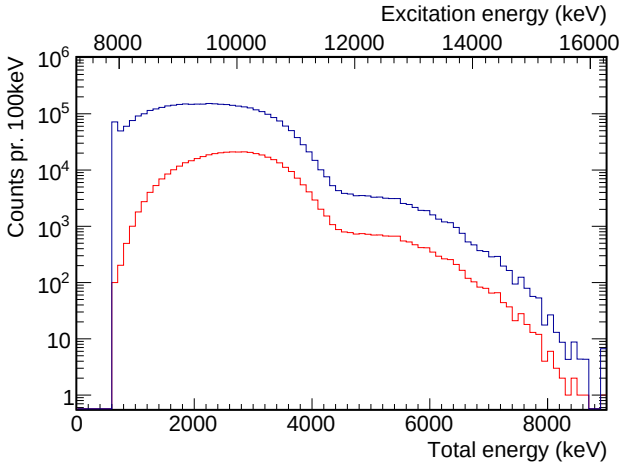

Figure 8.5: The red line indicates the observed spectrum of ^{8}Be(peak) decays. The blue line shows the same spectrum corrected for detection efficiency as determined in Section 7.2.

tection efficiency determined in Section 7.2 to calculate the true spectrum of these decays, which is also shown in the figure. In Section 2.3.1 we discussed the phenomenon of ghosts in relation to the 0^+ ground state in ^{8}Be, and we found the branching ratios for decay to the peak and the ghost, respectively.

This means that from the ^{8}Be(peak) spectrum it is possible to predict the contribution of ^{8}Be(0^{+}) decays to the ^{8}Be(exc) spectrum and the corresponding phase space distributions, the only free parameter being the relative strength of 0^{+} and 2^{+} resonances in ^{12}C.

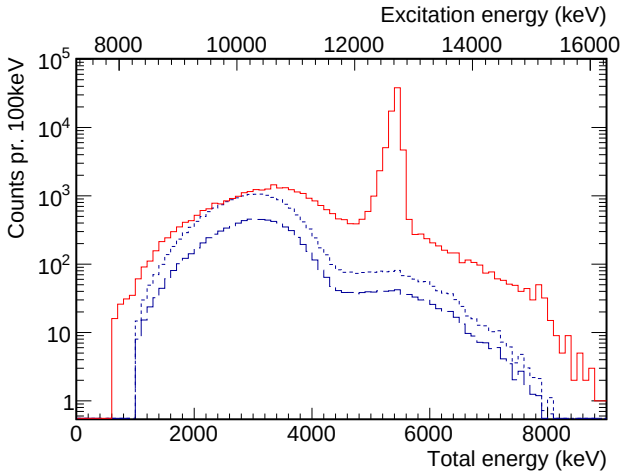

Figure 8.6: The red line shows the observed ^{8}Be(exc) spectrum. The blue lines show the predicted ^{8}Be(0^{+}) contribution to the spectrum assuming pure 0^{+} strength in ^{12}C (short dashed) and pure 2^{+} strength in ^{12}C (long dashed).

The observed ^{8}Be(exc) spectrum is shown in Figure 8.6 together with the predicted contribution from decays through ^{8}Be(0^{+}), assuming either pure 0^{+} strength or 2^{+} strength in ^{12}C. The predicted spectra include the estimated detection efficiency for the appropriate decay modes. From the work by (Diget et al. 2005) and (Hyldegaard et al. 2010) we expect the 8 MeV–12 MeV range in excitation energy to be dominated by 0^{+} strength and if this is indeed the case, the ^{8}Be(0^{+}) contribution can explain almost the entire ^{8}Be(exc) spectrum up to around 3 MeV total energy. Below 2 MeV the discrepancy between the observed spectrum and the spectrum predicted from pure 0^{+} strength seems to indicate that we need a further decay mechanism, namely decay through ^{8}Be(2^{+}). It would be strange, however, if the contribution from decay modes

through ^{8}Be(2^+) became relatively more prominent at these low energies, since the breakup could only proceed through the extreme low-energy tail of the 2^+ resonance in ^{8}Be. I therefore find it most probable that the discrepancy is caused by background (see Figure 7.10 for the estimated background spectrum) and/or badly estimated detection efficiencies below 2 MeV and that the ^{8}Be(exc) spectrum is indeed dominated by breakups through ^{8}Be(0^+) up to 3 MeV. The same conclusion was reached by (Diget et al. 2009).

8.3 Broad resonances I: Two detailed fits

Figures A.2 to A.7 show simulated phase space distributions for six of the seven possible decay modes in four different energy ranges (the seventh mode, the (1,2,2) breakup, is treated independently). In addition to the standard Dalitz plots we have also introduced three new coordinates, ρ, ξ and η. In Figure A.1 the experimental data is shown in equivalent energy bins for visual comparison. Our job is to figure out which combination of breakup models best fits the observed distribution. We proceed by making a linear combination of the simulated models, i.e.

$$H_x(i) = \sum_j n_j h_x(i) + B_x(i), \tag{8.3}$$

where $x = \rho, \xi, \eta$, i is the histogram bin number and the sum is over $j = (000), (022), (220), \ldots$, $h_x(i)$ is a histogram of the simulated distribution, normalised to unit area. $B_x(i)$ is the background spectrum found by mixing simulated data with real β/noise-signals, as described in Section 7.3. The n_j coefficients are used as fitting parameters in a simultaneous fit to the ρ, ξ and η distributions, using the MIGRAD routine from the MINUIT2 library, included in the ROOT framework, (Brun and Rademakers 1997). The background contribution which we estimated in Section 7.3 is included in the fit.

In some parts of the spectrum there is a limited amount of statistics, and we therefore use a log-likelihood fitting method instead of standard χ^2 fitting. To

estimate the quality of a fit, we use a generalised χ^2:

$$\chi^2_\lambda = 2\sum_{i=1}^{M}\left(n_i \log\frac{n_i}{y_i} + y_i - n_i\right), \tag{8.4}$$

where M is the number of bins included in the fit, n_i is the observed number of counts in bin i and y_i is the number of counts predicted by the fit, see (Baker and Cousins 1984).

8.3.1 *Fitting in the 2.9MeV – 3.1MeV range*

As a starting point we consider only a limited energy range around $Q_\alpha = 3\,\text{MeV}$, corresponding to an excitation energy of 10.27 MeV. The choice of energy binning is a compromise between the total energy resolution of our experiment of FWHM = 110 keV, the energy dependence of the phase space distributions, and the fact that a reasonable number of counts in the bin is desirable. A bin width of 200 keV seems appropriate.

Table 8.1: Parameters for the fits described in this section. A "0" entry indicates that a model has been included in the fit, but that the fit converged toward zero contribution. A "-" entry indicates that the model has not been included in the fit.

	Fit 1	Fit 2	Fit 3	Fit 4	Fit 5
n_{000}	1178	2340	2340	1925	1484
n_{220}	912	-	-	418	748
n_{022}	128	-	0	-	113
n_{202}	127	-	-	-	-
n_{222}	0	-	-	-	-
n_{242}	0	-	-	-	-
R	1.53	1.09	1.09	1.34	1.49
ndf	135	140	139	139	138
χ^2_λ/ndf	1.155	1.279	1.288	1.163	1.135
p-value	0.1054	0.0145	0.0125	0.0921	0.1325

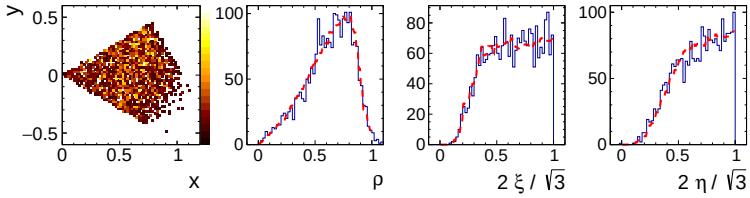

(a) The solid, blue line shows the experimental data while the dashed, red line shows the best fit (Fit 1 of Table 8.1).

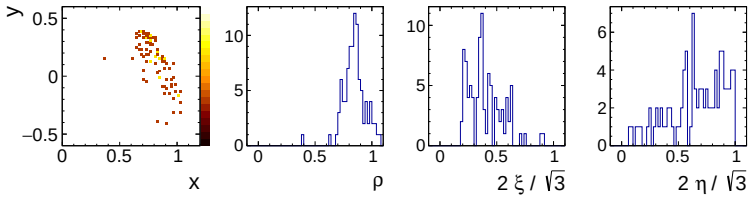

(b) Background contribution estimated from simulation and event mixing.

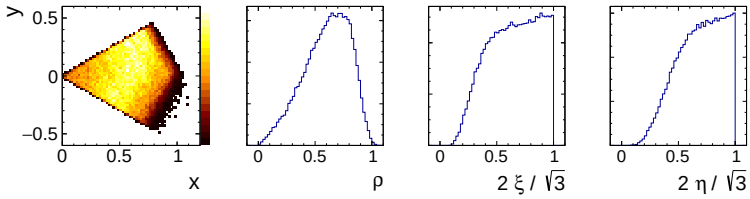

(c) Simulated (0,0,0) breakups.

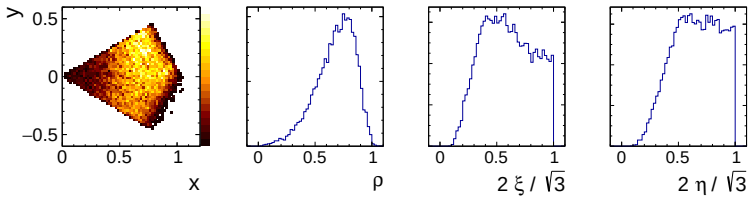

(d) Simulated (2,2,0) breakups.

Figure 8.7: A fit to experimental data with Q_α between 2.9 MeV and 3.1 MeV.

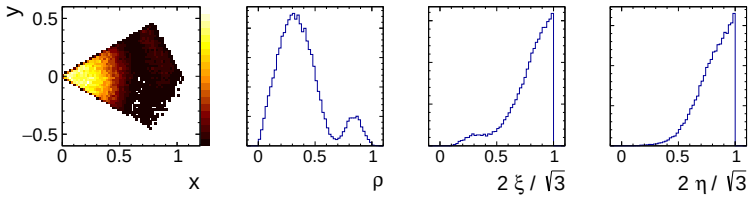

(e) Simulated (0,2,2) breakups.

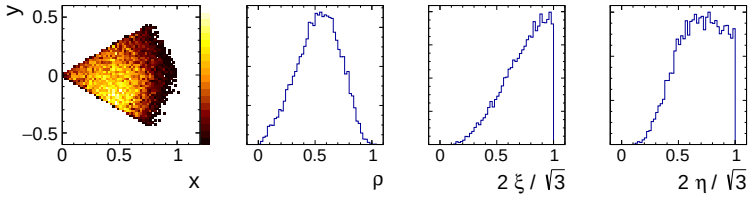

(f) Simulated (2,0,2) breakups.

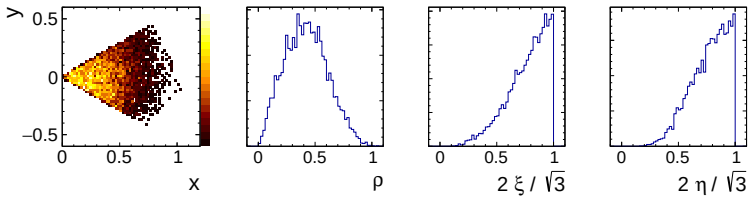

(g) Simulated (2,2,2) breakups.

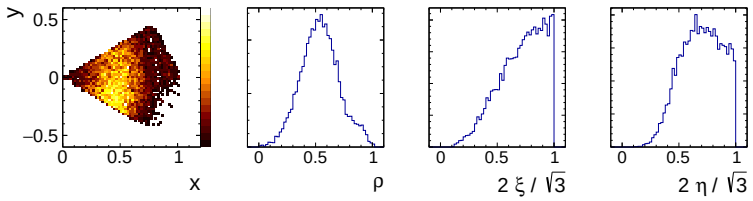

(h) Simulated (2,4,2) breakups.

Figure 8.7: Simulated breakups with Q_α between 2.9 MeV and 3.1 MeV.

If we allow all seven breakup modes to contibute to the fit, we get the result shown in Figure 8.7. The best fit parameters are found under "Fit 1" in Table 8.1. With the definition in Equation (8.3) we can interprete the coefficients as the number of observed decays attributed to each breakup mode. According to this fit, the spectrum is dominated by 2^+ strength in ^{12}C, which is a remarkable result and not immediately consistent with results from earlier β decay studies, (Fynbo et al. 2005; Diget et al. 2009; Hyldegaard et al. 2010).

The six models allowed in the fit are also shown in Figure 8.7. The challenge with this approach is that the observed distribution is quite uniform with no distinctive features. The (0,0,0) model gives an almost uniform phase space distribution by itself, however, comparing the alternative models of Figures 8.7(d) to 8.7(h) it is not impossible to imagine that a combination of these models could also result in a more or less uniform distribution. If several combinations of the models produce identical phase space distributions the fitting parameters would be strongly correlated and the fits unreliable. To test if this is the case, we try to fit the (0,0,0) distribution to a combination of the other models, and the result in Figure 8.8 shows that it is indeed possible to obtain quite a good fit to the

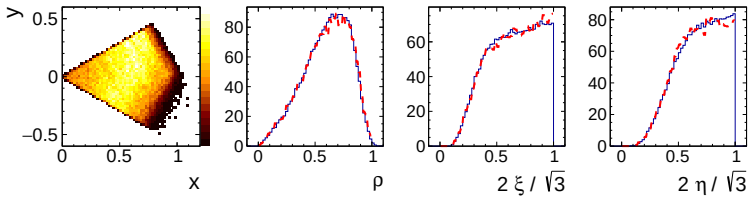

Figure 8.8: The solid, blue line shows the phase space distribution of simulated (0,0,0) breakups for Q_α between 2.9 MeV and 3.1 eV. The dashed, red line shows a fit where all but the (0,0,0) model are allowed to contribute.

pure (0,0,0) distribution, even if the (0,0,0) model is not allowed in the fit itself. The resulting parameters of this fit are found in Table 8.2, and the low value of χ^2/ndf confirms what we already concluded from the visual inspection of the fit, that it is a reasonably good fit.

The foregoing discussion shows that if we let all breakup models contribute, the obtained fit results are ambiguous, and it seems clear that some kind of con-

Table 8.2: Parameters for the fit shown in Figure 8.8.

n_{220}	1469
n_{022}	37
n_{202}	167
n_{222}	387
n_{242}	280
ndf	141
χ^2_λ/ndf	0.155
p-value	1

straints are needed in order to extract some useful information from the fitting. Following the ideas presented in Section 8.2 it is possible to calculate the number of ^{8}Be(0^+) peak decays from the observed number of ^{8}Be(0^+) ghost decays, i.e. from the fitting parameters n_{000} and n_{220}. If the total number of decays through the (0,0,0) and (2,2,0) modes are denoted N_{000} and N_{220}, the number of observed ^{8}Be(0^+) peak decays is

$$N_{\text{peak}} = \epsilon_{\text{peak}} \left[N_{000}(1 - \text{BR}_{000}) + N_{220}(1 - \text{BR}_{220}) \right]. \tag{8.5}$$

Here ϵ_{peak} is the detection efficiency for decays through the ground state peak and BR_{000} and BR_{220} are the branching ratios for (0,0,0) and (2,2,0) breakups through the ghost, which are plotted in Figure 2.4. Since the relations $n_{000} = \epsilon_{000}\text{BR}_{000}N_{000}$ and $n_{220} = \epsilon_{220}\text{BR}_{220}N_{220}$ must hold, we can rewrite Equation (8.5) such that we get the number of observed decays through the ground state peak directly from the fitting parameters:

$$N^{\text{fit}}_{\text{peak}} = \epsilon_{\text{peak}} \left[\frac{n_{000}}{\epsilon_{000}} \frac{1 - \text{BR}_{000}}{\text{BR}_{000}} + \frac{n_{220}}{\epsilon_{220}} \frac{1 - \text{BR}_{220}}{\text{BR}_{220}} \right]. \tag{8.6}$$

Using this result we form the ratio

$$R = N^{\text{fit}}_{\text{peak}} / N^{\text{obs}}_{\text{peak}}, \tag{8.7}$$

which should be reasonably close to unity. The value of R is quoted for each fit in Table 8.1. It is important to consider the fact that R is heavily dependent not only on the accuracy of the Monte Carlo simulations, but also on the validity of the sequential R-matrix description through the estimated detection efficiencies and branching ratios. Therefore we use the value of R only as a guide and not as a strict constraint in the fitting procedure.

Other constraints could for instance be based on theoretical predictions or conclusions from earlier experimental work. As was mentioned in Section 1.1, most of the 0^+ strength in ^{12}C above the α threshold can be explained as the ghost of the Hoyle state (labelled 0^+_2). According to the discussion in (Kanada-En'yo 2007), we should expect another 0^+ state (0^+_3), as well as the rotational excitation of the Hoyle state (2^+_2), to appear at approximately 10 MeV of excitation energy, close to the energy range we are investigating in this section. The same theoretical paper states that the main α-cluster components of these states are

$$\begin{aligned} |0^+_2\rangle &\sim |^8\mathrm{Be}(0^+) \otimes L = 0\rangle_{J=0} \\ |0^+_3\rangle &\sim |^8\mathrm{Be}(2^+) \otimes L = 2\rangle_{J=0} \\ |2^+_2\rangle &\sim |^8\mathrm{Be}(0^+) \otimes L = 2\rangle_{J=2}. \end{aligned} \tag{8.8}$$

With these assignments, the states would break up mainly through respectively the (0,0,0), the (0,2,2) and the (2,2,0) mode.

Experimentally, the 2^+_2 state was measured at 10.03(11) MeV by (Zimmerman et al. 2013). In the related thesis work it is stated that for excitation energies of 9.1 MeV to 10.7 MeV the number of observed $^{12}\mathrm{C}(\gamma,\alpha)^8\mathrm{Be}$ events that did NOT proceed through the ground state peak of ^{8}Be was only 1 %–6 %, (Zimmerman 2013). In the same work those breakups were interpreted as going through the excited 2^+ state in ^{8}Be, however, if we consider the calculated branching ratio for breakup through the $^8\mathrm{Be}(0^+)$ ghost, shown in Figure 2.4, we see that the ghost contribution is exactly expected to be on the order of 1 %–6 % in this energy range. This means that if we are trying to identify the same 2^+ level that (Zimmerman et al. 2013) found, we can assume that its triple-α breakup is completely described by the (2,2,0) breakup model, and the (2,0,2), (2,2,2) and (2,4,2) models can be excluded from the fits.

The simplest assumption to make is that there is only the Hoyle state ghost to account for the spectrum, so we do a fit where only the (0,0,0) breakup mode is included. The result is shown in Figure 8.9 and in the column denoted "Fit 2"

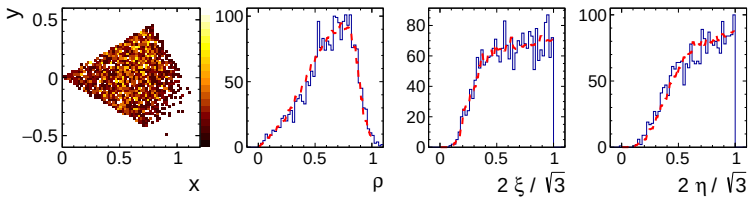

Figure 8.9: The solid, blue line shows the experimental data for the Q_α between 2.9 MeV and 3.1 MeV. The dashed, red line shows the result of "Fit 2", which includes only a (0,0,0) contribution, see Table 8.1.

in Table 8.1. Judging from the figure alone, the fit is not completely unrealistic, however, the χ^2 value is somewhat higher than the free fit, the corresponding p-value allowing the fit to be rejected at a confidence level of more than 99.95 %.

The next-simplest scenario is that we have only 0^+ strength in ^{12}C, but that it can decay through both the (0,0,0) and the (0,2,2) modes, consistent with the presence of the Hoyle state ghost and the 0_3^+ level of (8.8). "Fit 3" includes both breakup modes, however, the fitting routine converges toward zero contribution from the (0,2,2) mode, making the result equivalent to "Fit 2".

In line with the foregoing discussion, we include the (0,0,0) and the (2,2,0) breakups in "Fit 4". This fit converges on a non-zero contribution from the (2,2,0) breakup, see the result in Figure 8.10 and Table 8.1. It seems that if we allow a 2^+ state to contribute to the spectrum via the (2,2,0) breakup the fit improves considerably, resulting in a p-value which is ~ 35 higher than "Fit 2", which included only (0,0,0) breakups. Still, the low p-value suggests that the fit can be rejected at a confidence level of 99 %, which is not very satisfying. It must be remembered, though, that the low p-value should be compared against the value obtained from "Fit 1", where all breakup modes were included. Assuming that the the fitting routine managed to find the global minimum of the χ^2, the fit quality of "Fit 1" is the best we can hope to achieve. Comparing the p-values of "Fit 1" and "Fit 4" we see that they are quite similar, and in that view we

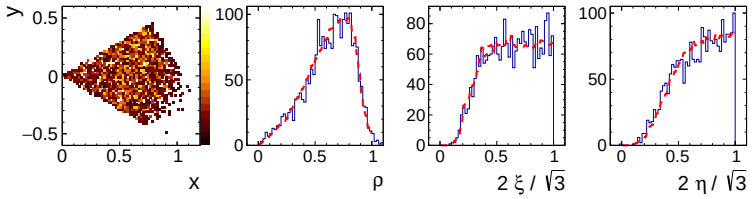

Figure 8.10: The solid, blue line shows the experimental data for the Q_α between 2.9 MeV and 3.1 MeV. The dashed, red line shows the result of "Fit 4", which includes a (0,0,0) and a (2,2,0) contribution, see Table 8.1.

conclude that "Fit 4" is close to the best result we can hope to obtain with this analysis method.

As a last experiment, we do a fit with the (0,0,0), the (2,2,0) and the (0,2,2) breakups included. The resulting fit is shown in Figure 8.11 and the best fit parameters are found in Table 8.1. "Fit 5" is slightly better than "Fit 4", but it is

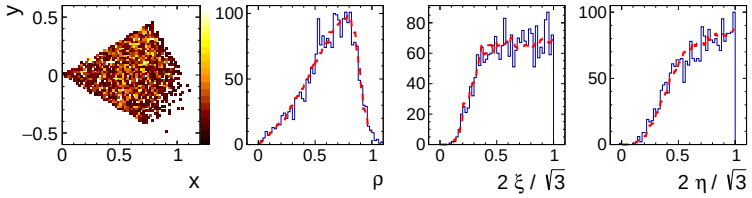

Figure 8.11: The solid, blue line shows the experimental data for the Q_α between 2.9 MeV and 3.1 MeV. The dashed, red line shows the result of "Fit 5", which includes a (0,0,0), a (2,2,0) and a (0,2,2) contribution, see Table 8.1.

hard to say whether one should prefer one over the other. One fact that should be noted, is that the inclusion of the (0,2,2) also requires a relatively larger contribution from the 2^+ resonance. A good idea is to consider on what order of magnitude we expect the 2^+ resonance to contribute to the spectrum. Referring again to the theoretical calculations by (Kanada-En'yo 2007), the 2_2^+ level is expected to be fed in β decay with a $\log(ft) = 6.3$, which should be compared with the measured feeding of the 0^+ strength of $\log(ft) \approx 4.4$ (Ajzenberg-

Selove 1990; Hyldegaard et al. 2009). Since the 0^+ "resonance" has a width of $\Gamma \approx 1.5\,\text{MeV}$, but the 2_2^+ level was measured by (Zimmerman et al. 2013) to have a width of $\Gamma \approx 0.8\,\text{MeV}$, we should expect the 2_2^+ level to make up $\sim 5\,\%$ of the spectrum. This number must further be corrected by the ratio of the branching to the $^8\text{Be}(0^+)$ ghost, which is larger for the 0^+ resonance by a factor of two, see Figure 2.4. In total, the 2_2^+ resonance should therefore only contribute $\sim 2.5\,\%$ to the spectrum. The result of "Fit 4" already suggests a contribution on the order of 20 %, and any fit results requiring a larger contribution I would consider with some doubt.

8.3.2 *Fitting in the 5.75MeV – 6.25MeV range*

We now proceed to inspect the phase space distributions at $Q_\alpha = 6\,\text{MeV}$, above the prominent peak of the 1^+ state. In this part of the spectrum we choose the somewhat coarser energy binning of 500 keV, mainly because of the limited number of counting statistics, but also because the phase space distributions have a slower variation with respect to the energy, than in the low-energy part of the spectrum.

In the first fit (Fit 6) we let all breakup modes contribute and the result is shown in Figure 8.12 together with the estimated background and simulated breakup patterns of the six models. We see that there are sharper features in these spectra and one could therefore hope to obtain a less ambiguous result than in the previous section. The fit parameters of "Fit 6" are listed in Table 8.3, and we notice that there seems to be only three breakup modes which contribute significantly to the spectrum, namely the (0,0,0), the (0,2,2) and the (2,2,2) modes, with the (2,2,2) mode dominating the spectrum.

We now try to find an alternative combination of the breakup modes providing an equally good fit to the experimental data. In "Fit 7" the (2,2,2) component that dominated in "Fit 6" is excluded, while all other parameters are still allowed to vary freely, see Figure 8.13 and Table 8.3. Judging both visually and from the calculated p-value this is not an acceptable fit, and we conclude that it is not possible to describe the spectrum without a sizeable contribution from (2,2,2) breakups. Another serious problem is that according to "Fit 7" there are

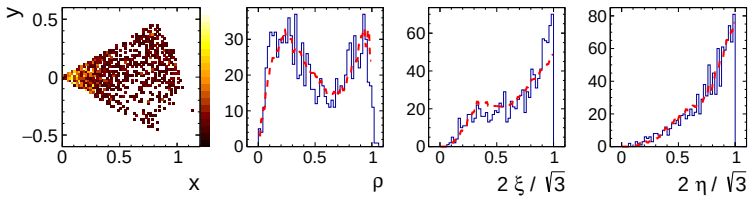

(a) The solid, blue line shows the experimental data while the dashed, red line shows the best fit (Fit 1 of Table 8.1).

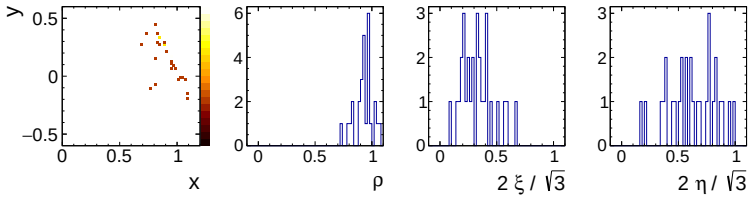

(b) Background contribution estimated from simulation and event mixing.

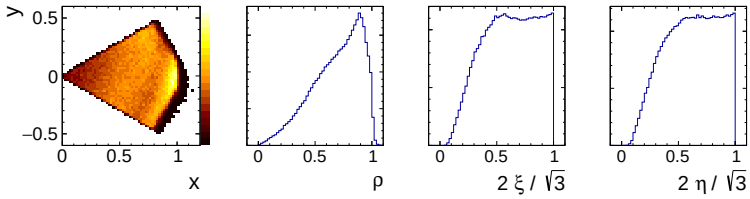

(c) Simulated (0,0,0) breakups.

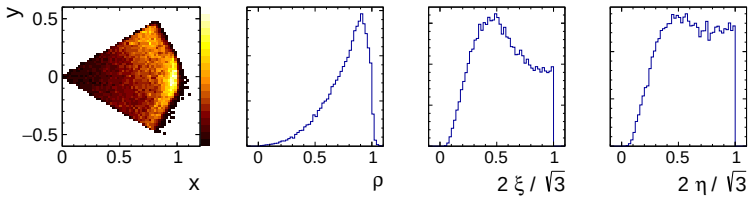

(d) Simulated (2,2,0) breakups.

Figure 8.12: A fit to experimental data with Q_α between 5.75 MeV and 6.25 MeV.

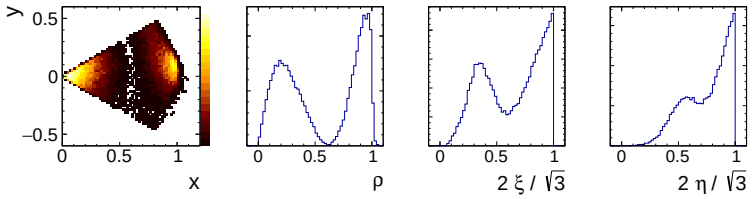

(e) Simulated (0,2,2) breakups.

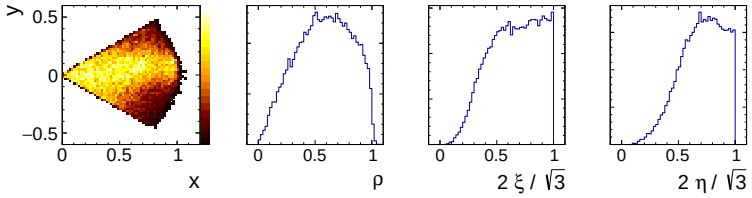

(f) Simulated (2,0,2) breakups.

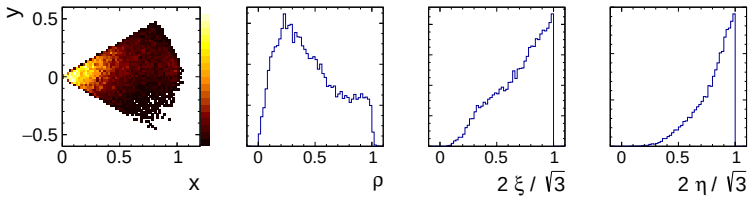

(g) Simulated (2,2,2) breakups.

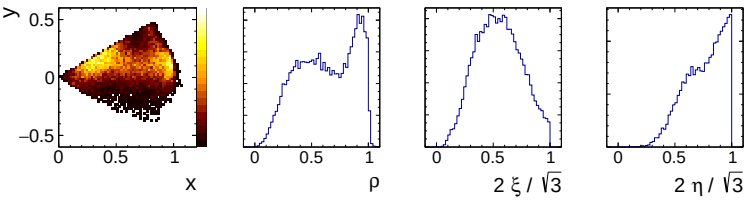

(h) Simulated (2,4,2) breakups.

Figure 8.12: Simulated breakups with Q_α between 5.75 MeV and 6.25 MeV.

Table 8.3: Parameters for the fits described in this section.

	Fit 6	Fit 7	Fit 8	Fit 9	Fit 10
n_{000}	137	0	0	-	142
n_{220}	5	0	191	123	-
n_{022}	282	669	-	246	284
n_{202}	0	409	0	0	0
n_{222}	655	-	886	710	653
n_{242}	0	0	0	0	0
R	0.58	0	1.39	0.89	0.56
ndf	136	137	137	137	137
χ^2_λ/ndf	1.476	2.765	1.708	1.470	1.465
p-value	0.00026	2.2×10^{-24}	4.7×10^{-7}	0.00028	0.00032

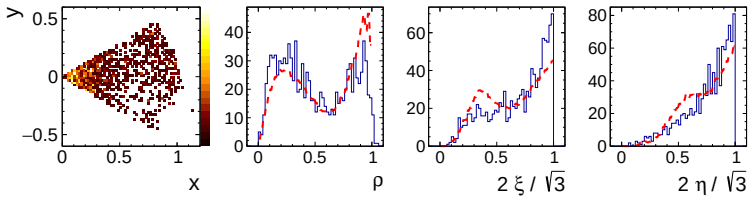

Figure 8.13: Illustration showing the experimental data in the energy range 5.75 MeV–6.25 MeV together with "Fit7" (red dashed line), see Table 8.3 and the text for details.

no breakups through 0^+ strength in ^{8}Be, which is inconsistent with the conclusions of Section 8.2.

Next, we try to suppress the (0,2,2) component which results in "Fit 8", see Figure 8.14. This is a better fit than "Fit 7" but still not very good and we reject it without further ado.

In the previous section it became clear that in the low-energy part of the spectrum the (0,0,0) and (2,2,0) breakups produced phase space distributions that were not easily distinguishable. To see if the same is true for energies around $Q_\alpha = 6\,\text{MeV}$ we could try in turn to exclude the (0,0,0) and the (2,2,0) models

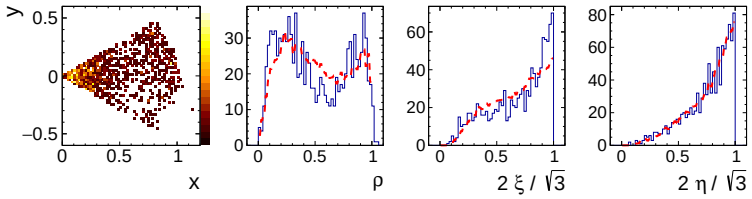

Figure 8.14: Experimental data (blue line) and "Fit 8" (red dashed line).

from the fit. This has been done for "Fit 9" and "Fit 10", which are shown in Figure 8.15. The reduced χ^2_λ is very similar for the two fits, and visual inspection shows no marked difference. We are thus again led to conclude that the (0,0,0) and (2,2,0) breakups are indistinguishable to the statistical accuracy of the present experiment. It should be noticed, however, that the value of R is closer to unity for "Fit 9", suggesting that "Fit 9" should be preferred over "Fit 10". More important is the fact that the (0,2,2) and (2,2,2) components change very little between the two fits, meaning that the ambiguity between (0,0,0) and (2,2,0) does not propagate to the other parameters of the fit.

It seems beyond reasonable doubt that the resonant strength for Q_α between 5.75 MeV and 6.25 MeV in ^{12}C is dominated by 2^+ strength decaying via the (2,2,2) breakup and contributing with approximately two-thirds of the decays. Some 0^+ strength decaying by (0,2,2) breakup is found to contribute with approximately one-fourth of the decays. It is not possible to conclude whether the small remaining part of the decays originates from 0^+ strength decaying via (0,0,0) breakup or 2^+ strength decaying via (2,2,0) breakup.

8.4 Broad resonances II: Fitting the entire spectrum

After our discussion of the phase space distributions in two limited parts of the spectrum it would be interesting to extend the analysis to the entire experimental spectrum. Hopefully we should be able to learn about the general trends without having to manually examine the fits in every single energy bin.

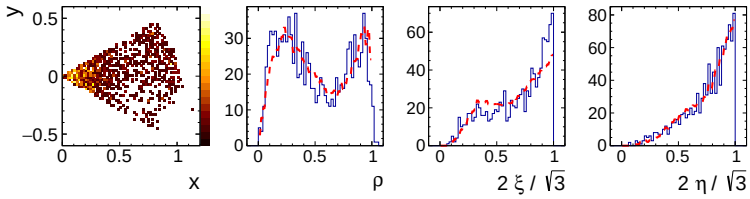

(a) The result of "Fit 9", where the (0,0,0) breakup mode is excluded.

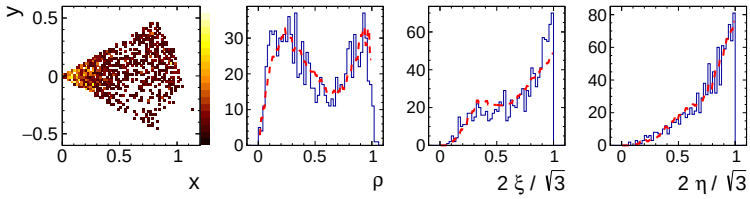

(b) The result of "Fit 10", where the (2,2,0) breakup mode is excluded.

Figure 8.15: Experimental data for the energy range 5.75 MeV–6.25 MeV (blue lines) and the result of two fits (red dashed lines).

8.4.1 The spectrum below the 12.7MeV state

In this low-energy part of the spectrum there are ample statistics and we use an energy binning of 200 keV. As in Section 8.3.1 we do the first fit without imposing any constraints on the fitting parameters, see Figure 8.16. The general picture is rather chaotic, which supports our earlier conclusion that the decay models are not easy to distinguish in this part of the spectrum. An interesting feature, though, is that the value of R rises enormously above 3.5 MeV. Even if we do not expect R to be exactly unity, the values from this fit seems excessive and unrealistic. We notice also that χ^2_λ/ndf increases in the same energy range, bringing further evidence that the quality of the fit above 3.5 MeV is not very good.

In the attempt to learn a bit more from this approach we now make the requirement that $0.8 < R < 1.2$, see Figure 8.17. Around 2.5 MeV we see the contributions from (2,2,0) and (2,0,2) taking over from the (0,0,0) breakup. This

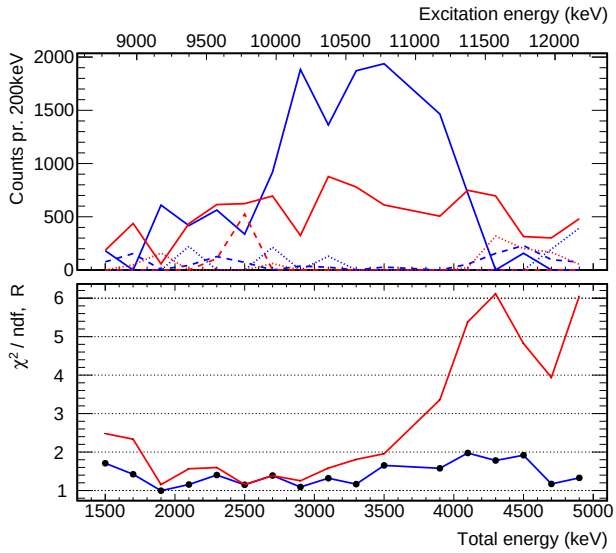

Figure 8.16: A fit to the phase space distributions in the low-energy part of the spectrum. The data have been divided in 200 keV bins and all breakup models are allowed to contribute to the fit in each bin. The best fit parameters are plotted as: n_{000} (solid blue), n_{220} (solid red), n_{022} (dashed blue), n_{202} (dashed red), n_{222} (dotted blue), n_{242} (dotted red). In the lower panel the reduced χ^2 (blue) and the value of R (red), defined in (8.7), are plotted.

is at exactly the same energy where (Freer et al. 2012) claim to have seen a 2^+ state in inelastic scattering of protons and alphas and it is tempting to conclude that we see the same state. It does, however, not seem reasonable that the (0,0,0) part of the spectrum should suddenly drop in intensity to allow a 2^+ state to pop up, and I believe it is just another proof of the strong correlation between the parameters, which was pointed out in the preceding section. More surprisingly, we see the (2,4,2) decay model starting to contribute above 3 MeV. The χ^2_λ/ndf is so high in this region that we should not really take the result seriously though.

We found in Section 8.3.1 that the data around 3 MeV were consistent with a model including only (0,0,0) and (2,2,0) breakups. To check if those two breakup

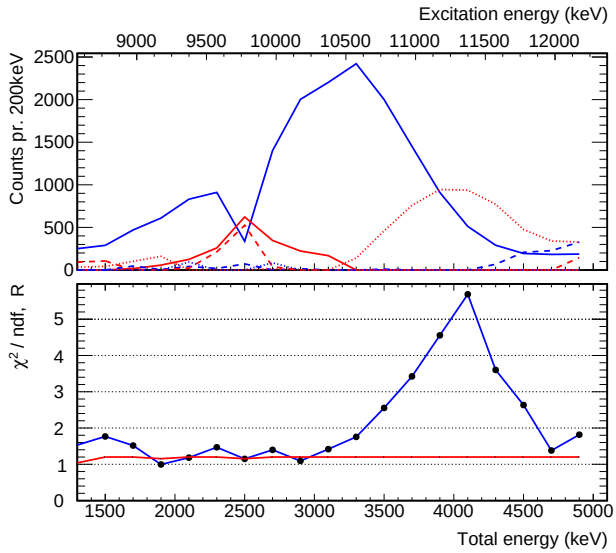

Figure 8.17: Fit where all breakup models are allowed to contribute but where the limitation $0.8 < R < 1.2$ is imposed. The line colors are described in the caption of Figure 8.16.

modes could explain the entire spectrum below 3 MeV we do a fit which only allows the (0,0,0) and (2,2,0) breakup models to contribute below $Q_{3\alpha} = 3$ MeV, while we still require $0.8 < R < 1.2$. The result is seen in Figure 8.18. From the value of χ^2_λ/ndf we conclude that it is perfectly possible to describe the data at low energies by (0,0,0) and (2,2,0) breakups only. The bump of (2,2,0) decays between 9.5 MeV and 10.5 MeV shows up again, hinting toward a small 2^+ contribution in this energy range. This is consistent with the position of the 2^+ state observed by (Zimmerman et al. 2013).

There are at least two conclusions we can make at this point: First, the breakups below 3 MeV are mainly (0,0,0) breakups, however, the addition of a small number of (2,2,0) breakups around 2.5 MeV–3.5 MeV provides an equally good fit, and thus our experiment is not inconsistent with a contribution from the 2^+ state observed by (Freer et al. 2012; Zimmerman et al. 2013). Sec-

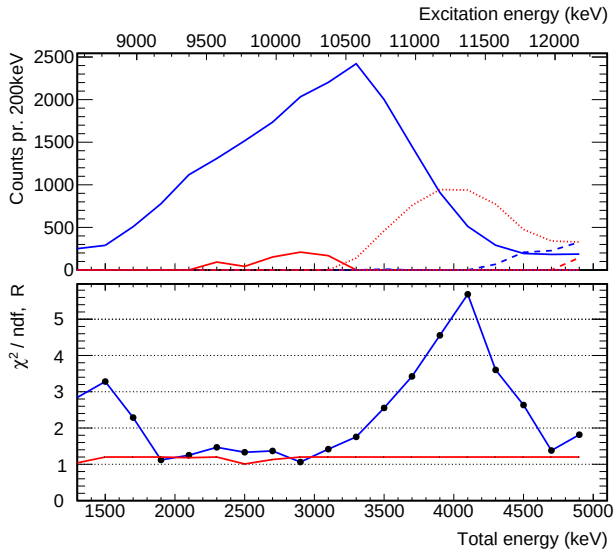

Figure 8.18: Fit where only (0,0,0) and (2,2,0) breakups are allowed for energies below 3 MeV. Also it is required that $0.8 < R < 1.2$. The line colors are described in the caption of Figure 8.16.

ond, the data are not fitted well by any combination of the breakup models between 3.5 MeV and 4.5 MeV, which indicates a breakdown of some of the implicit assumptions of the analysis method. This problem is quite serious and is investigated further in Section 8.5.

8.4.2 The spectrum above the 12.7MeV state

We proceed to look at the high-energy part of the spectrum. Here, we divide the data into energy bins of 500 keV width, and the first fit is performed without any restrictions on the parameters. The result is shown in Figure 8.19. The fit quality is satisfactory in all four bins, and it seems that the components that were found to dominate at 6 MeV continue to dominate the spectrum throughout this extended energy range. The poor power to discriminate between (0,0,0) and

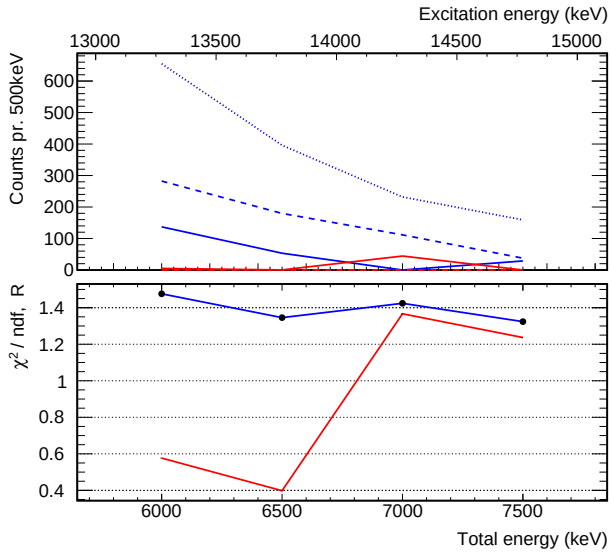

Figure 8.19: Fit where all breakup models are allowed to contribute without any constraints. The line colors are described in the caption of Figure 8.16.

(2,2,0) remains a problem, however, the contribution from these two breakup modes is not very important in this energy range. Also, we have seen that if the (0,0,0) or the (2,2,0) breakups are excluded individually from the fit, the dominating (2,2,2) and (0,2,2) components do not change appreciably. This conclusion is confirmed if we make another fit, imposing the constraint that $0.8 < R < 1.2$, see Figure 8.20. This fit includes more (2,2,0) than the previous, but the value of χ^2_λ/ndf is almost unchanged.

In conclusion, this part of the data set is best described by (2,2,2) and (0,2,2) breakups, in addition to a small number of decays through (0,0,0) and/or (2,2,0). It is remarkable that the contributions seem to be relatively constant over the 2 MeV range of the fit, indicating that we are observing both a very broad 0^+ resonance and a very broad 2^+ resonance. It is interesting to note that the breakup mode of the 2^+ strength is the same as that observed for the $2^+(T = 1)$ state at 16.11 MeV, see (Laursen et al. 2016). Such a $T = 1$ state can only α decay through

some admixture of a $2^+(T=0)$ component. Since the breakup mechanisms are identical it seems reasonable to suggest that we have identified this $2^+(T=0)$ component.

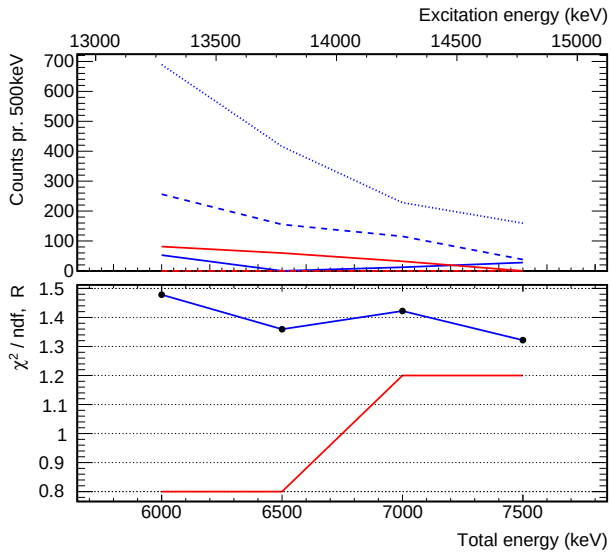

Figure 8.20: Fit where it is required that $0.8 < R < 1.2$. The line colors are described in the caption of Figure 8.16.

8.5 Limitations of the Method

In Section 8.4.1 we observed the quality of the fit degrade considerably around 4 MeV, either requiring an amount of decays through the ^{8}Be(0^+) ghost very much larger than what the theoretical model predicts from the observed number of ^{8}Be(peak) decays, or simply fitting the phase space distributions very poorly. In order to address this problem we take a more detailed look at the fits around 4 MeV. We do both a fit without any constraints at all (Fit 11), and a fit where we require $R = 1$ (Fit 12). The results are found in Table 8.4 and in Figure 8.21.

Table 8.4: Parameters for the fits described in this section.

	Fit 11	Fit 12
n_{000}	945	583
n_{220}	738	0
n_{022}	62	0
n_{202}	0	0
n_{222}	0	0
n_{242}	0	1059
R	4.3	1
ndf	134	135
χ^2_λ/ndf	1.920	6.089
p-value	8×10^{-10}	6×10^{-99}

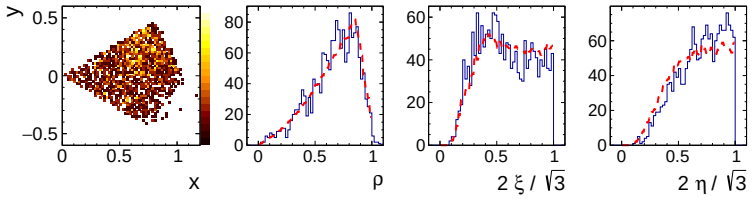

(a) The result of "Fit 11", where no constraints are imposed on the fitting parameters.

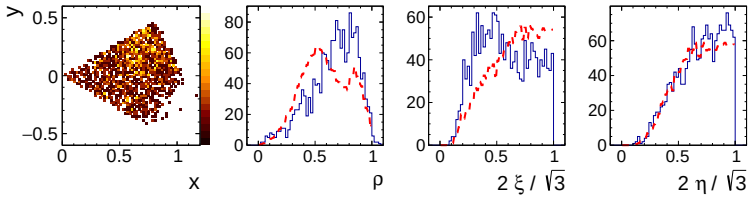

(b) The result of "Fit 12", where $R = 1$ is required to be fulfilled.

Figure 8.21: Experimental data for the energy range 3.9 MeV–4.1 MeV (blue lines) and the result of two fits (red dashed lines).

From the value of $\chi^2\lambda$/ndf alone it is clear that neither of the fits are acceptable. By visual inspection of Figure 8.21 we see that the general shape of the phas space distributions is not so badly imitated by "Fit 11", however, the value of R is much higher than expected. "Fit 12" on the other hand does not follow the experimental distributions at all. From this we conclude that either is the theoretical link between the observed ^{8}Be(peak) and the observed ^{8}Be(ghost) decays completely wrong, the calculated phase space weight of the breakup models are wrong, or the estimated detection efficiency is wrong. These causes are directly linked, since they are all calculated using the theoretical decay weight of Equation (3.7) and the Monte Carlo simulation. The possibility that the problems should be caused by misidentified background events seems unlikely, since the analysis of Section 7.3 showed that the background is expected to be minimal at this energy.

When we look at the total energy spectrum of 6.5 and the energy region around 4 MeV we see that this energy is also the transition point between the low-energy region, which we believe is dominated by the Hoyle state ghost, and the broad high-energy structure, which the preceding analysis showed to be dominated by second 0^+ resonance and a 2^+ resonance. This means that we can expect interference effects to play an important rôle in this region, and in fact it was shown explicitly by (Fynbo et al. 2005) that the sharp intensity drop of the low-energy 0^+ intensity from 3 MeV to 4.5 MeV was a sign of interference between the Hoyle state ghost and some other 0^+ strength.

The entire analysis of this section is based on the assumption that it is possible to add the contributions from different breakup modes incoherently in the Dalitz plot, but if interference is important this assumption breaks down. To include interference in the fitting procedure would not be impossible, however, it would be quite demanding in terms of computational resources. Another improvement would be to include constraints on the resonance line shape. The present analysis has been done by fitting each energy bin indepently, but a simultaneous fit to the entire spectrum, including knowledge of the standard R-matrix line shape, would probably exclude some of the unphysical fits, i.e. fits like the one in Figure 8.16.

9

SUMMARY

The purpose of this present work has been to characterise the broad, resonant structures that are observed above the triple-α threshold in ^{12}C in terms of their spin, parity and decay mechanism. The possibility of observing the second excited 2^+ state, first predicted by (Morinaga 1956) almost six decades ago and recently identified by (Zimmerman et al. 2013) has been a major motivation.

To achieve this goal an experiment was devised to populate the excited states in ^{12}C through the β decay of ^{12}N, the β decay selection rules providing a good handle on the spin and parity of the daughter states and eliminating background from several narrow levels. The experiment was carried out at the radioactive beam facility IGISOL in Jyväskylä where approximately 5.2×10^5 β-delayed triple-α breakups were measured in complete kinematics.

A sequential description of the three-particle breakup was used to adapt the well-known methods of R-matrix analysis to the triple-α breakup of the excited states in ^{12}C. The R-matrix calculations were combined with Monte Carlo simulations in order to compare the theoretical phase space distributions of the three-particle final state to the experimentally observed distributions.

Analysis of the triple-α breakups of the narrow 1^+ state at $E_x = 12.71\,\text{MeV}$ was used to test the method. Very good agreement was found between the observed phase space distribution and the distribution predicted by the sequential model where an α particle is emitted in an $L = 2$ breakup, leaving the ^{8}Be recoil in its first excited 2^+ state. The analysis also showed that the method can be used to probe the properties of the first excited state in ^{8}Be. A little research showed, however, that this is not a new idea (Dee and Gilbert 1936).

The observed excitation spectrum of ^{12}C shows a broad structure at $E_x = 8\,\text{MeV} - 12\,\text{MeV}$, which in the evaluations is interpreted as a resonance (Ajzenberg-Selove 1990). The idea that the ghost of the 0^+ Hoyle state contributes with a major part of this structure was already put forward by (F. C. Barker and Treacy 1962). Our results show that the resonant strength in this energy range is best described by a 0^+ state which decays by emission of an $L = 0$ α particle via the 0^+ ground state in ^{8}Be. This decay mechanism is the same as for the Hoyle state, which supports the "ghost" interpretation of the resonance.

The 2^+ state at 10 MeV was observed by (Zimmerman et al. 2013) to decay almost exclusively through emission of an $L = 2$ α particle via 0^+ strength in ^{8}Be. Our analysis shows that the phase space distribution of this breakup is not easily distinguishable from the phase space distribution of the beforementioned 0^+ decays. At the present level of statistics we cannot rule out the possibility of a small contribution from this 2^+ level in our data, but such a component is not needed in order to obtain a good description.

Another resonant structure is observed in the $E_x = 12\,\text{MeV} - 15\,\text{MeV}$ region. The decays from this structure show phase space distributions that are clearly different from the decays in the low-energy part of the spectrum. We find the spectrum to be dominated by 2^+ strength that decays via $L = 2$ emission of an α particle into 2^+ strength in ^{8}Be. These decays make up around two-thirds of the observed events in this energy range. It is probably an admixture of this 2^+ resonance which is responsible for the triple-α breakup of the $2^+(T = 1)$ state at $E_x = 16.11\,\text{MeV}$ (Laursen et al. 2016), based on their identical decay mechanisms.

The other major component in the high-energy spectrum is a broad 0^+ resonance which decays via $L = 2$ emission into 2^+ strength in ^{8}Be. Earlier β-decay experiments found a 0^+ resonance at $E = 11.2(3)\,\text{MeV}$ with a width of $\Gamma = 1.5(6)\,\text{MeV}$ (Hyldegaard et al. 2010). It could be the decays from this state that we observe. There are also decays via 0^+ strength in ^{8}Be in this part of the spectrum, but it was not possible in the analysis to conclude whether these decays come from 0^+ or 2^+ strenght in ^{12}C.

We see evidence that the analysis method breaks down around $E_x = 11.5\,\text{MeV}$. This failure is most probably caused by improper treatment of interference. Another effect, which is ignored in the analysis, is the initial polarisation of the ^{12}C nuclei that are produced in the β decay. The summation in Equation (3.8) as-

sumes all magnetic quantum numbers to be equally and incoherently populated. While this is not correct, it is not clear me whether the effects of polarisation on the phase space distributions dissappear when averaging over the direction of emission of the β particle. The applicability of the sequential model is in itself a questionable matter. The formulas from (Balamuth et al. 1974) has, to the best of my knowledge, not been derived in any rigorous way, and the best argument for their validity is that they "seem to work". All in all, the subject of β-delayed three-particle emission is still an open playground for the theoretically inclined.

It should be noted that the data set from the present experiment is still being analysed with respect to $\beta\alpha$ angular correlations. The distributions are dependent on the total spin of the populated resonance in ^{12}C and hopefully this analysis should be able to confirm or modify the spin assignments that were reached in the present work.

A

Simulated Models

The six allowed breakup models for 0^+ and 2^+ strength in ^{12}C are simulated as described in Chapter 7. To give the reader a general idea of the resulting phase space distributions and their energy dependence, the simulated decays events have been passed through the same data reduction and subjected to the same cuts as the experimental data. The results are shown for four energy bins around $Q_\alpha = 2\,\text{MeV}, 4\,\text{MeV}, 6\,\text{MeV}, 8\,\text{MeV}$ in Figures A.1 to A.7 on the following pages.

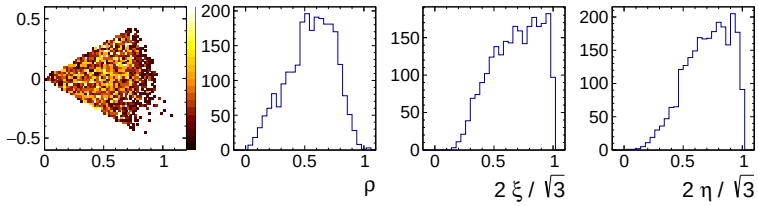

(a) 1750 keV–2250 keV, 2507 counts.

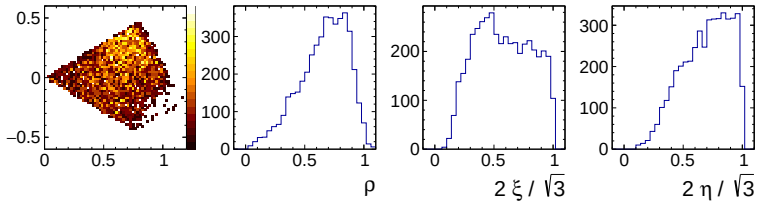

(b) 3750 keV–4250 keV, 4487 counts.

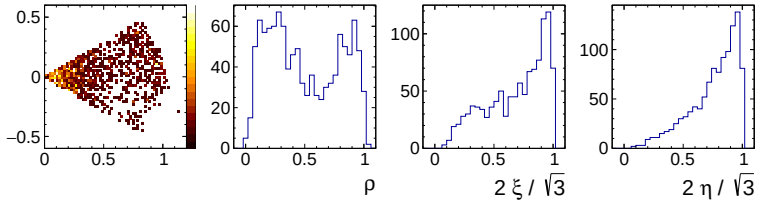

(c) 5750 keV–6250 keV, 1106 counts.

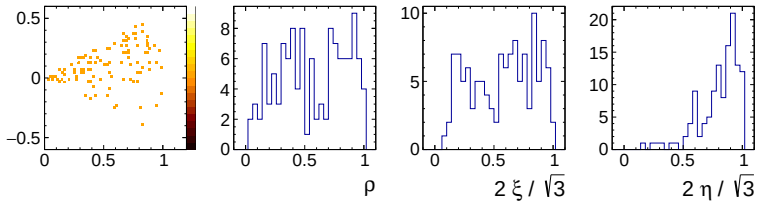

(d) 7750 keV–8250 keV, 124 counts.

Figure A.1: Phase space distribution of experimental data in the same energy bins as those used in Figures A.2 to A.7.

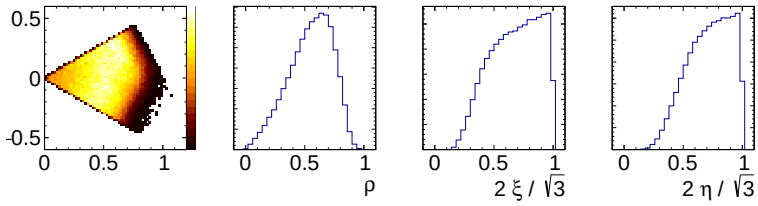

(a) 1750 keV–2250 keV

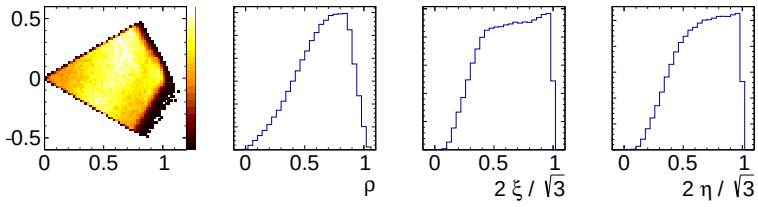

(b) 3750 keV–4250 keV

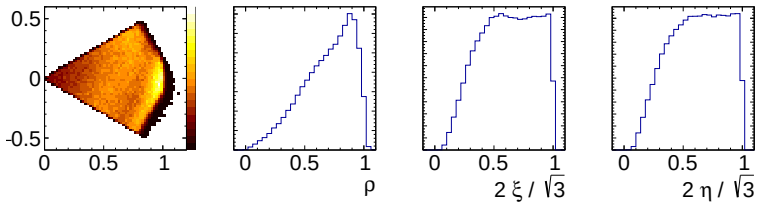

(c) 5750 keV–6250 keV

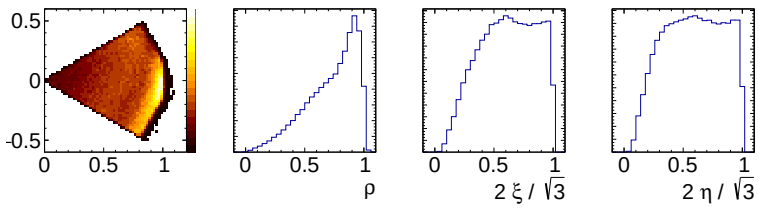

(d) 7750 keV–8250 keV

Figure A.2: Simulation of the (0,0,0) decay mode for four different values of $Q_{3\alpha}$.

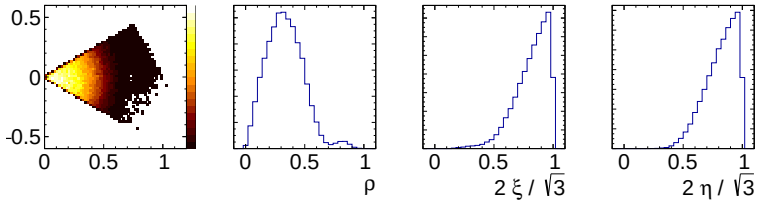

(a) 1750 keV–2250 keV

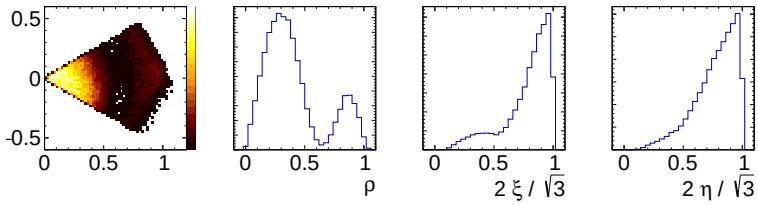

(b) 3750 keV–4250 keV

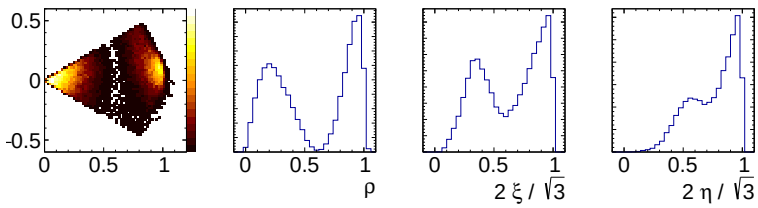

(c) 5750 keV–6250 keV

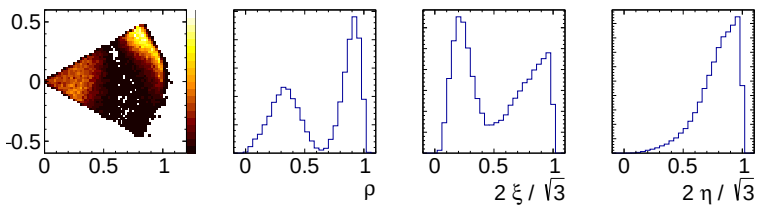

(d) 7750 keV–8250 keV

Figure A.3: Simulation of the (0,2,2) decay mode for four different values of $Q_{3\alpha}$.

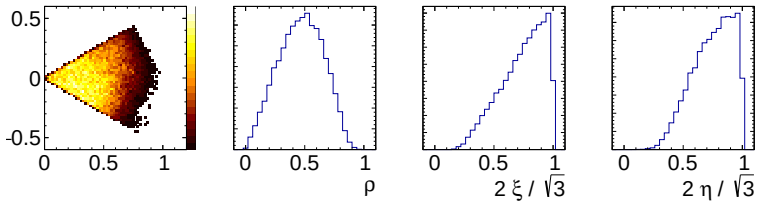

(a) 1750 keV–2250 keV

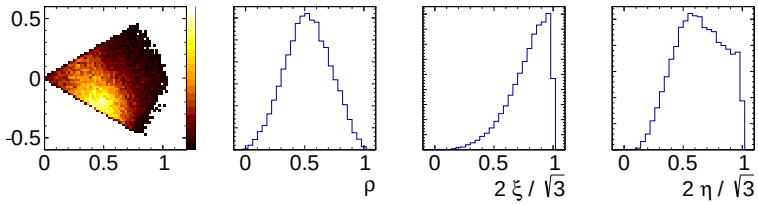

(b) 3750 keV–4250 keV

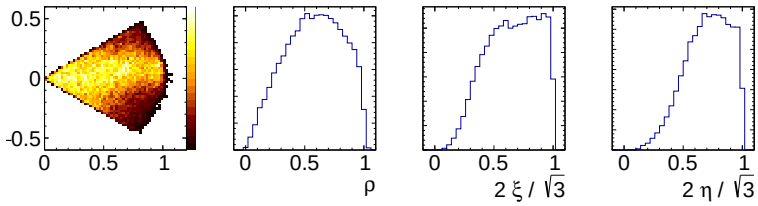

(c) 5750 keV–6250 keV

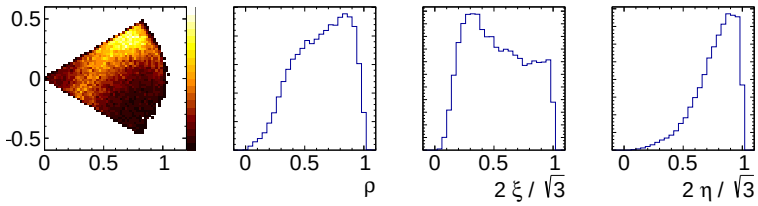

(d) 7750 keV–8250 keV

Figure A.4: Simulation of the (2,0,2) decay mode for four different values of $Q_{3\alpha}$.

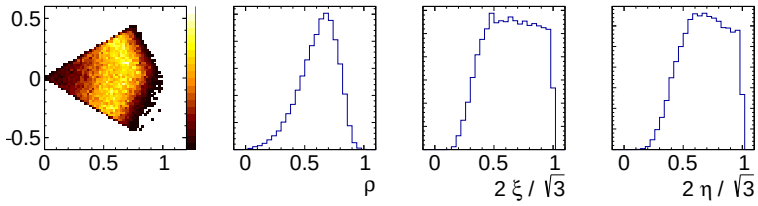

(a) 1750 keV–2250 keV

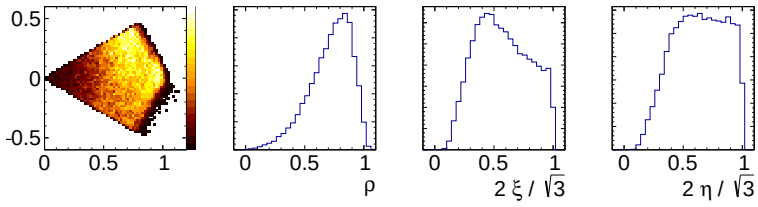

(b) 3750 keV–4250 keV

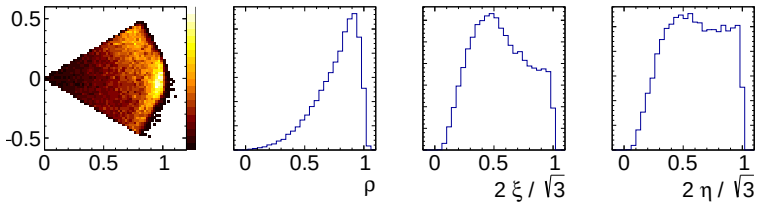

(c) 5750 keV–6250 keV

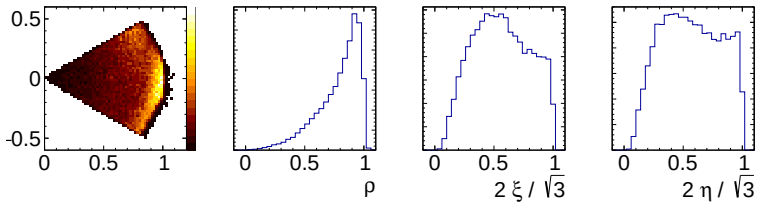

(d) 7750 keV–8250 keV

Figure A.5: Simulation of the (2,2,0) decay mode for four different values of $Q_{3\alpha}$.

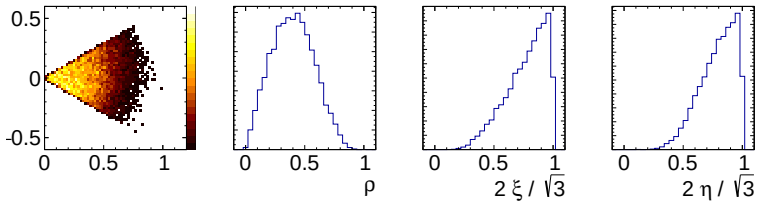

(a) 1750 keV–2250 keV

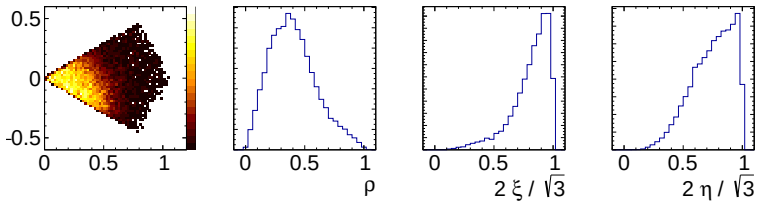

(b) 3750 keV–4250 keV

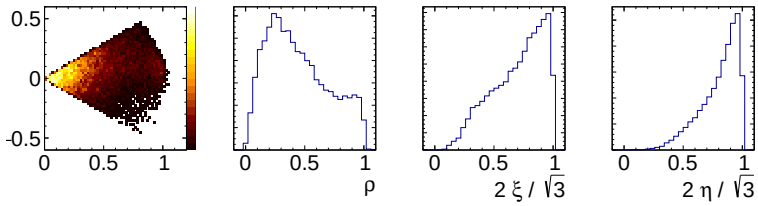

(c) 5750 keV–6250 keV

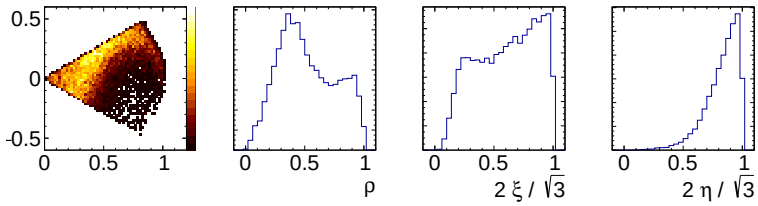

(d) 7750 keV–8250 keV

Figure A.6: Simulation of the (2,2,2) decay mode for four different values of $Q_{3\alpha}$.

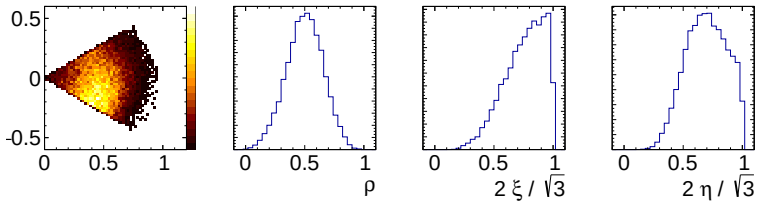

(a) 1750 keV–2250 keV

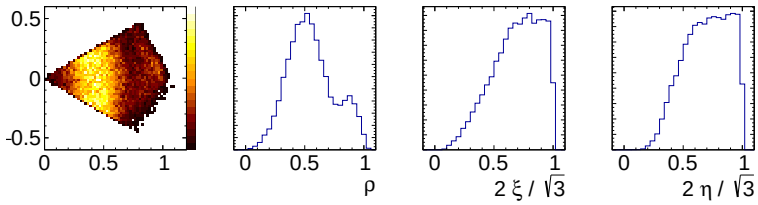

(b) 3750 keV–4250 keV

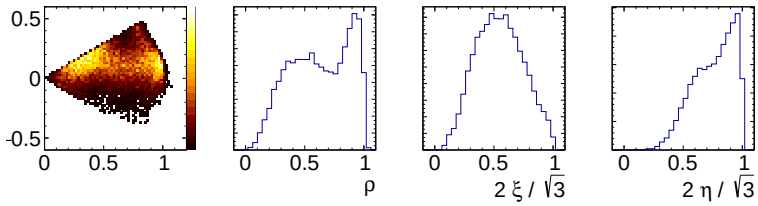

(c) 5750 keV–6250 keV

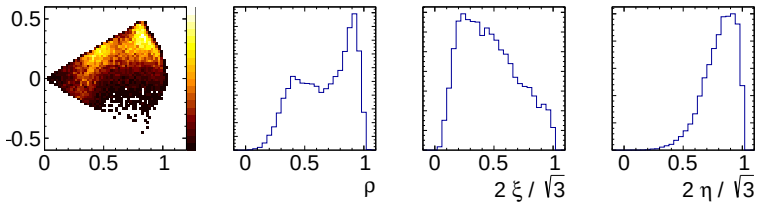

(d) 7750 keV–8250 keV

Figure A.7: Simulation of the (2,4,2) decay mode for four different values of $Q_{3\alpha}$.

BIBLIOGRAPHY

Abramowitz, M. and I. A. Stegun (1965). *Handbook of Mathematical Functions*. Dover Publications, Inc.

Ajzenberg-Selove, F. (1990). *Energy levels of light nuclei A = 11-12*. Nuclear Physics A 506.1, 1 –158.

Amaldi, E. and E. Fermi (1936). *On the Absorption and the Diffusion of Slow Neutrons*. Physical Review 50 (10), 899–928.

Äystö, J. (2001). *Radioactive Nuclear Beams Development and applications of the IGISOL technique*. Nuclear Physics A 693.1, 477 –494.

Azuma, R. E., L. Buchmann, et al. (1994). *Constraints on the low-energy E 1 cross section of $^{12}C(\alpha,\gamma)^{16}O$ from the β-delayed α spectrum of ^{16}N*. Physical Review C 50 (2), 1194–1215.

Baker, S. and R. D. Cousins (1984). *Clarification of the use of CHI-square and likelihood functions in fits to histograms*. Nuclear Instruments and Methods in Physics Research 221.2, 437 –442.

Balamuth, D. P., R. W. Zurmühle, and S. L. Tabor (1974). *Isospin-forbidden alpha decay of the 15.11-MeV state in ^{12}C*. Physical Review C 10 (3), 975–986.

Barker, F. C. (1969). *2+ states of 8Be*. Australian Journal of Physics 22.3, 293–316.

— (1971). *Calculation of the ^{12}C+alpha capture cross section at stellar energies.* Australian Journal of Physics 24, 777–792.

Barker, F. C. and P. B. Treacy (1962). *Nuclear levels near thresholds*. Nuclear Physics 38, 33 –49.

Barker, F. C. and E. K. Warburton (1988). *The beta-decay of 8He*. Nuclear Physics A 487.2, 269 –278.

Berkowitz, E. (1964). *Level parameters of short-lived nuclear states*. Nuclear Physics 60.4, 555 –560.

Bhattacharya, M., E. G. Adelberger, and H. E. Swanson (2006). *Precise study of the final-state continua in ^{8}Li and ^{8}B decays*. Physical Review C 73 (5), 055802.

Bijker, R. and F. Iachello (2000). *Cluster states in nuclei as representations of a $U(\nu+1)$ group*. Physical Review C 61 (6), 067305.

Blatt, J. M. and V. F. Weisskopf (1952). *Theoretical nuclear physics*. John Wiley & Sons, Inc.

Bohr, N. (1936). *Neutron capture and nuclear constitution*. Nature 137.3461, 344–348.

— (1937). *Transmutations of Atomic Nuclei*. Science 86.2225, 161–165.

Bortels, G. and P. Collaers (1987). *Analytical function for fitting peaks in alpha-particle spectra from Si detectors*. International Journal of Radiation Applications and Instrumentation. Part A. Applied Radiation and Isotopes 38.10, 831 –837.

Breit, G. and E. Wigner (1936). *Capture of Slow Neutrons*. Physical Review 49 (7), 519–531.

Brune, C. R. (2002). *Alternative parametrization of R -matrix theory*. Physical Review C 66 (4), 044611.

Brun, R. and F. Rademakers (1997). *New Computing Techniques in Physics Research V ROOT — An object oriented data analysis framework*. Nuclear Instruments and Methods in Physics Research Section A: Accelerators, Spectrometers, Detectors and Associated Equipment 389.1, 81 –86.

Cohen, S. and D. Kurath (1965). *Effective interactions for the 1p shell*. Nuclear Physics 73.1, 1 –24.

Cook, C. W., W. A. Fowler, et al. (1957). *B^{12}, C^{12}, and the Red Giants*. Physical Review 107 (2), 508–515.

— (1958). *High-Energy Alpha Particles from B^{12}*. Physical Review 111 (2), 567–571.

Dalitz, R. (1953). *CXII. On the analysis of τ-meson data and the nature of the τ-meson*. The London, Edinburgh, and Dublin Philosophical Magazine and Journal of Science 44.357, 1068–1080.

Dee, P. I. and C. W. Gilbert (1936). *The Disintegration of Boron into Three α -Particles*. Proceedings of the Royal Society of London. Series A, Mathematical and Physical Sciences 154.881, 279–296.

Diget, C. A., F. C. Barker, et al. (2005). *Properties of the 12C 10 MeV state determined through β-decay*. Nuclear Physics A 760.1, 3 –18.

Diget, C. A., F. C. Barker, et al. (2009). *Breakup channels for ^{12}C triple-α continuum states*. Physical Review C 80 (3), 034316.

Dunbar, D. N. F., R. E. Pixley, et al. (1953). *The 7.68-Mev State in C^{12}*. Physical Review 92 (3), 649–650.

Epelbaum, E., H. Krebs, et al. (2012). *Structure and Rotations of the Hoyle State*. Physical Review Letters 109 (25), 252501.

Freer, M., H. Fujita, et al. (2009). *2^+ excitation of the ^{12}C Hoyle state*. Physical Review C 80 (4), 041303.

Freer, M., M. Itoh, et al. (2012). *Consistent analysis of the 2^+ excitation of the ^{12}C Hoyle state populated in proton and α-particle inelastic scattering*. Physical Review C 86 (3), 034320.

Freer, M., A. H. Wuosmaa, et al. (1994). *Limits for the 3α branching ratio of the decay of the 7.65 MeV, 0_2^+ state in ^{12}C*. Physical Review C 49 (4), R1751–R1754.

Frisch, O., G. Hevesy, and H. McKay (1936). *Selective Absorption of Neutrons by Gold*. Nature (London) 137, 149–150.

Fynbo, H. O. U., C. A. Diget, et al. (2005). *Revised rates for the stellar triple-α process from measurement of 12C nuclear resonances*. Nature 433.7022, 136–139.

Fynbo, H. O. U., Y. Prezado, et al. (2003). *Clarification of the Three-Body Decay of ^{12}C (12.71 MeV)*. Physical Review Letters 91 (8), 082502.

Galassi, M., J. Davies, et al. (2009). *GNU Scientific Library Reference Manual*. 3rd.

Hamilton, D. R. (1947). *Electron-Neutrino Angular Correlation in Beta-Decay*. Physical Review 71 (7), 456–457.

Hoyle, F., D. Dunbar, et al. (1953). *A State in C^{12} Predicted from Astrophysical Evidence*. Physical Review 92, 1095c.

Hyldegaard, S., M. Alcorta, et al. (2010). *R-matrix analysis of the β decays of ^{12}N and ^{12}B*. Physical Review C 81 (2), 024303.

Hyldegaard, S., C. Forssén, et al. (2009). *Precise branching ratios to unbound 12C states from 12N and 12B β-decays*. Physics Letters B 678.5, 459 –464.

Ikeda, K., N. Takigawa, and H. Horiuchi (1968). *The Systematic Structure-Change into the Molecule-like Structures in the Self-Conjugate 4n Nuclei*. Progress of Theoretical Physics Supplement E68, 464–475.

Itoh, M., H. Akimune, et al. (2011). *Candidate for the 2^+ excited Hoyle state at $E_x \sim 10$ MeV in ^{12}C*. Physical Review C 84 (5), 054308.

Itoh, M., S. Ando, et al. (2014). *Further Improvement of the Upper Limit on the Direct 3α Decay from the Hoyle State in ^{12}C*. Physical Review Letters 113 (10), 102501.

Kanada-En'yo, Y. (2007). *The structure of ground and excited states of 12C*. Progress of Theoretical Physics 117.4, 655–680.

Kirsebom, O. S. (2013). *Decay of $12C^*$ into Three α Particles*. Few-Body Systems 54.5, 755–759.

Kirsebom, O. S., M. Alcorta, et al. (2010). *Breakup of ^{12}C resonances into three α particles*. Physical Review C 81 (6), 064313.

Kirsebom, O. S., M. Alcorta, et al. (2012). *Improved Limit on Direct α Decay of the Hoyle State*. Physical Review Letters 108 (20), 202501.

Knoll, G. F. (2000). *Radiation Detection and Measurement*. 3rd. John Wiley and Sons, Inc.

Kragh, H. (2010). *An anthropic myth: Fred Hoyle's carbon-12 resonance level*. English. Archive for History of Exact Sciences 64.6, 721–751.

Lane, A. M. and R. G. Thomas (1958). *R-Matrix Theory of Nuclear Reactions*. Reviews of Modern Physics 30 (2), 257–353.

Laursen, K. L., H. O. U. Fynbo, et al. (2016). *Complete kinematical study of the 3α breakup of the 16.11MeV state in 12C*. arXiv:1604.01244 [nucl-ex].

Marín-Lámbarri, D. J., R. Bijker, et al. (2014). *Evidence for Triangular $\mathscr{D}_{3h}$ Symmetry in ^{12}C*. Physical Review Letters 113 (1), 012502.

Michel, N. (2007). *Precise Coulomb wave functions for a wide range of complex l, η and z*. Computer Physics Communications 176.3, 232 –249.

Moore, I., T. Eronen, et al. (2013). *Towards commissioning the new IGISOL-4 facility*. Nuclear Instruments and Methods in Physics Research Section B: Beam Interactions with Materials and Atoms 317, Part B. {XVIth} International Conference on ElectroMagnetic Isotope Separators and Techniques

Related to their Applications, December 2–7, 2012 at Matsue, Japan, 208 – 213.

Morinaga, H. (1956). *Interpretation of Some of the Excited States of 4n Self-Conjugate Nuclei*. Physical Review 101 (1), 254–258.

— (1966). *On the spin of a broad state around 10 MeV in 12C*. Physics Letters 21.1, 78 –79.

Öpik, E. J. (1951). *Stellar Models with Variable Composition. II. Sequences of Models with Energy Generation Proportional to the Fifteenth Power of Temperature*. Proceedings of the Royal Irish Academy. Section A: Mathematical and Physical Sciences 54, 49–77.

Overway, D., J. Jänecke, et al. (1981). *Reaction dependence of nuclear decay linewidths*. Nuclear Physics A 366.2, 299 –319.

Refsgaard, J., O. Kirsebom, et al. (2016). *Measurement of the branching ratio for β-delayed α decay of 16N*. Physics Letters B 752, 296 –301.

Ricken, L., K. Bodek, and A. Szczurek (1990). *The first excited state of 8Be studied in the 7Li(p, γ)8Be reaction*. Nuclear Physics A 515.2, 226 –236.

Riisager, K., H. Fynbo, et al. (2015). *Broad resonances and beta-decay*. Nuclear Physics A 940, 119 –137.

Rolfs, C. E. and W. S. Rodney (1988). *Cauldrons in the Cosmos*. The University of Chicago Press.

Roth, R., J. Langhammer, et al. (2011). *Similarity-Transformed Chiral $NN + 3N$ Interactions for the Ab Initio Description of ^{12}C and ^{16}O*. Physical Review Letters 107 (7), 072501.

Rytz, A. (1991). *Recommended energy and intensity values of alpha particles from radioactive decay*. Atomic Data and Nuclear Data Tables 47.2, 205 –239.

Salpeter, E. (1952). *Nuclear Reactions in Stars Without Hydrogen*. Astrophysical Journal 115, 326–328.

Schwalm, D. and B. Povh (1966). *Alpha particles following the β-decay of 12B and 12N*. Nuclear Physics 89.2, 401 –411.

Steinbauer, E., G. Bortels, et al. (1994). *A survey of the physical processes which determine the response function of silicon detectors to alpha particles*. Nuclear Instruments and Methods in Physics Research Section A: Accelerators, Spectrometers, Detectors and Associated Equipment 339.1, 102 –108.

Szczurek, A., K. Bodek, et al. (1991). *Ghost anomaly and first excited state of 8Be in the 9Be(d, tα)4He reaction at 7 MeV*. Nuclear Physics A 531.1, 77 –92.

Tang, X. D., K. E. Rehm, et al. (2010). *Determination of the $E1$ component of the low-energy $^{12}C(\alpha,\gamma)^{16}O$ cross section*. Physical Review C 81 (4), 045809.

Tarasov, O. and D. Bazin (2008). *LISE++: Radioactive beam production with in-flight separators*. Nuclear Instruments and Methods in Physics Research Section B: Beam Interactions with Materials and Atoms 266.19–20. Proceedings of the {XVth} International Conference on Electromagnetic Isotope Separators and Techniques Related to their Applications, 4657 –4664.

Tengblad, O., U. Bergmann, et al. (2004). *Novel thin window design for a large-area silicon strip detector*. Nuclear Instruments and Methods in Physics Research Section A: Accelerators, Spectrometers, Detectors and Associated Equipment 525.3, 458 –464.

Tilley, D., J. Kelley, et al. (2004). *Energy levels of light nuclei A=8,9,10*. Nuclear Physics A 745.3, 155 –362.

Torresi, D., D. Stanko, et al. (2013). *Influence of the interstrip gap on the response and the efficiency of Double Sided Silicon Strip Detectors*. Nuclear Instruments and Methods in Physics Research Section A: Accelerators, Spectrometers, Detectors and Associated Equipment 713, 11 –18.

Von Neumann, J. (1951). *13. Various Techniques Used in Connection With Random Digits*. Nat. Bureau of Standards, 36 –38.

Weinberg, S. (1996). *The quantum theory of fields*. Vol. 1. Cambridge University Press.

Wheeler, J. A. (1937). *Molecular Viewpoints in Nuclear Structure*. Physical Review 52 (11), 1083–1106.

Wilkinson, D. H., D. E. Alburger, et al. (1963). *Alpha-Particle Emission in the Decays of B^{12} and N^{12}*. Physical Review 130 (5), 1953–1960.

Zemach, C. (1964). *Three-Pion Decays of Unstable Particles*. Physical Review 133 (5B), B1201–B1220.

Ziegler, J., M. Ziegler, and J. Biersack (2010). *SRIM - The stopping and range of ions in matter (2010)*. Nuclear Instruments and Methods in Physics Research, Section B: Beam Interactions with Materials and Atoms 268.11-12. cited By 1273, 1818–1823.

Zimmerman, W. R. (2013). *Direct Observation of the Second 2+ State in 12C*. Doctoral Dissertation. University of Connecticut.

Zimmerman, W. R., M. W. Ahmed, et al. (2013). *Unambiguous Identification of the Second 2^+ State in ^{12}C and the Structure of the Hoyle State*. Physical Review Letters 110 (15), 152502.